UNIVERSITÉ DE STRASBOURG

DOCTORAL SCHOOL Physics Chemistry-Physics

UMR 7550

THESIS defended by:

Jérémy CHASTENET

on: **September, 26th 2017**

to be granted the rank of: **PhD of the Université de Strasbourg**

Major/Specialty: Astrophysics

Analysis of dust emission in nearby galaxies

Implications of the modeling assumptions

THESIS supervised by:

Mrs BOT Caroline	Fellow astronomer, Observatoire astronomique de Strasbourg
Mr Gordon Karl	Astronomer, Space Telescope Science Institute

REPORTERS:

Mrs MADDEN Susan	CEA Engineer, CEA
Mr BAES Maarten	Professor of Astrophysics, Sterrenkundig Observatorium

---

OTHER MEMBERS OF THE BOARD:

Mrs Karin DEMYK	Head of research, IRAP
Mrs Françoise GENOVA	Head of research, Observatoire astronomique de Strasbourg
Mr Laurent CAMBRESY	Astronomer, Observatoire astronomique de Strasbourg

Il faut se défier d'une réponse trop précise, car des explications circonstanciées sur de tels sujets tournent aisément à la fausse profondeur, quand ce n'est à l'absurdité gratuite.

Ernst GOMBRICH, in Histoire de l'art

Acknowledgements

I wish to express my deepest gratitude to my advisers, Caroline and Karl, without whom the last 3 years would have not been such a success. I am thankful that they have trusted me with their project, and led me with great tutorship towards this ending. Encouraging, friendly, and sensitive, they have always seemed to show the best of themselves, and I thrived learning how to be a researcher thanks to their advice. I sincerely hope to have reached their expectations, and will do my best to pursue this path, and perpetuate their insights[1]. I also wish to thank Françoise, first for agreeing to be my adviser, and then for having kept an eye on my work and for showing a constant interest in my progress. And to Mark and Hervé, for their unfailing support as directors, through every crisis I had to face.

Cette thèse aurait été beaucoup moins facile sans le soutien de ma famille. Merci à mes parents, Papa et Maman (ou René et Véronique pour les moins intimes) pour leur aide dans mes multiples déménagements[2], leur soutien inébranlable et leurs encouragements. Merci aussi à ma fratrie, Marine et Jonathan, pour avoir été aussi présents que nécessaire, pour toutes les bonnes nouvelles et les célébrations[3]. Merci aussi à Arnaud, d'être toujours là, sans condition, et sans qui cette dernière année aurait moins de sens.

Tout ce travail n'aurait pas été possible sans l'Observatoire astronomique de Strasbourg, et tout son personnel, en particulier Céline, Sandrine et Véronique. Un grand merci pour m'avoir épauler dans mes (trop) nombreuses démarches administratives. Merci aussi à tous les autres, pour les réponses à mes questions, scientifiques ou pas.
I am grateful to the people who made my working environment as pleasant as possible during my stay at the STScI: Bram, Gail, Heddy, Josh, Julia, Kirill, Martha. With motivating discussions, intelligent remarks and a good sense of humor; these things have made our meetings delightful.

Merci à mes amis d'ici, toujours aux rendez-vous, qu'ils soient près ou qu'elle soit loin : Anaïs, Clémentine, Elodie, Eva, Fanny, Hélène, Pauline, Vincent et d'autres. Les retrouvailles, régulières ou pas, sont toujours aussi brillantes et pleines de nouveaux souvenirs.
Thank you, of course, to all the friends I made during my journeys in the US: Adrian, Alyssandra, Asa, Caleb, Dylan, Jackie, Lynn, and Ricky. They have taught me the culture of their country, shown me some of it, and made my experience of the US a marvelous one. Thank you for correcting my English mistakes, making fun of my Frenchness, voting Democrats[4], and, for my roommates: feeding me bacon.

Et enfin, merci à mes "co-docs" sans qui l'ambiance de la thèse n'aurait pas été la même : François, Guillaume, JB, Jérôme, Julien, Mathieu, Maxime, et aussi Nicolas, Nicolas, et Nicolas[5]. Les rires, les terrasses me manqueront davantage que le son des verres qui s'entrechoquent.

Merci à tous. Here's to us.

[1] Including: how to be a good Pokémon™ trainer, how to be friend with everyone, and how not to work on weekends. I did not pass any of those.

[2] J'ai cumulé un total de huit logements différents en trois ans. Alors merci beaucoup !

[3] Qui s'échelonnent d'une union maritale à la sortie de la Nintendo© Switch.

[4] You failed nonetheless.

[5] "Not necessarily in that order."

Contents

List of Figures

List of Tables

Part I

General Introduction

1

Enter the void

We can estimate that there are about 54 galaxies in our "direct" neighborhood (astronomically speaking, so... very far). In our Milky Way (MW) only, a couple of hundreds of billions stars of all kinds and colors can be counted. In other words, there is a lot going on in this vast space. All these stars of different masses, compositions, ages; galaxies with different shapes, speeds, populations; gas gathered in clouds diffuse or dense; dust grains packed and glued forming large structures; high-energy objects of unbearable densities, planets that hold the secrets of their formation... There is an infinite reservoir of questions to answer in our Universe, and each of us can only do so much to satisfy our endless curiosity.

That is why, in this thesis, we will focus on one of the things that is found in our Universe: *dust*. "Dust", in its general term, refers to small solid particles, of nanometer to micrometer in size; a dust grain is mainly composed of carbon and hydrogen, with heavier elements in lower quantity. Clarification though: "dust" can refer to two different kinds: one can be found in what is called protoplanetary disks, in an early stage of planet formation, and the other is called interstellar dust. We will focus only on the dust that evolves in the void between stars, inside a galaxy –aka the interstellar medium (ISM). The interstellar medium refers to the mixture of gas and dust, tightly mixed together and yet different. Dust is carried by gas flows, illuminated by starlight and re-radiates its own light. It is a fascinating probe of the intense industry that is going on inside galaxies. This first part aims at explaining the physics and chemistry of dust grains: how do they react to light, what are they made of, where do they come from...? In a few words: what do we know about them (so far)? We will go over the history and equations we need to build a comprehensive understanding of dust. This information will become crucial for the following chapters that are exclusively dedicated to the study of this dust in nearby galaxies, and in a more distanced approach, the study of its interpretation through observations.

Before diving head first into space, we will overview some of the basic descriptions of the objects that can be found in a galaxy, and how they shape the information that we have when we look up at the skies, and collect the celestial light.

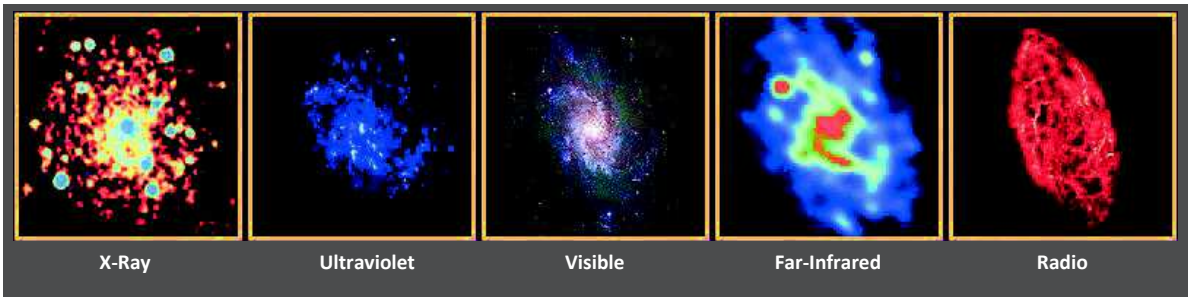

Figure 1.1: M33 seen in five parts of the electromagnetic spectrum, tracing various components of the galaxy. *Credit:* http://coolcosmos.ipac.caltech.edu

1.1 Watching a galaxy

Light is our best –and almost only– friend in astronomy. Thanks to the photons carrying the energy through space, the information comes to us. We use this light to learn all we can about the place we live in. Figure 1.1 shows the Triangulum Galaxy (Messier 33) observed at different wavelengths. The different parts of the electromagnetic spectrum relay different information. A short description of the wavelength domains, which we can separate to extract different information, is given below.

Gamma rays trace very high energy, and extremely hot objects, close to a billion degrees. This includes cosmic rays when they collide with atomic hydrogen, pulsars, neutron stars (very high density and rapidly rotating stars), or the surroundings of black holes, accreting and accelerating matter.
X-Rays trace the hot gas present in a galaxy, as well as neutron stars or supernova remnants (hot matter remaining after the explosion of a massive star). Gas, however, can be detected throughout the entire spectrum through the emission and absorption lines characteristic of the transitions between energy levels of the composing atoms or molecular transitions.
The ultraviolet (UV) emission comes from young, hot stars, recently formed (up to $\sim$ 1 Myr old), and quasars. This part of the spectrum also includes scattered photons from these various sources; this is important to take into consideration as it means it does not only trace the sources themselves.
More evolved stars (a few Myr up to $\sim$ 1 Gyr) have an emission peak in the visible, which therefore traces galaxies, filled with stars, and planets seen in visible light by reflection.
In the infrared (IR), dust emission prevails over other components, such as old and colder stars. It also allows observations of asteroids and comets.
Finally, radio emission is characteristic of cold matter: cold gas and dust, molecular clouds, but also the cosmic microwave background (remaining emission of the 'first light of space'), and the synchrotron emission.

The energy emitted by an astronomical source is distributed over the wavelength space. Figure 1.2 shows the spectral energy distribution (SED) of NGC6240, a starburst galaxy, and some ranges of the electromagnetic spectrum.

To collect such signal, we cannot use the same kind of instruments at all wavelengths. Because of our atmosphere, gamma rays, X-rays, UV and IR photons are mostly blocked before reaching Earth, and observations at these wavelengths require space telescopes, or high-altitude balloons and rockets. Ground-based observatories are thus almost entirely dedicated to observing the visible sky, the near infrared, sub-millimeter, millimeter and the radio wavelengths.

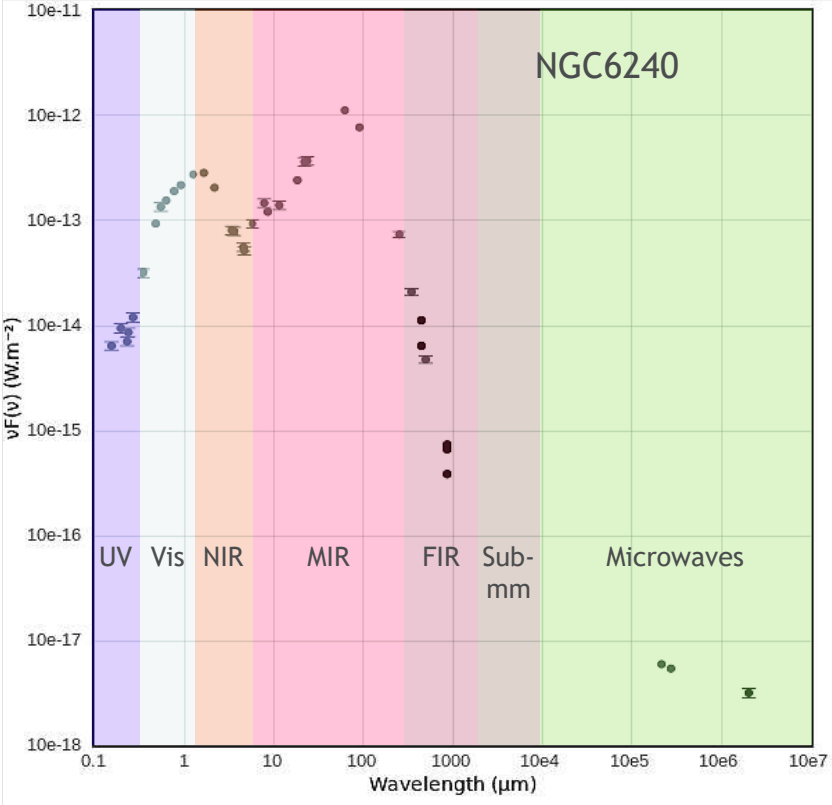

Figure 1.2: A few photometric points of the SED of NGC6240, a starburst galaxy. *From the VizieR catalogue access tool, CDS, Strasbourg, France (Ochsenbein et al. 2000).*

1.2 The Interstellar Medium

In this section, we will briefly describe the ISM, the medium of main interest in this thesis.

The ISM is mostly filled with H and He atoms. These elements were formed shortly after the Big Bang, and observations notice a slow decrease of the H fraction with time and a slow increase of He. The heavy elements[1] found in the ISM are the results of stellar nucleosynthesis. Some of these elements are found in their solid forms in dust grains. Figure 1.3 shows a sketch of a few objects and processing in the ISM. The ISM evolution is a cycle, most of it is re-used and enriched and modified. Let us start from the 'Molecular cloud'. It is a dense cloud of gas and dust, and, as it condenses and gets denser, it will eventually collapse on itself. When the density and temperature are high enough, it can give birth to new stars. Stars can be roughly distinguished as low- and high-mass; their lives would not follow the same pattern and neither would their death. In one case, a bright supernova is the result of the stars death. In the other case, a planetary nebula, which is more discreet. In both cases, heavy elements are formed and ejected into the diffuse ISM through stellar winds and shock waves. Dust grains start to appear where and when metals are available : dust grains are formed in the atmospheres of low-mass stars, and as they live, gather metals and other elements found in the diffuse ISM. We can find elements like oxygen, silicon or manganese in dust grains. Although contributing less in mass than hydrogen or carbon, they play an important role in dust composition. More details will be given in the following sections. A region can be ionized by UV photons coming from the surroundings stars; the more diffuse, the stronger the ionization. It will affect the gas composition (for instance, ionize the H atoms) of that region, as well as, we believe, dust grains. Subjects to

[1] In an astrophysical context, 'heavy element' or 'metal' refers to any element heavier than He.

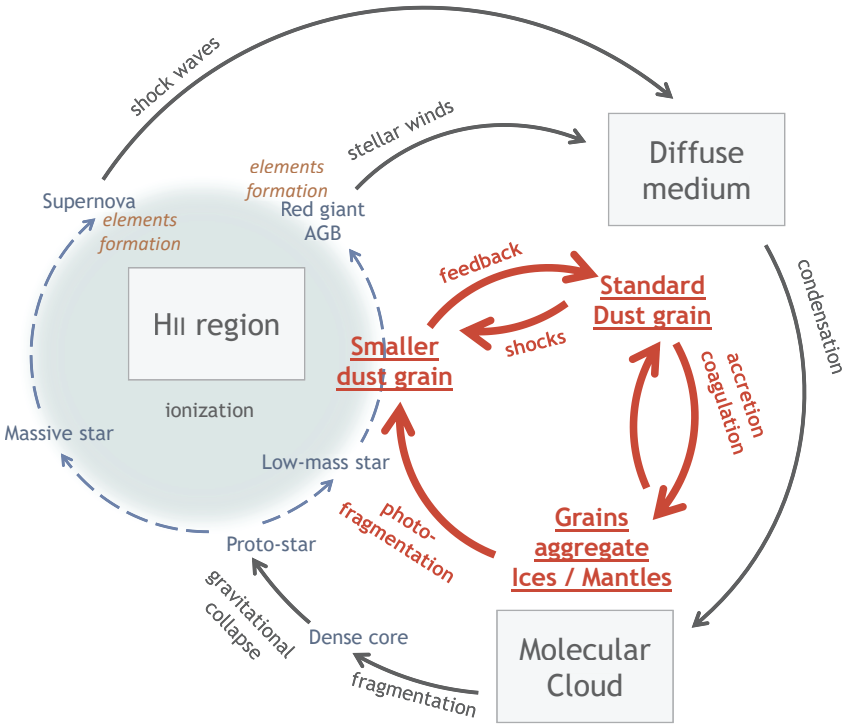

Figure 1.3: Sketch of some processes occurring in the ISM, leading to a recycling of dust grains throughout different phases. Changes in grain sizes are due to interactions with photons or shocks, and agglomerations of several grains.

interactions with other high-energy particles, grains are likely to be sputtered, eroded. If nothing as such is happening, the diffuse ISM will slowly evolve as it is enriched by generations of stars, affecting its chemical composition. At some point, condensation and accretion will gather the dust grains, gluing them together, forming aggregates. This process also impacts the gas, turning a diffuse region into a denser cloud. And so on.

Even though it does not play a large part in the mass budget of a galaxy, the role of the ISM in other processes is rarely negligible. In the Milky Way, only $\sim 10\%$ of the baryons are attributed to the ISM, in the form of gas and dust particles, but in the IR, its contribution in terms of energy budget is much higher.

Although interstellar gas is not at the center of this thesis, here I briefly describe the different gas phases that are distinct, and these phases are used to separate the ISM:

- coronal gas: very hot shock-heated gas running away from supernovae explosion, with multiply ionized atoms;
- ionized H II gas: high temperature ($\sim 10^4$ K) mixture of ions from the ionization of H atoms by UV photons from hot stars; ionized gas can be found either in diffuse clouds, surrounded by a strong radiation that allows ionization, or in H II regions that are denser[2];
- warm H I gas: neutral atomic gas with temperatures up to 5 000 K; it is referred to as warm neutral medium;
- cool H I: neutral atomic gas with lower temperatures of $\sim 10^2$ K; it is referred to as cold neutral medium;

[2]Usually, the estimation of "dense" refers to more than 1000 particles per cm^{-3} and "diffuse", to ~ 100 particles per cm^{-3}

- dense/diffuse H_2 : in these media, the temperature is low ($\sim$ 50 K in diffuse molecular clouds, and down to 10 K in denser regions) with densities high enough to allow formation of H_2 molecules. The H_2 molecule is the main component of cold gas found in dense molecular clouds.

1.3 The Interstellar Radiation Field

The gas and dust filling the ISM evolve under the conditions of the local *interstellar radiation field* (ISRF), which determines their physical state. The ISRF is set by the surrounding stars[3], as well as those distributed further throughout the galaxy. Their age, mass, or metallicity affect this ISRF by the energy they provide. Dust emission depends on the shape and intensity of the surrounding ISRF spectrum. To this day, the ISRF often used in dust modeling of diffuse regions has been taken as that of the solar neighborhood. It is described with three main components (Figure 1.4):

- stars: the starlight from different stellar populations, modeled as a combination of several blackbodies and a UV component. The three blackbodies have different temperatures (3000, 4000, and 7500 K) to depict two stellar populations in the disk, and a population of red giant stars;
- dust emission: the resulting emission of dust grain heated by the photons at lower wavelengths;
- cosmic microwave background (CMB): the remnant emission of the "first light" of the Universe, modeled as a blackbody at $\sim$ 2.73 K;

Mezger et al. (1982) and Mathis et al. (1983) modeled this stellar emission as a function of the distance to the galactic center, $D_{\rm G}$. In most studies, we use the reference at the distance $D_{\rm G} =$ 10 kpc, because it was approximately the estimated distance of our sun from the galactic center at the time. Figure 1.4 shows these spectra at the different distances $D_{\rm G}$ and the decomposition of the reference ISRF, based on the above description.

[3]Sometimes an active galactic nucleus can also be a significant contributor to dust heating, by affecting the ISRF

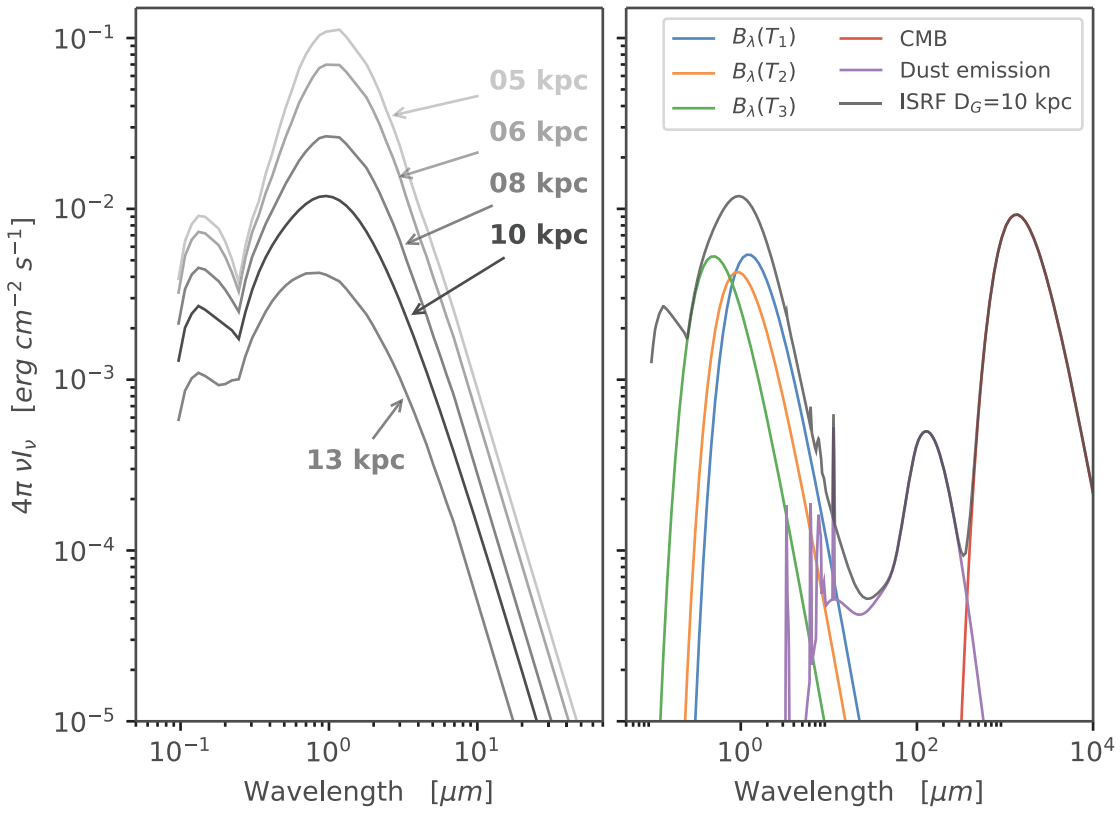

Figure 1.4: *Left:* the stellar contribution of the ISRFs computed by Mezger et al. (1982) and Mathis et al. (1983) at increasing distances $D_{\rm G}$ = 5, 6, 8, 10, and 13 kpc; the one at 10 kpc is used for most studies of dust in diffuse regions. *Right:* a more detailed construction of the ISRFs at $D_{\rm G}$ = 10 kpc: a UV component (not represented); three blackbodies for stellar emission of stars in the galactic disk and a population of red giants; dust emission; and a cold blackbody to account for the CMB.

2 Interstellar Dust

Dust is a key component of the ISM. In this chapter, we will deepen the description of the physical and chemical aspects of interstellar dust. This will lead us to understand how dust models are built and finally how can we detect dust in space.

2.1 Discovery, history and context

The idea of a component capable of absorbing light in space emerged about eighty years ago. Barnard (1910) noticed the obscuration of stars by "something" between them and us, the observers. Trumpler (1930) established that this accentuated attenuation was different than that due to the simple diminution of light due to distance, as it decreased too rapidly. He analyzed peculiar measurements, and concluded that small pieces of material were responsible of such selective extinction. The reddening caused by dust, i.e. the shift in the emitted signal to shorter (*redder*) wavelengths was one of the essential clues of dust grain existence.

Dust is a crucial component of a galaxy for various reasons. First, it is a real chemistry laboratory. For instance, grains hold heavy elements ejected from star cores. As such, it constitutes a reservoir of metals that eventually affects the evidence for evolution of a galaxy. It is also important because of its cooling properties and its nature as a catalyst. Dust grains are formation sites for H_2, mainly forming in the dense gas phase (Le Bourlot et al. 2012). Through its absorbing properties, dust grains serve as cooling material of the ISM. Eventually, they allow for molecular clouds to cool down to the temperature where gravitational collapse can happen, giving birth to stars. Dust also plays an important role in the energy distribution of the ISM. When heated by UV light from stars, electrons released by dust grains can be a major contributor to heating the surrounding gas. The emission process from dust grains, that emit in the infrared to release energy, is an important cooling mechanism, making dust grains a large contributor in the global energy budget and processing of a galaxy. Finally, dust grains can impact the dynamics of the interstellar medium. For instance, they are sensitive to the magnetic field which can have an influence on dust grain orientation.

Studying dust is delicate, and the extent of our knowledge still promises critical progress. Observed dust properties are extremely dependant on the heating sources, and our understanding is thus linked to the observables. Nonetheless, more understanding of dust physics, along

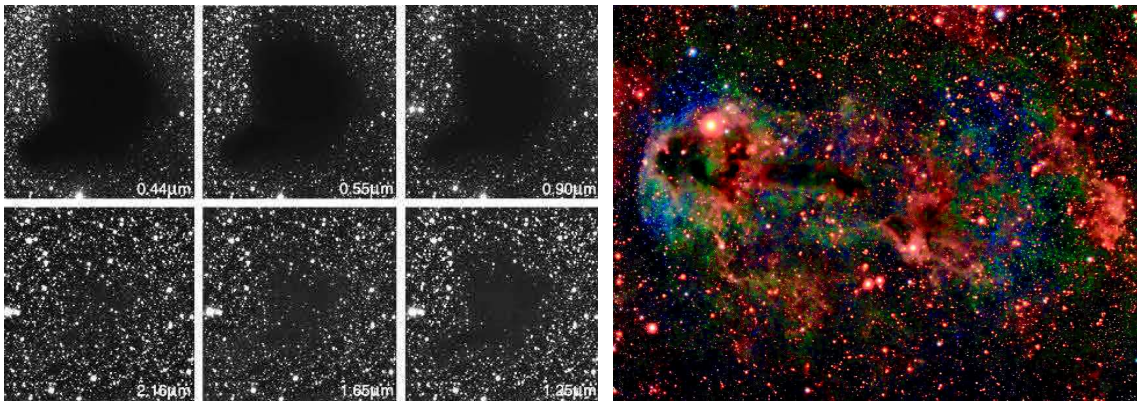

Figure 2.1: *Left:* Barnard68 molecular cloud, nicknamed Dark Cloud, observed at different wavelengths. The absorption efficiency is clearly visible at smaller wavelength (blue), blocking the background light coming from stars behind the cloud. *Credit:* ESO. *Right:* Lynds Dark Nebula 1251, another molecular cloud blocking the starlight. *Credit:* Lynn Hilborn

with progress in technology has lead to a list of observational constraints, whose terms will be explained in the following sections, coupled with laboratories constraints:

- wavelength-dependent attenuation, and albedo;
- features observed in extinction measurements: fixed position of the UV bump and variable width;
- polarization-dependent attenuation;
- emission spectrum;
- cosmic abundance of heavy elements;
- optical and heating properties of condensed matter.

In the following, I describe more thoroughly these observables and dust properties.

2.2 Dust extinction

2.2.1 Some definitions

As aforementioned, one of the first measured characteristics of dust was its ability to absorb light. Dust "attenuates" the stellar light emitted in the UV (young objects) and optical (older stars). Figure 2.1 illustrates this process in the Barnard 68 dark cloud. It is a dense cloud which completely blocks the UV-optical light coming towards the observer. The multi-wavelength picture shows its efficiency depends on the wavelength.

Extinction measurements are usually done with the *pair method*. This consists of measuring the signal of a star free of dust in its surroundings, and the dust-attenuated signal of a similar-type star, at a different position. The former gives the reference measurement for a wavelength. Knowing what the signal from the dusty star should be if no dust were present, we can derive the amount that is removed by dust, and estimate a dust amount.

The intensity passing through a dust cloud at wavelength λ is determined by:

$$I_\lambda = I_{\lambda_0} \times e^{-\tau_\lambda} \tag{2.1}$$

where I_{λ_0} is the original intensity and τ_λ is the optical depth of the medium. The optical depth characterizes the density, i.e. the number of particles, and the capacity of the dust (or gas) to

extinguish light, with respect to their size and properties. It is usually defined with respect to the extinction in the V band ($\lambda \sim 0.55\ \mu$m). We can distinguish two extreme regimes described by the optical depth: when $\tau_\lambda \ll 1$, we refer to the *optically thin* regime, i.e. few particles between the source and the observer; when $\tau_\lambda \gg 1$, we refer to the *optically thick* regime. The original and emerging intensities are related through the extinction term:

$$A_\lambda = -2.5 \log_{10}(I_\lambda / I_{\lambda_0}) \tag{2.2}$$

which can eventually lead to an approximate relation between the extinction and the optical depth:

$$A_\lambda \sim 1.086 \tau_\lambda \tag{2.3}$$

The properties contained in the optical depth, τ_λ, depend on the *extinction cross section*, C_{ext} and the grain radius a. In a homogeneous cloud of dimension l and particle density, n_d:

$$\tau_\lambda = C_{\text{ext}}(a, \lambda)\ n_d\ l \tag{2.4}$$

The grain properties are carried in the *extinction efficiency*, Q_{ext}:

$$C_{\text{ext}}(a, \lambda) = Q_{\text{ext}}(a, \lambda)\ \pi a^2 \tag{2.5}$$

where πa^2 represents the *geometric cross section*.

Absorption and Scattering The extinction is the cumulative effect of two processes called *absorption* and *scattering*. Equation 2.5 can be written:

$$C_{\text{ext}} = C_{\text{abs}} + C_{\text{sca}} \qquad \text{and} \qquad \begin{cases} Q_{\text{abs}} \equiv C_{\text{abs}} / \pi a^2 \\ Q_{\text{sca}} \equiv C_{\text{sca}} / \pi a^2 \end{cases} \tag{2.6}$$

where C_{abs} and C_{sca} are the absorption cross section and scattering cross section, respectively, and Q_{abs} and Q_{abs} are the absorption and scattering efficiencies, respectively.

Dust grains have the ability to absorb photons. This process leads to an increase of the internal energy of the grain (equivalent to a raise of its temperature). Eventually, the grain re-emits the energy it absorbed, but at longer wavelengths, in the infrared.

Scattering is the change of direction of propagation of a photon after it hits a dust grain. The photon has the same energy, but is not observable in the same direction. Scattering is most visible in what is called *reflection nebulae*, for which Figure 2.2 shows an example where a cloud is illuminated by a star. The light we collect comes from the reverberation of the stellar light on the dust particles of the cloud. Such situations provide measurements of the *albedo*, defined as the contribution of scattering compared to the total extinction:

$$albedo = \frac{C_{\text{sca}}}{C_{\text{ext}}} \tag{2.7}$$

The albedo is thus an interesting property because it can be measured (e.g. Lewis et al. 2009), and provides an additional constraint for theoretical dust grain models. However, some works (e.g. Mathis et al. 2002) have showed that, even though we can measure extinction as well as and scattering in nebulae like that in Figure 2.2, constraining dust properties, and especially their geometry, is very difficult and uncertain.

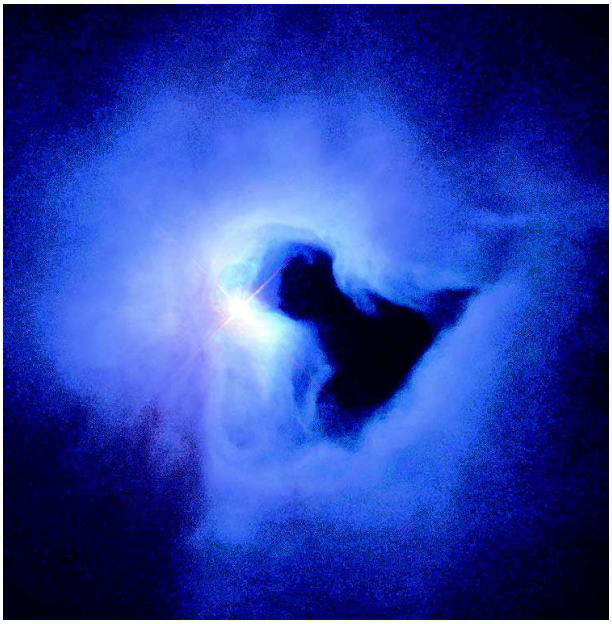

Figure 2.2: Reflection nebula NGC1999: the bright star V380 Orionis, behind the dust and gas cloud, illuminates the nebula, which preferentially scatters blue light, hence the color. *Credit:* Hubble Heritage Team and NASA.

2.2.2 Dust physics properties

The absorption and scattering properties of dust are crucial elements to know in order to build a dust model. The efficiencies Q_{abs} and Q_{sca} carry the information of dust grains. They both depend on the incident wavelength and grain composition, size, and to some extent, temperature. Efficiencies can be either measured in laboratories, using synthetic dust grains or samples, or calculated, by solving Maxwell's equations of the propagation of electromagnetic waves through a system. There are different approaches to determine these efficiencies numerically, and different regimes.

Under an electric field $E = E_0 \, \mathrm{e}^{-i\omega t}$, with ω the response frequency, we note the response of a solid material, ε, as an imaginary number:

$$\varepsilon = \varepsilon_1 + i\varepsilon_2 \tag{2.8}$$

where ε_1 and ε_2 are its real and imaginary parts, respectively. We also define $\lambda = 2\pi c/\omega$, where c is the speed of light. In case of polarized grains, the applied electric field generates a dipole moment:

$$\boldsymbol{P} = \alpha \boldsymbol{E} \tag{2.9}$$

where α is the electric polarizability of the grain. It is an intrinsic property of matter and provides insight into the nature of the material. Analytic solutions to this problem are known for the whole family of ellipsoidal grains. Here, we will only write the equations for a particular case: spheres. Under that assumption, we can distinguish two regimes to determine the absorption and scattering cross sections.

In the case where $a \gg \lambda$, the grain fully blocks the photons, and we have:

$$\begin{cases} C_{\text{abs}} \sim 1 \\ C_{\text{sca}} \sim 1 \end{cases} \tag{2.10}$$

If $a \ll \lambda$, we call this regime the *Rayleigh limit* or the *electric dipole limit*. In this case, the electric field appears uniform to the small grains, and the cross sections are:

$$\begin{cases} C_{\text{abs}} = \dfrac{4\pi\omega}{c}\,\text{Im}(\alpha) \\ C_{\text{sca}} = \dfrac{8\pi}{3}\left(\dfrac{\omega}{c}\right)^4 |\alpha|^2 \end{cases} \tag{2.11}$$

And we can link this to the response ε (Equation 2.8):

$$\begin{cases} C_{\text{abs}} = 18\pi\,\dfrac{\varepsilon_2}{(\varepsilon_1+2)^2+\varepsilon_2^2}\,\dfrac{V}{\lambda} \\ C_{\text{sca}} = 24\pi^3\left|\dfrac{\varepsilon-1}{\varepsilon+2}\right|^2\dfrac{V^2}{\lambda^4} \end{cases} \tag{2.12}$$

with V, the volume of grain material. We can note that, for very small grains, and still in the case where $a \ll \lambda$, as $V \to 0$, $C_{\text{abs}} \gg C_{\text{sca}}$: absorption prevails over scattering.
In the same regime, at long wavelengths ($\lambda \to \infty$ or $\omega \to 0$), we can write:

$$\begin{cases} C_{\text{abs}} \xrightarrow[\omega\to 0]{} f_{\text{abs}}\,\dfrac{V}{\lambda^2} \\ C_{\text{sca}} \xrightarrow[\omega\to 0]{} f_{\text{sca}}\,\dfrac{V^2}{\lambda^4} \end{cases} \tag{2.13}$$

with f_{abs}, f_{sca} functions depending on the insulator or conductor nature of the grain:

$$\begin{cases} \begin{cases} f_{\text{abs}} &= f_{\text{abs}}(\varepsilon_0) \\ f_{\text{sca}} &= f_{\text{sca}}(\varepsilon_0) \end{cases} & \text{if insulator} \\ \begin{cases} f_{\text{abs}} &= f(1/\sigma_0) \\ f_{\text{sca}} &= \text{constant} \end{cases} & \text{if conductor; } \sigma_0 \text{ is the grain conductivity} \end{cases} \tag{2.14}$$

At long wavelengths, material with high σ_0 will be a poor absorber as $C_{\text{abs}} \to 0$. Figure 2.3 shows an example of the extinction efficiencies for two types of grains, illustrating the λ^{-2} behaviour. A very common example of this phenomenon is our daily blue sky, due to the Rayleigh scattering at long wavelengths of sunlight by the particles in the atmosphere.

If the grain size is comparable to the wavelength, the previous solutions are not valid, and the resolution of the Maxwell's equations is not the same. The *Mie theory*, introduced by G. Mie and P. Debye around 1908, offers new solutions to this particular case. Then, the response of the grain will depend on the ratio a/λ and its refractive index. As the incident electric wave travels through the grain, the *phase shift* occurring after a distance a within the grain is an important parameter to estimate the absorption and scattering cross sections of the grain.

We should also notice the importance of the spherical material assumption on the previous development. This is a strong simplification that could have important consequences when confronted with observations. The discrete dipole approximation (DDA; Purcell & Pennypacker 1973) is an approach to avoid considering dust particles as spheroids. It is, however, very complex, and requires numerical calculations. The spheres approach is much faster, and is used by most of the models to this day.

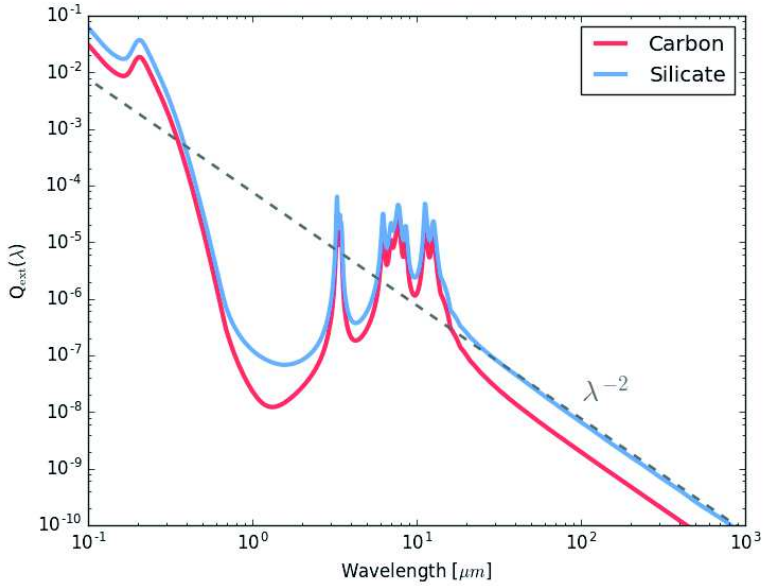

Figure 2.3: Extinction efficiencies (absorption and scattering combined) for carbonaceous and silicate grains, in THEMIS (Jones et al. 2013; Köhler et al. 2014; Ysard et al. 2015)

2.2.3 Measurements of dust extinction

Empirically, variations of the extinction with wavelength can be summarized with an *extinction curve*. Cardelli et al. (1989) showed that the averaged extinction curves measured in the Milky Way could be parameterized simply with

$$R_V = A_V / E(B-V) \tag{2.15}$$

The indices B and V refer to the bands at 0.44 and 0.55 μm, respectively; the *reddening* $E(B-V)$ is the difference between the extinctions in these two bands. The same authors showed that the ratio $A_\lambda / A_{\lambda_{\rm ref}}$ can be completely parameterized by seven parameters, and if R_V is known, it can be parameterized by a one-parameter function.
Figure 2.4 shows average extinction curves in the MW with varying R_V) from Fitzpatrick (1999). A particular discrepancy between these curves can be noticed: the bump around 4.5 μm^{-1} ($\sim$ 217 nm). It is a well known feature of dust extinction, far from being well understood, conveniently called the *2175 Å feature*. Its position seems invariant but significant width variations have been observed (Beitia-Antero & Gómez de Castro 2017). Moreover, it appears absent in some lines of sight. If current evidence points towards a transition in graphite or small aromatic hydrocarbons, its origin remains uncertain.

2.2.4 The Diffuse Interstellar Bands

The terms *diffuse interstellar bands*, or DIBs, refer to a series of extinction features, weak and broad. Their width indicates that they are not atomic absorption lines but rather emerge from large molecules. To this day, about 400 DIBs have been compiled, from 3900 Å to the NIR (Hobbs et al. 2009). It is important to admit that until very recently, none of these lines were ever assigned to a molecule. Figure 2.5 shows a compilation of several DIBs on the spectrum.

Although identified about 90 years ago, and classified as interstellar about a decade later (Heger 1922; Merrill & Wilson 1934; Merrill 1934) , only one idea has yet be proven right: *buckminsterfullerene*!

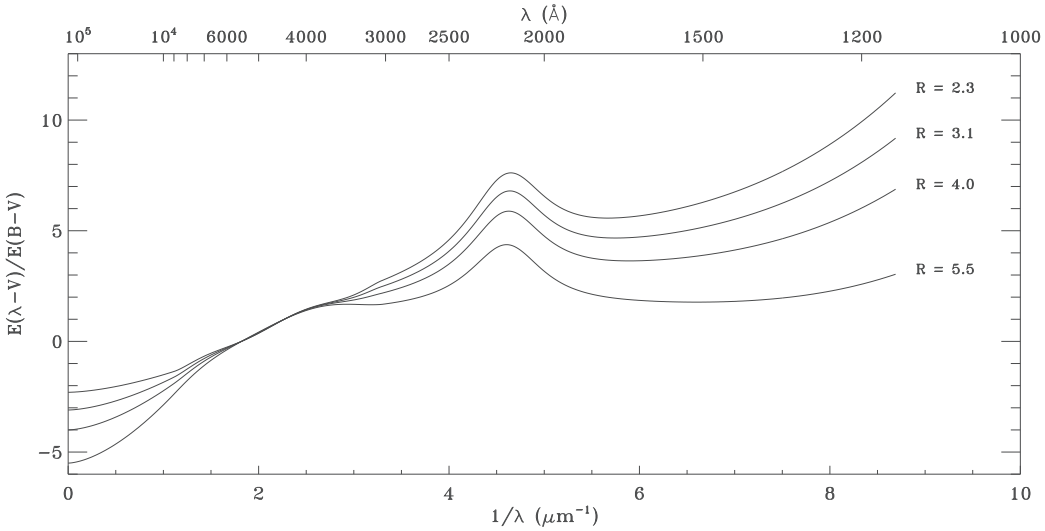

Figure 2.4: A few extinction curves of the Galaxy from the work of Fitzpatrick (1999). They modeled extinction with a R ($\equiv R_V$) parametrization.

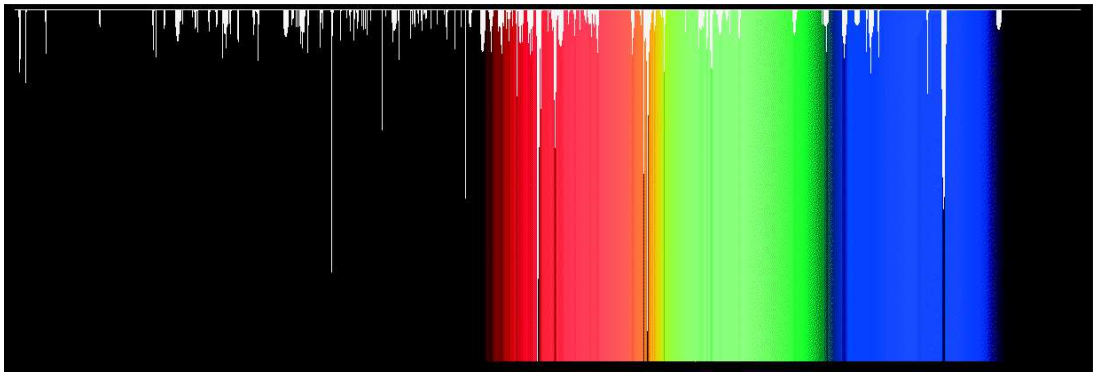

Figure 2.5: Cropped spectrum showing some Diffuse Interstellar Bands, after compilation from Jenniskens & Desert (1994) work. *Credit:* http://www.kroto.info/dibs/

This cage-like molecule, composed of 60 carbon atoms and noted C_{60}, resembles a football. In the late 80s, after a serendipitous discovery of C_{60} presence in space, its positively ionized ion was predicted to be a DIB carrier by Kroto & Jura (1992). Around 1995, two bands are strongly suspected to be due to C_{60}^+. In 2015, a team conclusively identifies C_{60}^+ as the carrier of two DIBs, at 9577.4 and 9632.6 Å, thanks to an extremely low temperature experiment, that allows the observations of molecules under 6 K (Campbell et al. 2015).

2.3 Dust emission

After absorbing the incident light in the UV and optical, dust grains re-emit this energy in the infrared (from mid-infrared to sub-millimetric wavelengths). This emission also depends on the dust grain size and composition, and the shape and intensity of the incident interstellar radiation field, its strength and hardness (see Section 1.3).

2.3.1 Thermal equilibrium

A grain large enough in a radiation field will absorb enough photons to be subject to a constant input of energy, and will re-emit that energy at the same rate. In that particular state, the grain is in equilibrium with the heating rate[1]. The absorbed energy, $E_{\rm abs}$, is:

$$E_{\rm abs} = \int_0^\infty 4\pi\, n_{\rm d}\, \pi a^2\, Q_{\rm abs}(\lambda, a)\, J_\lambda\, {\rm d}\lambda \tag{2.16}$$

where $n_{\rm d}$ is the number density of grains, and J_λ is the mean intensity of the interstellar radiation field. and we have energetic equality between emission and absorption, leading to:

$$\int_0^\infty Q_{\rm abs}(\lambda, a)\, J_\lambda\, {\rm d}\lambda = \int_0^\infty Q_{\rm abs}(\lambda, a)\, B(\lambda, T_{\rm d})\, {\rm d}\lambda \tag{2.17}$$

The term $B(\lambda, T_{\rm d})$, or $B_\lambda(T_{\rm d})$ for simplification, is the Planck function at wavelength λ and dust temperature, $T_{\rm d}$:

$$B_\lambda(T_{\rm d}) = \frac{2\pi {\rm c}^2}{\lambda^5} \frac{1}{{\rm e}^{\frac{\rm hc}{{\rm k_B}\lambda T_{\rm d}}} + 1} \tag{2.18}$$

where c is the speed of light, h is the Planck constant, and $\rm k_B$ is the Boltzmann constant.

The grain emission however, is not a perfect blackbody, and is often referred to as a *modified blackbody*. The modification lies in the *emissivity* of the dust grains. The surface brightness, S_λ, from a grain is:

$$\begin{aligned} S_\lambda &= \tau_\lambda\, B_\lambda(T_d) \\ &= {\rm n_d}\, \pi a^2\, Q\, B_\lambda(T_d) \\ &= \frac{\Sigma_{\rm d}}{m_{\rm d}}\, \pi a^2\, Q\, B_\lambda(T_d) \qquad \text{with } m_{\rm d} = \frac{4}{3}\pi a^3 \rho \\ &= \kappa_\lambda\, \Sigma_{\rm d}\, B_\lambda(T_d) \end{aligned} \tag{2.19}$$

where τ_λ is the dust optical depth; $\rm n_d$ is the number of grains, or dust column density; $\Sigma_{\rm d}$ is the dust surface density; ρ the grain density; $m_{\rm d}$ is the dust grain mass; and κ_λ is grain absorption cross section per unit mass, characterizing the power of a dust grain to absorb/emit, at a given wavelength.

[1] The equilibrium state can be achieved for small grain under the condition of a strong enough radiation field. However, it is usually admitted, from empirical situations, that mostly large grains are found to be in the equilibrium state.

Wien's law In the case of thermal equilibrium, it is possible to coarsely assess the peak of radiation for large grain, using Wien's law. It predicts:

$$\lambda_{\max} T_{\rm d} \sim 3000 \ \mu{\rm m\ K} \tag{2.20}$$

where $\lambda_{\max}$ is the wavelength at which the emission peaks. For instance, it means that dust grains at temperature ~ 30 K will have an emission peak at $\sim 100\ \mu$m.

Stefan-Boltzmann's law In the case of a blackbody, the law of Stefan-Boltzmann predicts that the power emitted is proportional to T^4. In the case of grains in the equilibrium, i.e. emitting all the power they receive, we can connect this with the surrounding heating power, U (from surrounding stars; see Section 1.3):

$$U \propto T^{4+\beta} \tag{2.21}$$

where β is the spectral index of the dust grains. We therefore expect a large increase in luminosity as the temperature rises. If we use the temperature of dust in the solar neighborhood, we can derive a dust temperature knowing the local heating environment:

$$T_{\rm d} \propto T_{\rm d\odot} \left(\frac{U}{U_\odot} \right)^{\frac{1}{4+\beta}} \tag{2.22}$$

Recent results The space telescope *Planck* observed the universe from a few hundreds of microns to centimeter wavelengths. The Planck collaboration modeled the dust emission with *Planck* data and found T_d between 16 and 24 K and $\beta = 1.51$ (Planck Collaboration et al. 2014, see also, Section 2.7).
The Hi-GAL mission (Herschel Open Time Key-Project Molinari et al. 2010) mapped the Galactic plane (-1°< b < 1°) between 60 and 600 μm . Paradis et al. (2012) used this project for ISM studies and found dust temperatures between 16 and 25 K in this region, varying as the distance from the Galactic center increases.

2.3.2 Stochastic heating

Thermal emission applies to grains whose size is sufficient to absorb photons continuously. In the opposite case, if the grain is too small that it absorbs photons irregularly, we refer to a *stochastic heating* process. We no longer consider the power emitted by the dust grain as a blackbody, but as an average of the heat capacity of the grain, $C(T)$, over a timescale. Due to absorption of individual photons, the grain temperature profile shows rapid spikes, and a slow decay toward lower temperatures. Every new photon absorbed creates a new raise in temperature, primarily due to a small heat capacity, as shown in Figure 2.6. It illustrates the temperature in spikes, over a few lifetimes of grains at various sizes, and increasing time between grain-photon interactions, $\tau_{\rm abs}$. It shows that, if the grain is too small, it undergoes strong peaks in temperature, and a more gradual cooling, until it gets hit by a photon again. It depicts the stochastic heating of small grains.

Instead of deriving an effective temperature, as for larger grains, we use a probability distribution of temperatures:

$$\int_0^\infty P(a,T)\ {\rm d}T \qquad \text{with } P(a,T) = P(a, T_{\rm grain} \leq T) \tag{2.23}$$

Figure 2.7 shows the peaks in temperature, for various grain sizes. We see that the smaller the grain, the broader the temperature distribution. Only when the grain radius reaches a sufficient size can we estimate a grain temperature.

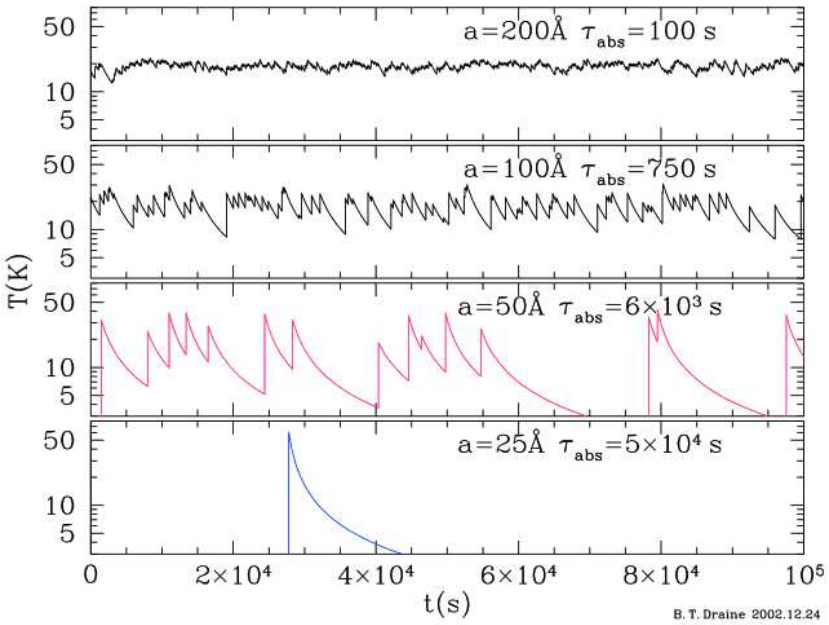

Figure 2.6: Temperature fluctuations of dust grains, during $\sim$ 1 day. Each peak comes from a photon absorption: if the grain radius a is too small, the grain undergoes a gradual cooling (bottom panel), instead of keeping a rather constant temperature (top panel). From Draine (2003a).

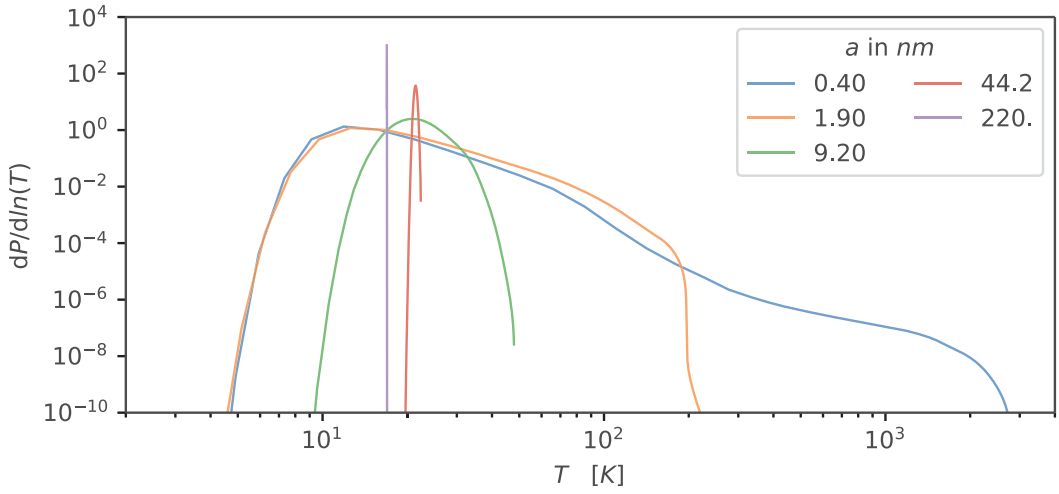

Figure 2.7: Temperature probability distributions of a few grains at different radii a. If the grains are big enough, the probability is peaked, defining a unique grain temperature, as opposed to a small grain.

	λ (μm)	Identification
		Known lines
	3.30	Aromatic C-H stretch
	6.22	Aromatic C-C stretch
	8.61	C-H bending, in-plane
		Complexes
	7.417	Aromatic C-C stretch
7.7	7.56	Aromatic C-C stretch
	7.85	C-C stretch + C-h bending
11.3	11.23	C-H bending, out-of-plane
	11.33	C-H bending, out-of-plane
	17.04	*C-C-C bending*
17.0	17.38	*C-C-C bending*
	17.87	*C-C-C bending*
		Empirical
	5.27	C-H bend + C-H stretch
	5.70	C-H bend + C-H stretch
	6.69	*unknown*
	13.5	*C-H bending, out-of-plane*
	14.2	*C-H bending, out-of-plane*
	15.9	*unknown*
	18.9	*C-C-C bending*

Table 2.1: Identification (or proposed specie, in italic) of some spectral lines, attempting to describe the emission features in the range of $1-20$ μm. Adapted from Draine & Li (2007)

2.3.3 Aromatic-rich (cyclic) carbonaceous

The emission in the mid-infrared, in the range $\sim 1-20$ μm, shows typical features that arise from vibration modes of cyclic hydrocarbon grains. They are characteristic of transitions of these large molecules and can be identified for the most part. Leger & Puget (1984) and Allamandola et al. (1985) identified the main features as:

- 3.3 μm: C - H stretching;
- $6.2, 7.7$ μm: C - C stretching;
- $8.6, 11.3$ μm: C - H bending.

However, the reality is more complicated. Some of these lines are complexes, encompassing the combined emission of multiple signals. Some features are seen in laboratories but not in observed spectra while some are seen in observations but their origins remain unknown. Draine & Li (2007) give a more complete description of these features and we gather a few of the characteristic features in Table 2.1.

Latest news: Stock & Peeters (2017) modeled the 7.7 μm complex with four Gaussian distributions, instead of three as has usually been done. This would imply a fourth component in the complex. That is not yet included in Table 2.1

Element	N_X/N_H	Element	N_X/N_H
C	$2.69\ 10^{-4}$	Si	$3.23\ 10^{-5}$
N	$6.76\ 10^{-5}$	S	$1.32\ 10^{-5}$
O	$4.90\ 10^{-4}$	Mn	$2.69\ 10^{-7}$
Mg	$3.98\ 10^{-5}$	Fe	$3.16\ 10^{-5}$

Table 2.2: Solar abundances adapted from Asplund et al. (2009).

2.4 Elemental abundances and dust composition

The dust emission and extinction are dependent on the chemical nature of the material. It is thus a necessity to know what dust grains are made of, in order to understand the interstellar observables. Experimental measurements in laboratories allow us to derive optical and heating properties from grains of various sizes and nature.

The extinction theory and measurements we explained previously serve as a baseline to estimate the chemical composition of dust grains. From extinction measurements, it is possible to estimate the total volume occupied by grains with respect to that of hydrogen atoms. From here, a lower limit on the $M_{\rm dust}/M_{\rm H}$ (where $M_{\rm dust}$ is the total dust mass and $M_{\rm H}$ is the hydrogen mass) ratio can be derived, which depends on the grain density ρ and a shape factor F:

$$\frac{M_{\rm dust}}{M_{\rm H}} \gtrsim 0.0056 \left(\frac{1.2}{F}\right)\left(\frac{\rho}{3\ {\rm g\ cm^{-3}}}\right) \tag{2.24}$$

However, H and He atoms locked in grains do not contribute a lot to the mass of these grains. To reach such ratio, it is essential to add element such as C, O, Mg, Si, S or Fe. Assumption is made that the total interstellar abundance of an element is the sum of its quantities in the gas phase and in the solid phase. From spectroscopic measurements, we can measure the elemental abundances in the gas phase. The dust elemental abundance is thus the difference between the total and gas phase measurements:

The term $[\frac{X}{\rm H}]_{gas}$ is called *depletion* of element X from the gas phase. It is estimated as the difference between the observed abundance of the element X and that we would expect if the atoms were all in the gas phase:

$$\left[\frac{X}{\rm H}\right]_{gas} = \log\left(\frac{N(X)}{\rm N(H)}\right) - \left[\frac{X}{\rm H}\right]_{\rm solar} \tag{2.25}$$

where $N(X)$, N(H) are the volume densities if an element X and hydrogen, respectively, and $[\frac{X}{\rm H}]_{\rm solar}$ is the depletion of the element X from the gas phase in the solar neighborhood. Still using spectroscopy, observations of absorption features, combined with molecular and atomic data, allow the identification of the corresponding materials. For example, absorption lines at 9.7 μm and 18 μm have been identified as $\rm Si-O$ and $\rm O-Si-O$ stretches. Combined with the typical "broad and smooth" aspect of the absorption spectrum, we can strongly suspect the presence of amorphous silicate in dust, instead of crystalline material. We are eventually able to narrow down the possible solids describing dust grains: silicate in the form of pyroxene ($\rm Mg_xFe_{1-x}SiO_3$) or olivine ($\rm Mg_{2x}Fe_{2-2x}SiO_4$), oxides of metals ($\rm SiO_2$, MgO, $\rm Fe_3O_4$), hydrocarbons, carbide (SiC)... There is a restriction, however, to the information spectra can give: absorption lines can only be recovered for atoms or small molecules. In the case of interstellar dust, it is expected to find more complex material (like the silicates), and spectroscopic evidence is therefore limited.

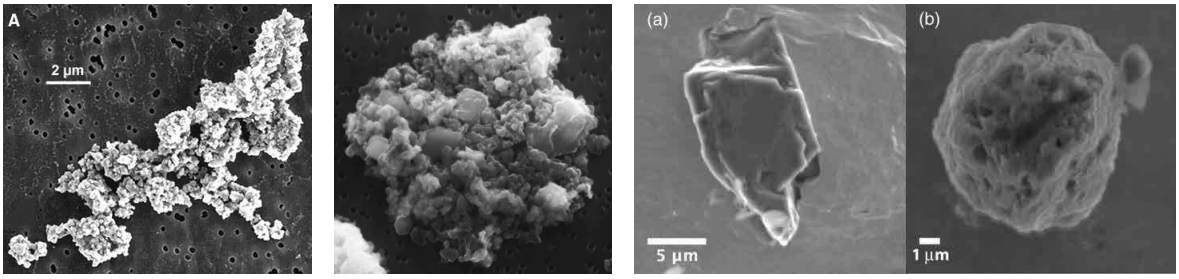

Figure 2.8: Dust grains seen with electron microscopes. *Left:* Chondritic grain, i.e. found in a meteorite. *Credit:* Bradley et al. (2005). *Middle:* Aggregate of silicate and carbonaceous matter on a grain, probably chondritic. *Credit:* Volten et al. (2007). *Right:* Two images of SiC grains: (a) may be a fragment, while (b) appears to be a whole condensate. *Credit:* Heck et al. (2009)

Very few "real" interplanetary grains have been collected by spacecrafts in the Earth surroundings, or further away. They are used to conduct direct laboratories measurements. Figure 2.8 shows a few example of these grains. The most striking information conveyed here is the (strongly) non-spherical aspect of the grains. Current models almost all assume spheres for efficient calculations. Such assumption underestimates the emissivity properties of dust grain, since their surface is, in fact, much larger. Also, these grains are very big compared to the limits imposed on ISM dust grains. It is possible that interplanetary dust grains are conglomerates of smaller interstellar grains.

New Horizons Student Dust Counter: during its flyby to Pluto, the instrument designed to collect and analyze dust grains on the fly was hit by only "six particles per cubic mile"; this is an indication on how rare the grains can be in our very close neighborhood.

2.5 Grain sizes

Minimal and maximal dust grain sizes are estimated through many observational constraints. Based on extinction measurements, scattering of visible light and polarization observations, we know that grains must cover a large size distribution, from ~ 0.01 to 0.2 μm. Emission features tell us that smaller grains are required to reproduce observations, with sizes down to ~ 0.003 μm. Recent dust models, detailed in the following section, use that information to create dust grain size distributions matching those measurements.

2.6 Dust grain models

Modeling dust emission and extinction is critical, and the properties and methods described above are used to build dust models. At each grain size and grain composition, we know the laws predicting the extinction and emission, through theoretical calculations and laboratory measurements. Despite this information, to this day, there is not a unique model able to reproduce the observations. However, using this knowledge, numerous studies have focused on the inverse problem: with extinction and emission measurements from nearby and distant galaxies, what can we derive on the composition and size distribution of dust grains from regions far away?

In Section 2.3.1, we saw that the emission of large grains in thermal equilibrium can be approximated by a blackbody, with a few changes. To build simple dust models taking into account only the large grain distribution, we can change the term κ_λ with different approaches, which modify the blackbody spectrum. Two "common" methods to attribute a change to κ_λ are the *Simple Modified Blackbody* (SMBB)and the *Broken-Emissivity Modified Blackbody* (BEMBB). Gordon et al. (2014) defined properties of the SMBB as:

$$\begin{cases} \kappa_\lambda^{\mathrm{SMBB}} = \kappa_{\lambda_0}^{\mathrm{eff}} \left(\dfrac{\lambda}{\lambda_0}\right)^{-\beta} \\ \kappa_\lambda^{\mathrm{BEMBB}} = \kappa_{\lambda_0}^{\mathrm{eff}} \dfrac{1}{\lambda_0^{-\beta_1}} \begin{cases} \lambda^{-\beta_1} & \text{if } \lambda < \lambda_b \\ \lambda_b^{(\beta_2-\beta_1)}\, \lambda^{-\beta_2} & \text{if } \lambda \geq \lambda_b \end{cases} \end{cases} \tag{2.26}$$

β typically ranges between 1 and 3, according to laboratories measurements, and most studies assumed a value of 2 (Henning & Mutschke 1997; Demyk et al. 2017). This is directly related to the Q_{abs} and Q_{sca} properties (see Section 2.2).

However, we know from MIR emission that there must be smaller grains that are responsible for the emission features at shorter wavelengths. To model those, we need a complete model with grain size distributions. The first dust model was developed in the 1940s (Oort & van de Hulst 1946). The solid phase was, at the time, described as 'smoke', an ensemble of small particles of a few microns in radius, and smaller. This smoke would contribute to the global extinction visible in space.

Mathis et al. (1977) used power-law size distributions to describe silicate and graphite populations to fit the observed extinction. After pioneer work from Platt (1956) and Donn (1968), the PAHs became acknowledged as responsible of many extinction and emission features, and models started adding a third component to the dust composition: Desert et al. (1990); Draine & Li (2001); Li & Draine (2001); Weingartner & Draine (2001); Zubko et al. (2004); Draine & Li (2007).

In most cases, these models vary from one another by the size distributions they use. The difference in composition can be minor (e.g. different extinction efficiencies) or carry greater consequences, like the use of different carbonaceous molecules: amorphous versus crystalline (graphite, diamond). All of these models manage to fit the Milky Way dust extinction and emission, and lie within acceptable abundances. The free parameters vary from a model to another, and it is an important point to study: which parameter are degenerate? Which parameters are kept fixed and why? These questions are the very reasons for the work presented in this thesis.

In this thesis, we will use three of these models in particular. A more explicit description is needed, in order to understand the differences that exist between models.

2.6.1 Draine & Li (2007)

The Draine & Li (2007) model (hereafter, DL07) originally stems from the model built by Draine & Lee (1984). It is a natural extension of the first *graphite-silicate* model, as new constraints brought new insights on dust modeling. Cross sections used in DL07 come from Draine & Lee (1984), who showed that their composition could fit the dust observables. A significant input was done by Draine & Li (2001) and Li & Draine (2001) by adding PAHs to the carbon grain distribution, after identification of their emission features in the mid-IR. Draine & Li (2001) also updated heat capacities. The "current" DL07 model uses an updated size distribution following the extensive work from Weingartner & Draine (2001). Minor changes based on more recent work and new assumptions bring revisions to this model, which is, to this day, the most frequently used in IR dust modeling.

2.6.2 Compiègne et al. (2011)

The Compiègne et al. (2011) model, or for further simplification, the DustEM model, also follows a family of dust models, its parent being that from Desert et al. (1990). The Desert et al. (1990) model described dust with three components: PAHs, very small grains, and big grains. The DustEM model is more precise in its description, and uses five components; the PAH population is split between neutral and ionized molecules; the carbonaceous grains, amorphous, are divided between a small and a large populations; finally, the silicate component only uses large grains. The small grain sizes are computed with a log-normal distribution while the large carbon and silicate grains are determined to have a power-law distribution. The carbonaceous populations are based on Zubko et al. (1996) and the silicate properties come from Draine & Lee (1984); they are "astronomicalised" to be compatible with sub-mm observations and are therefore more empirical, based on works from Li & Draine (2001), Draine (2003b) and Draine & Li (2001). An important point is the common spectral index of both large carbonaceous and silicate grains. The PAHs cross sections are slightly modified from Draine & Li (2007).

2.6.3 THEMIS

Another model has recently been developed by Jones et al. (2013). Based on a series of new laboratory measurements from Jones (2012c,d,a,e,b), and updated by Köhler et al. (2014) and Ysard et al. (2015), it is named THEMIS for The Heterogeneous Evolution dust Model at the IAS[2]. Its particularity, besides taking into account laboratory data, is to take into account the PAH-like material in the form of mantles around the dust grains. In this model, the smallest grains are only aromatic-rich, while large carbonaceous grains have an aliphatic-rich core, covered by an aromatic mantle, just like silicate-core grains. The difference between aromatic and aliphatic lies in the crystal organization, leading to more or less H atoms. Further work have also added ices to this model: it enables grain aggregation in very dense regions, such as molecular clouds.
Because it is heavily based on laboratory data, this model is not exactly fit to the same observations as the other models. However, Ysard et al. (2015) adjusted the dust masses and density to be able to reproduce the different ISM phases in the MW.
The model is therefore described by two grain populations, split into four components; the carbonaceous material is divided between a small grain population, aromatic-rich, and a large grain population with aliphatic cores and aromatic mantles. The metals are locked into two silicate-based compositions: pyroxene $(SiO_3)_2$ and olivine (SiO_4).

2.6.4 Calibration

Most dust models are calibrated on measurements done in the MW, and more precisely in the local neighborhood. It is where our constraints have the lower uncertainties, even though it represents only one sample. For example, the DustEM model uses a combination of extinction and emission to adjust their model. The extinction curve is that of $R_V = 3.1$ from Fitzpatrick (1999). The total emission spectrum used to calibrate DustEM is a compilation of many observations from the near-IR to the submillimetric wavelengths. It covers a large portion of the sky at high galactic latitude ($|b| > 15°$), in order to select the *diffuse ISM* of our Galaxy (see Compiègne et al. 2011, for a compilation).
Additional information is used from depletion measurements. It helps to estimate a limit on the

[2]Institut d'Astrophysique Spatiale (Paris, France)

quantity of each element to put in the grain composition. Jenkins (2009) carried out extensive work on depletions which are used today.
Other galaxies have been used to constrain models. For instance, Weingartner & Draine (2001) built dust models, in particular size distributions based on fits of the Magellanic Clouds, two nearby galaxies (see Section 4).

2.7 Observations and Instruments

To confront theoretical models with "reality", we need measurements that will constrain the emission, extinction and abundances in samples of galaxies of various shapes, dynamics, or ages... Here is a short history of space telescopes used in IR studies.

Infrared measurements have to be taken from space. The atmosphere surrounding the Earth blocks infrared photons and therefore prevents ground based IR measurements. The Infrared Astronomical Satellite (IRAS; Neugebauer et al. 1984) was launched in 1983, for a mission that lasted 10 months. It was the first space observatory to observe the full-sky at four infrared wavelengths: 12, 25, 60 and 100 μm. The Cosmic Background Explorer (COBE) was launched in 1989; its main goal was to observe the microwave background emission, but two of its instruments (DIRBE and FIRAS) took measurements of the sky in infrared wavelengths. In 1995, the European Space Agency (ESA) launched the Infrared Space Observatory (ISO), for observations between 2.4 and 240 μm.

More recent space observatories have had an incredible impact on modern astrophysics, and this thesis is mainly based on measurements from these telescopes. The level of precision in IR observations was largely increased with the *Spitzer* Space Telescope (Werner et al. 2004) launched in 2003, whose main mission ended in 2009 (the "warm" mission is still ongoing at the two shortest wavelengths). It was not a full-sky survey, but pointed observations, as was ISO. *Spitzer* carried 3 instruments to orbit. Among these, two are for photometry, IRAC (Infrared Array Camera; Fazio et al. 2004) and MIPS (Multiband Imaging Photometer for Spitzer; Rieke et al. 2004). IRAC photometric bands are centered on 3.6, 4.5, 5.8, and 8.0 μm, and MIPS bands on 24, 70, and 160 μm. The spectrometer, IRS (Infrared Spectrograph; Houck et al. 2004), covered 5 to 38 μm, with both high and low resolutions. The science questions that *Spitzer* was built to tackle were, among others, star formation or young stellar objects as well as dust, given its spectral coverage. Some programs used *Spitzer*, making significant contributions in dust analysis in nearby galaxies. The SINGS consortium (Kennicutt et al. 2003) took measurements of 75 galaxies and focused on their IR emission and star formation properties. Two programs were meant to study in detail regions of the Small Magellanic Cloud (SMC), a nearby dwarf galaxy, in photometry and spectroscopy (S^3MC, S^4MC; Bolatto et al. 2007; Sandstrom et al. 2012). The SAGE surveys (SMC and LMC; Meixner et al. 2006; Gordon et al. 2011) were keys projects of the *Spitzer* program and are used in numerous studies.

The *Herschel* Space Observatory (Pilbratt et al. 2010) was launched in 2009, and remained functional until 2013, working as a pointed instrument as well, and operating from the L2 point. Its photometry channels covered 6 bands, split between two instruments. PACS (Photoconductor Array Camera and Spectrometer; Poglitsch et al. 2010) covered 70, 100, and 160 μm, and SPIRE (Spectral and Photometric Imaging Receiver ; Griffin et al. 2010) covered 250, 350, and 500 μm. PACS also allowed for spectroscopy between 55 and 210 μm a moderate resolution; the HIFI spectrometer worked between 157 and 625 μm. Since its coverage was in the IR, *Herschel* was almost fully dedicated to the study of interstellar dust. Numerous studies have used *Herschel* state-of-the-art resolutions and a lot of studies continue. One of the main programs useful for us is HERITAGE (Meixner et al. 2013, 2015), which focused on dust in the

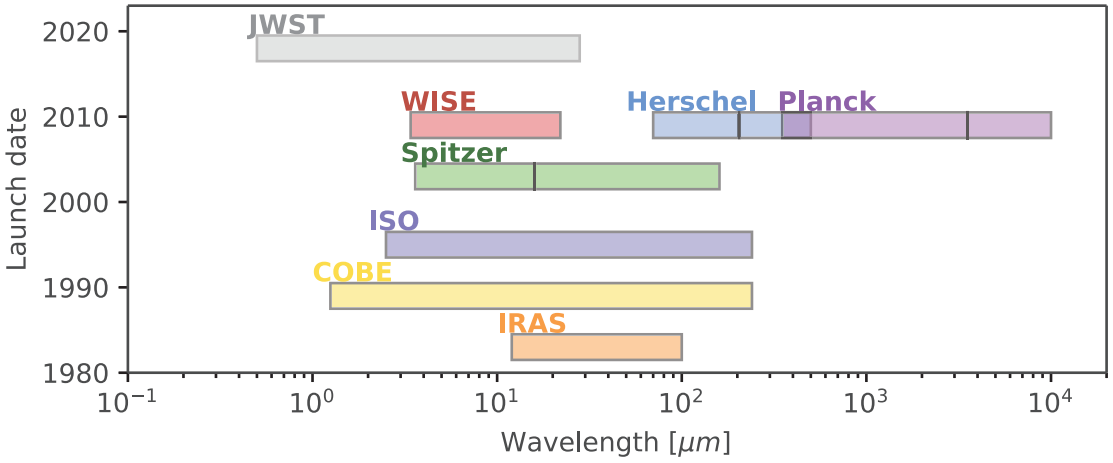

Figure 2.9: A non-exhaustive history of IR-/Submm-dedicated space telescopes

Magellanic Clouds.

The Planck satellite was launched in 2009 and finished its mission in 2013. It was built to study the CMB at much better resolution than COBE and following that, WMAP. Planck's two instruments, HFI and LFI (High/Low Frequency Instrument) observed the sky at 30, 44, 70, 100, 143, 217, 353, 545, and 857 GHz (i.e. 350, 550, 850 μm, and 1.4, 2.1, 3.0, 4.3, 6.8, and 10 mm). An extensive number of references could be given for the work that Planck has generated. Given its very large spectral coverage, it allowed for numerous studies. Its main purpose was to derive a new map of the CMB, and its spectral power distribution (which it did). It showed that the current Λ-CDM model is in very good agreement with the observations of deep space. In our case, an important result would be the modeling of dust emission at long wavelength by the Planck collaboration. They used a Modified Blackbody to fit their all-sky observations and found that we could match them with an emissivity $\beta = 1.51$ (Planck Collaboration et al. 2014).

The James Webb Space Telescope (JWST) is to be launched in 2018. It is the next very large space telescope and is designed for measurements in the NIR and the MIR. Its resolution will be better than *Spitzer* or *Hubble*, for which it is considered a successor. Four instruments will allow for photometry and spectroscopy: NIRCam, NIRSpec, MIRI and FGS-NIRISS. NIRCam and NIRSpec will be operating from 0.6 to 5 μm while MIRI will focus on wavelengths between 5 and 28 μm. The JWST represents a tremendous opportunity for IR astronomy, and a vast variety of science projects are already being assembled in the expectation of its incredibly fine measurements.

Figure 2.9 gives a summary of the spacecrafts, as well as other telescopes that worked in the IR and submillimeter.

PART I – TAKE AWAY

This Part has introduced us to the characteristics of interstellar dust. Here are a few key points to remember for the purpose of this thesis:

- a galaxy is filled with numerous and diverse components: old and young stars, hot and cold gas, diffuse and dense clouds of dust... which are all studied through light;
- the multiple objects in a galaxy contribute to the energy budget, and create available photons travelling through space and defining the Interstellar Radiation Field;
- dust can be observed through a few processes:
  - dust absorbs and scatters the UV and visible light, through a global process that we define as the extinction; its properties can be summarized in an extinction curve; this extinction curve has typical features like the 217 nm bump or the DIBS, whose variations and origins are uncertain;
  - dust re-emits this energy in the IR through the process of emission; the emission spectrum depends on the grain characteristics: large grains are in thermal equilibrium and their emission is similar to a modified blackbody, while small grains are stochastically heated and their emission shows features in the MIR and PAH features;
  - dust composition can be estimated through spectroscopy measurements in the gas phase; polarization is also a dust characteristic that can be observed;
- dust models adjusting all these observables are created to match our observations and derive dust properties in nearby and distant galaxies.

We will use these models to fit the IR emission in nearby galaxies in an application described in the Part II.

Part II

Modeling dust emission in the Magellanic Clouds

3

Fitting the IR emission in nearby galaxies

3.1 Context of this study

Dust plays a fundamental role in the evolution of a galaxy. It has a large impact on the thermodynamics and chemistry processes by catalyzing molecular gas formation (e.g. H_2 formation sites). It can be a gas tracer when the gas-to-dust ratio is known. It reflects the chemical history of a galaxy... To comprehend the dust impact on other processes and features in the ISM, it is of crucial importance to understand its physical state and composition, including minimal and maximal grain sizes, as described by dust models presented in Section 2.6.

All these models vary from one to another by the definition of dust composition, size distribution of grains, and laboratory-based data for optical properties, and are not necessarily constrained by the same observational references. As described in Chapter 2.7, the widely accepted description of dust involves two main chemical entities: carbonaceous grains, which usually show both amorphous and aromatic structures, and silicate grains, with metallic-element inclusions to agree with the observed abundances.

Section 2.7 presented the progress made in IR observations, from IRAS to *Herschel* and future JWST. In the ultraviolet, continued observations and analysis of extinction (Cardelli et al. 1988, 1989; Mathis 1990; Fitzpatrick & Massa 2005; Cartledge et al. 2005; Gordon et al. 2003, 2009) and depletions (Jenkins 2009; Tchernyshyov et al. 2015) have shown that large variations in dust properties exist from one line of sight to the next, and between galaxies.

Although we may have identified common behaviour with different models, the same models do not agree on all deduced properties (e.g., dust masses). It is difficult to determine whether the differences between dust studies arise from the intrinsic descriptions of the dust models, or the statistical treatment of the fitting algorithm, or both. In this study published as a paper (Chastenet et al. 2017), we use current dust grain models to fit the MIR to sub-millimeter observations of two nearby galaxies. Our goal is to quantitatively measure the discrepancies between the models used in a common fitting scheme, and assess which part of the SEDs can be reproduced best with a given set of physical inputs. To do so, we base our effort on the work of Gordon et al. (2014). In their study, they focused on fitting three models to the *Herschel* HERITAGE PACS and SPIRE photometric data: the Simple Modified BlackBody, the Broken Emissivity Modified BlackBody and the Two Temperatures Modified BlackBody (SMBB, BEMBB and

TTMBB, respectively). They identified a substantial sub-millimeter excess at 500 μm, in two nearby galaxies, presented below, likely explained by a change in the emissivity slope. They built grids of spectra, varying parameters for a given model (e.g., for the SMBB model, they allow the dust surface density, the spectral index, and the dust temperature to vary). They adopted a Bayesian approach to derive, for each spectrum, the multi-dimensional likelihood assuming a multi-variate Normal/Gaussian distribution for the data to assess the probability that a set of parameters fit the data. Their residuals and derived gas-to-dust ratio favor the BEMBB model, which best accounts for the sub-millimeter excess. We use the same statistical approach in this study. We present the two galaxies studied here, the Magellanic Clouds, before explaining the data in Section 4.3. Because we extend the observational constraints to shorter wavelengths, we must account for smaller dust grains and "full" models, and we make use of the DustEM tool [1] (Compiègne et al. 2011) to build our own grid of physical dust models (Section 5). We then compare the different models used based on residual characteristics (Section 6) and derive physical properties and interpretations (Sections 7 and 8).

3.2 Studying nearby galaxies

The closest galaxy to study is, of course, the one we live in. However, despite obvious high resolution, observing a galaxy from within comes with numerous drawbacks. For instance, the confusion along the line of sight, for any object in the MW lower than a latitude of $\sim$ 30°, is extremely important. Observations in the galactic disk are very complicated because most of the objects are found in this disk, all mixed together. A similar confusion can be faced when observing external galaxies. Because of our position in the MW, observations of other galaxies may exhibit a foreground, a signal that is not part of the studied object. In the IR, this foreground is the emission of the Galactic cirrus, the atomic gas floating in the MW, and confusing observers. However blaming it all on our Galaxy would be a shame: a confusing background also makes observations difficult. It is the signal emitted by faint and distant galaxies, called the Cosmic Infrared Background. This mixture of signals coming from different parts in space, along a single line-of-sight, cannot be avoided, and only reduced.

Another kind of problematic mixture happens in observations of nearby galaxies. When the spatial resolution is too coarse, the signal contained in that single fraction is the sum of multiple objects in a single pixel. Studying nearby galaxies is a way to decrease the impact of that problem: the closer the galaxy, the finer the spatial resolution, and the lower the number of objects in a single pixel.

Studying these galaxies, however, holds for an argument of statistical sample. Being restricted to only our Galaxy does not allow for general theories. The high variety of properties in nearby galaxies is a tremendous advantage in constraining our models: different shapes, dynamics, or ages lead to different evolution scenarios, with various galaxy properties. In the case of the ISM, studying galaxies other than the MW gives us access to multiple types of environment in which the dust and gas evolve. Since they are correlated with the star formation and age of a galaxy, we do not expect to see the same properties when it comes to a galaxy different from the MW. Using this different stages helps us to understand the life-cycle of ISM components within the galaxy, and how it changes from one galaxy to the next.

It also allows different approaches to study a galaxy. One can either consider its smaller components: when the resolution is good enough, we can distinguish sub-parts of the galaxy such as bubbles, filaments, star formation regions... These parts have individual properties than

[1] http://www.ias.u-psud.fr/DUSTEM/

Figure 3.1: Artist view of the Milky Way (left), and pictures of the Andromeda (middle) and Triangulum (right) galaxies. *Credit: NASA - Lorenzo Comolli - Robert Gendler*

can be of interest as such. On the other hand, one can choose to treat the galaxy as a whole, with average properties. Going further, we might even link the detailed behavior of a galaxy with its global characteristic. In doing so, studying nearby galaxies can be of great help when distant galaxies cannot be resolved.

In general, "nearby galaxies" refers to galaxies within the Local Group. It covers a radius of ~ 1.5 Mpc around the MW, including about 54 galaxies. It includes three spiral galaxies, represented in Figure 3.1, the Milky Way, the Andromeda Galaxy (M31) and the Triangulum Galaxy (M33). Most of the other objects are irregular and dwarf galaxies, satellites of the Milky Way or Andromeda, including the Magellanic Clouds, two galaxies of particular interest in this thesis.

4

The Magellanic Clouds: close neighbors

4.1 Description of the Clouds

In the surroundings of the MW, two small galaxies dance around. They can be seen with the naked eye, from the South hemisphere: the Small and Large Magellanic Clouds (together, the MCs; see Figure 4.1); although seen since ancient times, their name is a reference to the navigator Ferdinand Magellan who mention them in his travel journal. The Small Magellanic Cloud (SMC) is at 62 kpc from us (Graczyk et al. 2014) while the Large Magellanic Cloud (LMC) stands closer, at about 50 kpc (Keller & Wood 2006; Walker 2012). They are among the closest galaxies to us, classified as *dwarf irregular galaxies*, and are objects of particular significance for many reasons developed below, when it comes to studying the ISM.

With such proximity to us, the level of details achieved with recent instruments (*Spitzer* or *Herschel*) is unprecedented. With the resolution of *Herschel*, we can resolve down to ~ 13 pc in the LMC and ~ 17 pc in the SMC. As a comparison, studies have shown that the typical ISM structure in the dense phase is of a few tens of parsecs (Roman-Duval et al. 2010). The MCs are therefore among the best nearby galaxies to study in terms of resolution. Because of their position (galactic latitude of $\sim 30{-}45°$; ascension and declination coordinates: 00 52 38.0 -72 48 01 and 05 23 34.6 -69 45 22 for the SMC and LMC, respectively) the MCs suffer from less foreground confusion than other galaxies at lower latitude. Close to the galactic pole, the zodiacal light contamination is also less substantial than in other observations.

With a lower metallicity than the MW, of respectively $1/2\ Z_\odot$ and $1/5\ Z_\odot$ for the LMC and SMC (Russell & Dopita 1992; Rolleston et al. 2002), the MCs are expected to show differences in behaviour than that we would expect in a galaxy similar in metallicity to the MW. With less metals available compared to the MW, the star formation history and composition of dust is bound to be different from what we observe in our Galaxy. In particular, in the scope of this work, the metallicity directly impacts the observed properties of the ISM. The elements available for dust formation depend on the generations of stars that made possible heavy element production, from the nucleosynthesis occurring in their dense cores.

Using H I gas measurements, we find evidence that the two galaxies are in interaction (Putman et al. 2003; Brüns et al. 2005). The observable track left by this interaction is called the *Magellanic Stream* (for an extensive review, see D'Onghia & Fox 2016). In the SMC, this

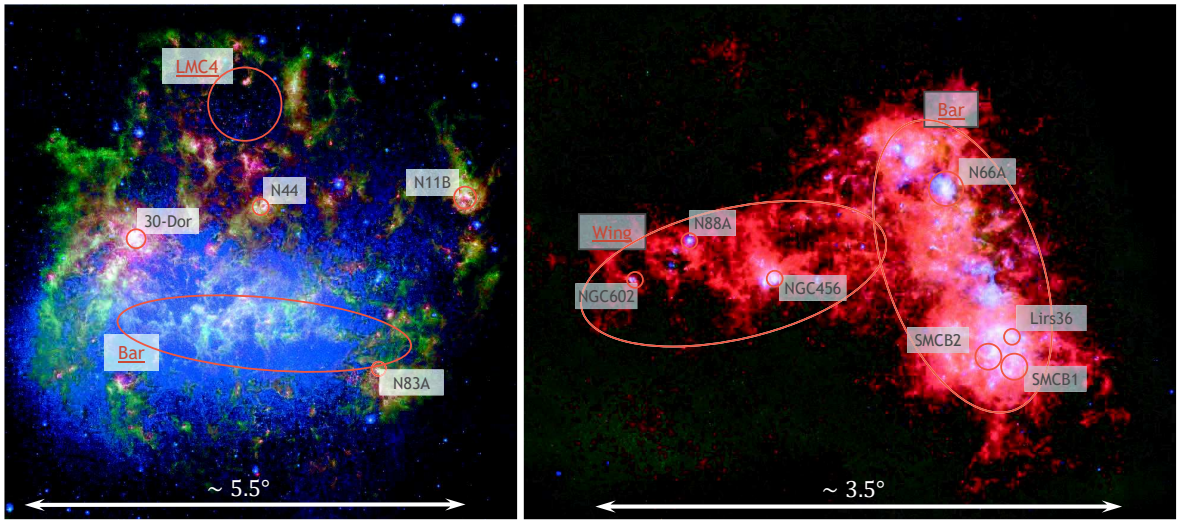

Figure 4.1: *Left:* The Large Magellanic Cloud. *Credit:* NASA, JPL-Caltech, M. Meixner and SAGE team. *Right:* The Small Magellanic Cloud. *Credit:* ESA, NASA, JPL-Caltech, STScI. The red regions indicate a few interesting spots in the galaxies, often studied and/or particularly bright.

	LMC	SMC
Stellar mass	$3.9\ 10^9\ M_\odot$	$3.0\ 10^8\ M_\odot$
HI mass	$4.4\ 10^8\ M_\odot$	$4.0\ 10^8\ M_\odot$
Total mass	$1.7\ 10^{10}\ M_\odot$	$2.4\ 10^9\ M_\odot$

Table 4.1: A few mass indicators in the LMC and SMC. The dust mass is omitted on purpose (Stanimirović et al. 2004; Brüns et al. 2005; Harris 2007; van der Marel & Kallivayalil 2014).

stream causes the gas and the stars to behave dynamically different, unlike that usually seen in other, more quiescent galaxies.

In Table 4.1 we gather a few indicators of masses in the galaxies. Despite an order of magnitude of difference in their total dust masses, the SMC atomic gas mass is quite close to that of the LMC. The extent of the H I distribution around the SMC is characteristic of this galaxy: although many galaxies shows a broad distribution, this is more visible in the SMC.

4.2 Interest of the MCs

Observations show that the infrared SEDs of the MCs differ from those seen in the Milky Way (MW). At (sub-)millimeter and centimeter wavelengths, dust is well modeled by a blackbody spectrum modified by a power-law (see Section 2.6). Many investigations have identified this trend by pointing out "excess" emission in the far-infrared (FIR) to radio wavelengths (e.g., Galliano et al. 2003, 2005; Bot et al. 2010; Israel et al. 2010; Gordon et al. 2010; Galliano et al. 2011; Gordon et al. 2014). In those models, it means that the spectral emissivity index β is lower in the MCs than in the MW. This excess had also been reported in the MW, although more mildly by Reach et al. (1995), who suggested this excess in the MW comes from cold dust. They rejected this hypothesis as the dust mass needed to account for such an emission (with dust at very low temperature) would be too high to be realistic, and violate elemental abundances. The current theory points toward different a power-law (i.e., different spectral indices) in the expression of the emissivity, in different wavelength ranges (e.g., a 'broken-

emissivity' modified blackbody model). Another kind of excess has been identified at 70 μm, with respect to the expected emission from MW-based dust models. The studies of Bot et al. (2004) and Bernard et al. (2008) linked this excess to a different size distribution and abundance of the very small grains whose emission is dominant at these wavelengths. The infrared peak (100 μm $\leqslant \lambda \leqslant$ 250 μm) also varies between the MW and the MCs and tends to be localized at shorter wavelengths in the SMC. This tendency may be due to the more intense radiation fields in the SMC.

Besides being close and offering good resolution, the MCs therefore seem to be good candidates to test the limits of our dust models.

4.3 Data used in this study

In this study, I fit the dust emission of the MCs. The MIR, FIR, and sub-millimeter images used in this study are taken from the *Spitzer* SAGE-SMC (Surveying the Agents of Galaxy Evolution; Gordon et al. 2011) and SAGE-LMC (Meixner et al. 2006) Legacies and the *Herschel* HERITAGE Key Project (The Herschel Inventory of the Agents of Galaxy Evolution; Meixner et al. 2013, 2015). The SAGE observations were taken with *Spitzer Space Telescope* (Werner et al. 2004) photometry instruments: the Infrared Array Camera (IRAC; Fazio et al. 2004) provided images at 3.6, 4.5, 5.8 and 8.0 μm and the Multiband Imaging Photometer for *Spitzer* (MIPS; Rieke et al. 2004) providing images at 24, 70, and 160 μm. The observations cover a ~ 30 $^{\circ 2}$ region for the SMC and ~ 50 $^{\circ 2}$ for the LMC. Data in the FIR to sub-millimeter were taken with PACS (Photoconductor Array Camera and Spectrometer; Poglitsch et al. 2010) and SPIRE (Spectral and Photometric Imaging Receiver; Griffin et al. 2010) on board the *Herschel Space Observatory* (Pilbratt et al. 2010), providing images at 100, 160, 250, 350, and 500 μm. The observations cover the same regions as the *Spitzer* data.

I used the combined *Spitzer* and *Herschel* sets of bands to cover the IR spectrum. The combined bands are from IRAC 3.6, 4.5, 5.8, and 8.0 μm, MIPS 24 and 70 μm, PACS 100 and 160 μm, and SPIRE 250, 350 and 500 μm. Thanks to the custom de-striping techniques used to process the HERITAGE data (see Meixner et al. 2013, for details), the PACS 100 data combines the resolution of Herschel with the sensitivity of IRAS 100. Similarly, the PACS 160 image was merged with the MIPS 160 image.

Like Gordon et al. (2014), first, all the images were convolved using the Aniano et al. (2011) kernels to decrease the spatial resolution of all images to the resolution of the SPIRE 500 μm band of $\sim 36''$. Next, the foreground dust Milky Way dust emission was subtracted. To do so, we built a MW dust foreground map using the MW velocity H I gas maps from Stanimirovic et al. (2000) for the SMC and Staveley-Smith et al. (2003) for the LMC. To convert the velocity gas maps to a dust emission map, I used the Compiègne et al. (2011) model. I derived conversion coefficients from H I column to MW dust emission, and subtracted the resulting maps from the data.

After this processing, the PACS observations show a gradient across the images. I removed this gradient by subtracting a two-dimensional surface, estimated from background regions in the images. Regions outside the galaxies (and bright sources) were chosen to evaluate a "background" plane that was then subtracted from all the images. For the LMC, the observations did not extend beyond the full disk and this introduced a larger uncertainty in the final background subtracted images. The SMC observations extend beyond the galaxy and we have access to regions on the images fully outside the galaxy. Finally, I rebinned the images to have a pixel scale of $\sim 56''$ that is larger than the resolution of the SPIRE 500 μm band to provide nominally

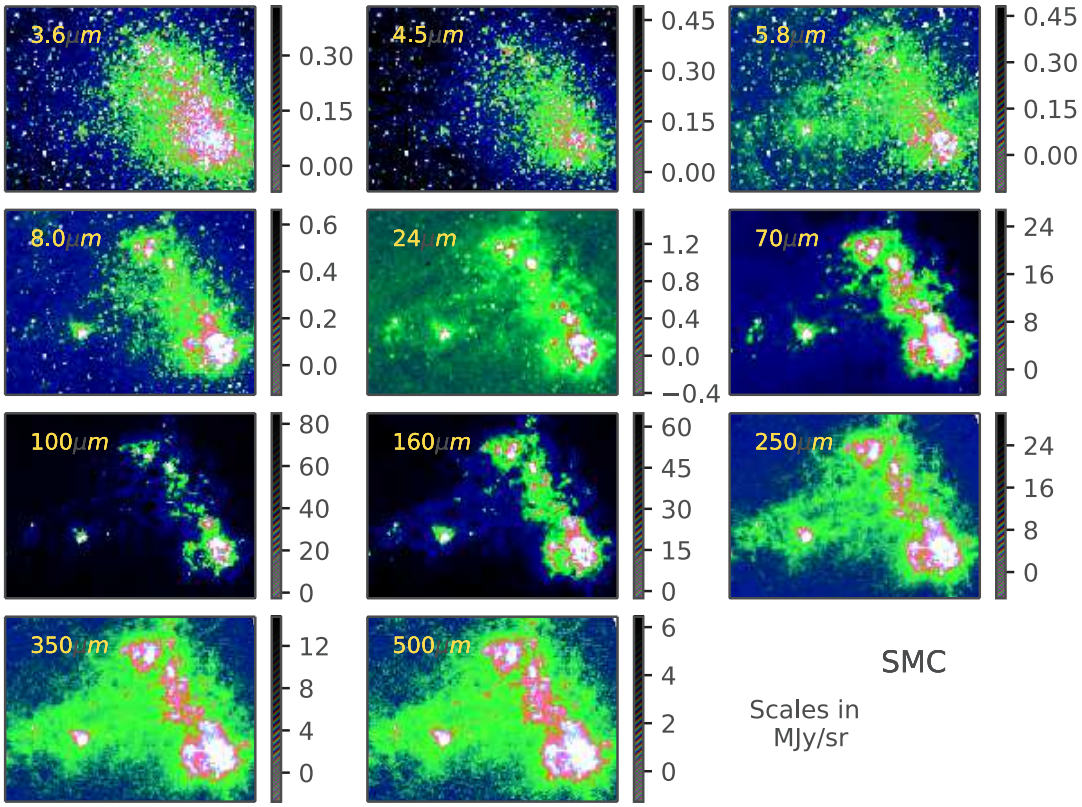

Figure 4.2: The Small Magellanic Cloud seen with *Spitzer* at 3.6, 4.5, 5.8, 8.0, 24 and 70 μm and *Herschel* at 100, 160, 250, 350 and 500 μm.

independent measurements for later fitting. Figures 4.2 and 4.3 shows the final data used in the 11 bands.

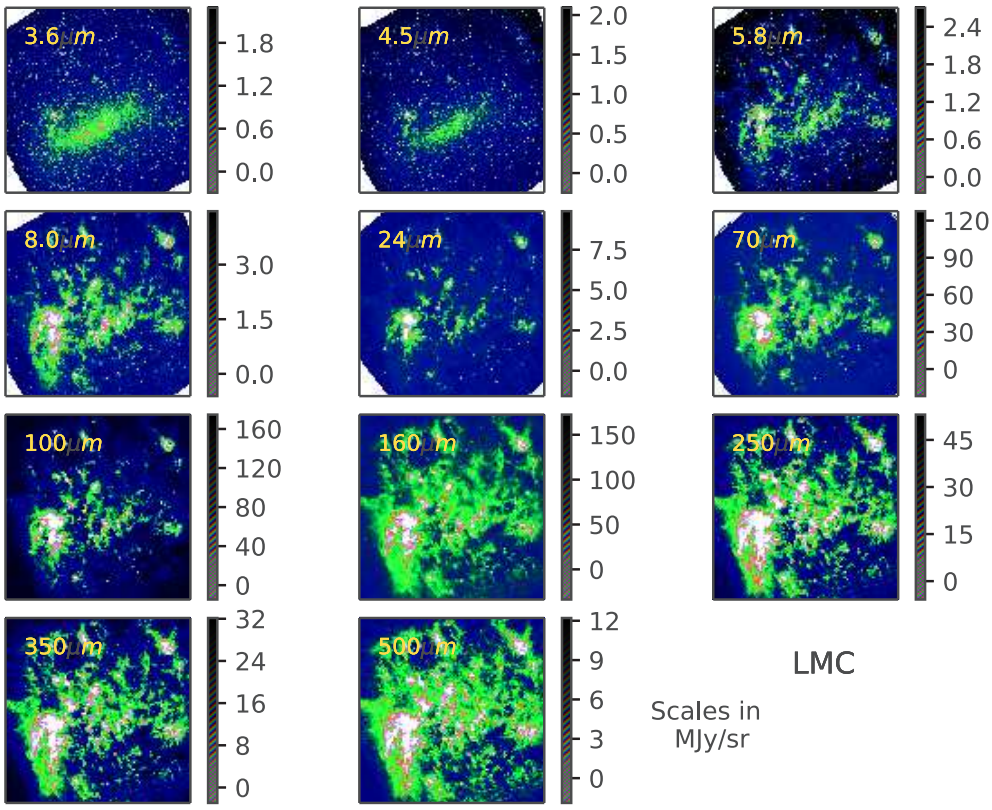

Figure 4.3: The Large Magellanic Cloud seen with *Spitzer* at 3.6, 4.5, 5.8, 8.0, 24 and 70 μm and *Herschel* at 100, 160, 250, 350 and 500 μm.

5 Tools and computation

To create the model SEDs, I used DustEM. To find the best fit in each pixel, or compare models to observations, I used the SED fitting tool: DustBFF. We will overview here in more details both tools and the work done.

5.1 DustEM

The DustEM tool (Compiègne et al. 2011) outputs emission and extinction curves calculated from dust grains properties. For each grain type, properties like the scattering and absorption efficiencies $Q_{\rm ext}(\lambda,a)$ and $Q_{\rm sca}(\lambda,a)$, and the heat capacities $C(\lambda,a)$ are used. Each model available explicitly specifies the minimal and maximal grain size $a_{\rm min}$, $a_{\rm max}$ and the size distribution law to adopt for each grain component. Finally, astronomical data like the full ISRF spectrum is used as well. I use the DustEM IDL wrapper[1] to generate full model grids with a large number of emission spectra. The wrapper forward-models the observations by multiplying the model SED with transmission curves. I used two dust models in this study (see 2.6 for more details) based on the work from Compiègne et al. (2011) and Jones et al. (2013) updated by Köhler et al. (2014) and Ysard et al. (2015). Here, we remind briefly the reader what the components of these models are.

The model from Compiègne et al. (2011) (MC11) is a mixture of PAHs, both neutral and ionized (cations), small and large amorphous carbonaceous grains (SamC and LamC, respectively; Zubko et al. 1996) with different size distributions, and amorphous silicate grains (aSil; Draine & Lee 1984), that is, a total of five independent components. In my fitting, I chose to use only a single PAH population, by summing the ionized and neutral species together. Given the shape of the emission spectra from the charged and neutral PAHs, the broad-band observations could not constrain them independently. I also tied (by summing) the big grains (BGs) together, originally described by both large carbonaceous and amorphous silicates. At $\lambda \geqslant 250$ μm, the emissivity law of both carbon and silicate grains in this model is the same ($\beta \sim 1.7-1.8$). Hence, they cannot be discriminated from their emission alone and allowing them to vary would result in the fitting arbitrarily choosing one or the other type of grains. Their variations with the

[1] available at http://dustemwrap.irap.omp.eu/

temperature are not different enough to be helpful in breaking the degeneracy. More precisely, I use three independent grain populations for this model.

The second model I used is the one for the diffuse-ISM-type dust in the Heterogeneous Evolution Dust Model at the IAS (THEMIS; Jones et al. 2013; Köhler et al. 2014). In this model, the dust is described by two components, split into four populations: very small grains made of aromatic-rich amorphous carbon, large(r) carbonaceous grains with an aliphatic-rich core and an aromatic-rich mantle, and amorphous silicate grains with nano-inclusion of Fe/FeS and aromatic-rich amorphous carbon mantle. The silicate grains are split into two populations: pyroxene ($-(SiO_3)_2$) and olivine ($-(SiO_4)$). I choose to tie these two silicate populations for the same reason as previously mentioned: up to 500 μm, they cannot be discriminated by their emission only. I therefore use three independent grain populations for THEMIS.

There is no clear correspondence between the two models because of their different (yet sometimes overlapping) grain-type definitions. The PAHs are only a feature of the MC11 model, the SamC refers to the small-amorphous carbon grains, and BGs refer to the large-amorphous carbon grains and amorphous silicates. In THEMIS, sCM20 and lCM20 refers to the small- and large- amorphous carbon grains, respectively, and we refer to the pyroxene (aPyM5) and olivine (aOlM5) grains altogether as aSilM5. Figure 5.1 shows the models as they were used with their respective grain populations.

The free parameters we allow to vary in the fitting are $Y_{\rm PAHs}$, $Y_{\rm SamC}$, and $Y_{\rm BGs}$ in the MC11 model, and $Y_{\rm sCM20}$, $Y_{\rm lCM20}$, and $Y_{\rm aSilM5}$ in THEMIS. The $Y_{\rm i}$ are scaling factors of the solar neighborhood abundances $M_{\rm i}/M_{\rm H}$, where i is one of the grain species (e.g., Compiègne et al. 2011). The SEDs are scaled through these parameters. Additionally, the ISRF environment will change with different approaches. This is explained in Section 6. Finally, due to short wavelengths and a non-negligible emission from stars in the IRAC bands, I also add a stellar component modeled as a black-body spectrum at 5 000 K. This parameter is scaled through a stellar density Ω^*.

5.2 DustBFF

The fitting technique used in this thesis follows the work of Gordon et al. (2014). They introduced a method that propagates uncertainties throughout of fit thanks to covariance matrices. This allows the uncertainties between the different bands to be taken into account, in the data. Although new techniques to consider correlated noise exist, this one avoids substantial simulations to estimate the global noise, and instead adds noise to each fit (for each pixel). Gordon et al. (2014) make use of a multi-variate distribution to determine the probability that a given model will fit the data:

$$P(\boldsymbol{S}^{\rm obs}|\theta) = \frac{1}{Q}\, {\rm e}^{-\frac{1}{2}\,\chi^2(\theta)} \tag{5.1}$$

$$Q = (2\pi)^n\, {\rm det}|\mathbb{C}| \tag{5.2}$$

with n being the number of bands, and $\mathbb{C}$ the covariance matrix. In this distribution, the χ^2 value is computed from the difference between the model prediction and the data, on which we apply uncertainties through $\mathbb{C}$:

$$\chi^2(\theta) = (\boldsymbol{S}^{\rm obs} - \boldsymbol{S}^{\rm mod}(\theta))^T\, \mathbb{C}^{-1}\, (\boldsymbol{S}^{\rm obs} - \boldsymbol{S}^{\rm mod}(\theta)) \tag{5.3}$$

$\boldsymbol{S}^{\rm obs}$ and $\boldsymbol{S}^{\rm mod}(\theta)$ are respectively the observed SED, and the modeled SED for a parameter set, θ. The correlation matrix $\mathbb{C} = \mathbb{C}_{\rm bkg} + \mathbb{C}_{\rm cal}$ is the combination of two kinds of uncertainties. The

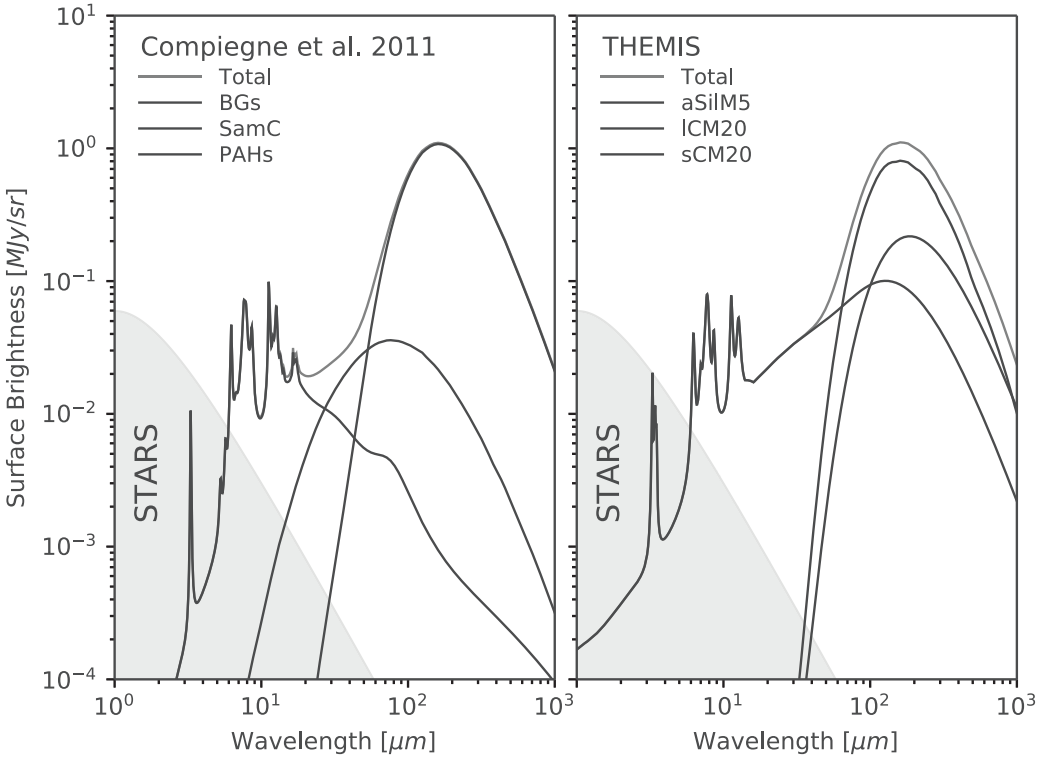

Figure 5.1: Compiègne et al. (2011) (MC11 model, *left*) and THEMIS (*right*) emission spectra, for U=1 (from Mathis et al. (1983)) and $N_{\mathrm{H}} = 10^{20}$ H cm^{-2}. The difference between these two models are the total number of components and optical and heating properties. The stellar component is a scaled blackbody at 5 000 K.

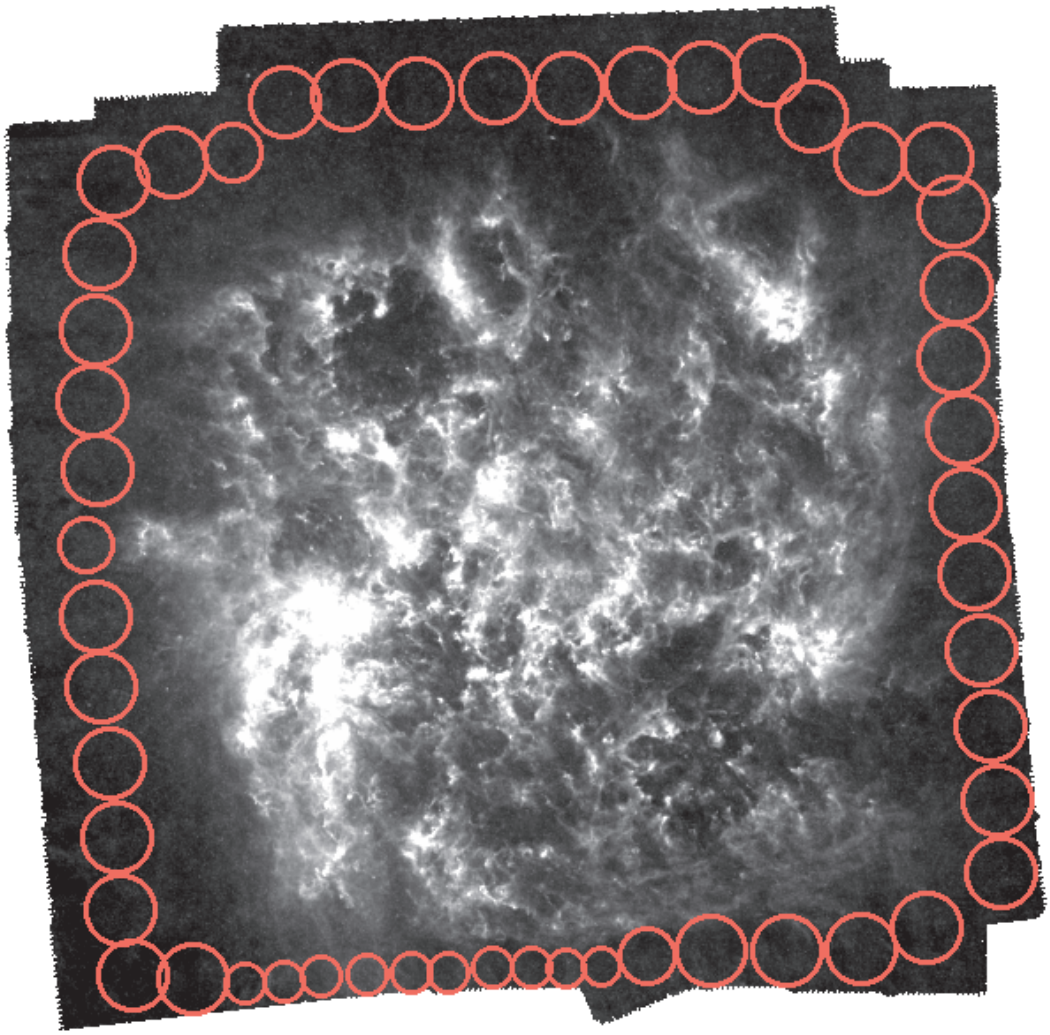

Figure 5.2: SPIRE500 image of the LMC showing the regions defined to determine the background correlation matrix $\mathbb{C}_{\rm bkg}$, marked by red circles.

correlation of the background from band to band is an empirical measure made over each band, and each element of the matrix is defined as:

$$(\mathbb{C}_{\rm bkg})^2_{ij} = \frac{\Sigma_k^N (S_i^k - \langle S_i \rangle)(S_j^k - \langle S_j \rangle)}{N-1}. \tag{5.4}$$

with S_x^k, the value of the $k^{\rm th}$ in the $x^{\rm th}$ band, and $\langle S_x \rangle$, the average background value of the $x^{\rm th}$ band. In order to avoid contamination from the actual signal one tries to model, $\mathbb{C}_{\rm bkg}$ is calculated from regions outside of the galaxy. Figure 5.2 shows a example of regions (circles) chosen in the LMC. The higher the number of pixels, N, counted as part of the background, the better will be $\mathbb{C}_{\rm bkg}$ estimation.

The errors made on the observations themselves are part of the $\mathbb{C}_{\rm cal}$ matrix. It is calculated as:

$$(\mathbb{C}_{\rm cal})_{i,j} = S_i^{\rm mod}(\theta))\ S_i^{\rm mod}(\theta))\ (\mathcal{M}_{\rm uncorr} + \mathcal{M}_{\rm corr}) \tag{5.5}$$

The matrices $\mathcal{M}_{\rm uncorr}$ and $\mathcal{M}_{\rm corr}$ are determined from the detailed calibration work done for each instrument. For 'uncorrelated' errors, we usually refer to the characteristic of repeatability of measurements. This term describes how stable a measurement is in instrument units at high

signal-to-noise. This error is not correlated between the different bands of the same instrument, and depicts the diagonal elements of the M_{uncorr} matrix. The measured gain of an instrument is a 'correlated' error. For example, estimating the sky level outside of the bright star measured (used for calibration) relies on various possible methods (e.g., increasing apertures). The systematic errors made in any of the methods propagate throughout the instrument, introducing correlated uncertainties. I account for calibration uncertainties as correlated errors. The IRAC and MIPS instruments were calibrated with stars. The IRAC uncertainties were taken from Reach et al. (2005). The instrument has a stability accounting for uncorrelated error of 1.5%; the absolute calibration leads to uncertainties of 1.8%, 1.9%, 2.0%, and 2.1% at 3.6, 4.5, 5.8, and 8.0 μm, respectively. The MIPS uncertainties were taken from Engelbracht et al. (2007) and Gordon et al. (2007). The repeatability at 24 and 70 μm is 0.4% and 4.5%, respectively. Absolute calibrations were made from star observations and give 2% and 5% error, at 24 and 70 μm, respectively. The PACS calibration was done with stars and asteroid models, with an absolute uncertainty of 5%, correlated between PACS bands, and a repeatability of 2% (Müller et al. 2011; Balog et al. 2013).

The SPIRE calibration used models of Neptune with an absolute uncertainty of 4% and 1.5% repeatability uncorrelated between bands (Bendo et al. 2013; Griffin et al. 2013). Both of the absolute uncertainties quoted above (5% and 4%) were made upon point source calibration. I chose to double all the uncorrelated uncertainties to account for the error on the beam area that arises for extended sources (see the matrices 5.11 - 5.14.)

$$\mathcal{M}_{\rm uncorr}^{\rm IRAC} = \begin{pmatrix} 0.015^2 & 0 & 0 & 0 \\ 0 & 0.015^2 & 0 & 0 \\ 0 & 0 & 0.015^2 & 0 \\ 0 & 0 & 0 & 0.015^2 \end{pmatrix}, \tag{5.6}$$

$$\mathcal{M}_{\rm uncorr}^{\rm MIPS} = \begin{pmatrix} 0.004^2 & 0 \\ 0 & 0.045^2 \end{pmatrix}, \tag{5.7}$$

$$\mathcal{M}_{\rm uncorr}^{\rm PACS} = \begin{pmatrix} 0.02^2 & 0 \\ 0 & 0.02^2 \end{pmatrix}, \tag{5.8}$$

$$\mathcal{M}_{\rm uncorr}^{\rm SPIRE} = \begin{pmatrix} 0.015^2 & 0 & 0 \\ 0 & 0.015^2 & 0 \\ 0 & 0 & 0.015^2 \end{pmatrix} \quad \text{and} \tag{5.9}$$

$$\mathcal{M}_{\rm uncorr} = \begin{pmatrix} \mathcal{M}_{\rm uncorr}^{\rm IRAC} & & & (0) \\ & \mathcal{M}_{\rm uncorr}^{\rm MIPS} & & \\ & & \mathcal{M}_{\rm uncorr}^{\rm PACS} & \\ (0) & & & \mathcal{M}_{\rm uncorr}^{\rm SPIRE} \end{pmatrix}. \tag{5.10}$$

$$\mathcal{M}_{\rm corr}^{\rm IRAC} = \begin{pmatrix} 0.036^2 & 0.036^2 & 0.036^2 & 0.036^2 \\ 0.036^2 & 0.038^2 & 0.036^2 & 0.036^2 \\ 0.036^2 & 0.036^2 & 0.040^2 & 0.036^2 \\ 0.036^2 & 0.036^2 & 0.036^2 & 0.042^2 \end{pmatrix}, \tag{5.11}$$

$$\mathcal{M}_{\rm corr}^{\rm MIPS} = \begin{pmatrix} 0.04^2 & 0.04^2 \\ 0.04^2 & 0.1^2 \end{pmatrix}, \tag{5.12}$$

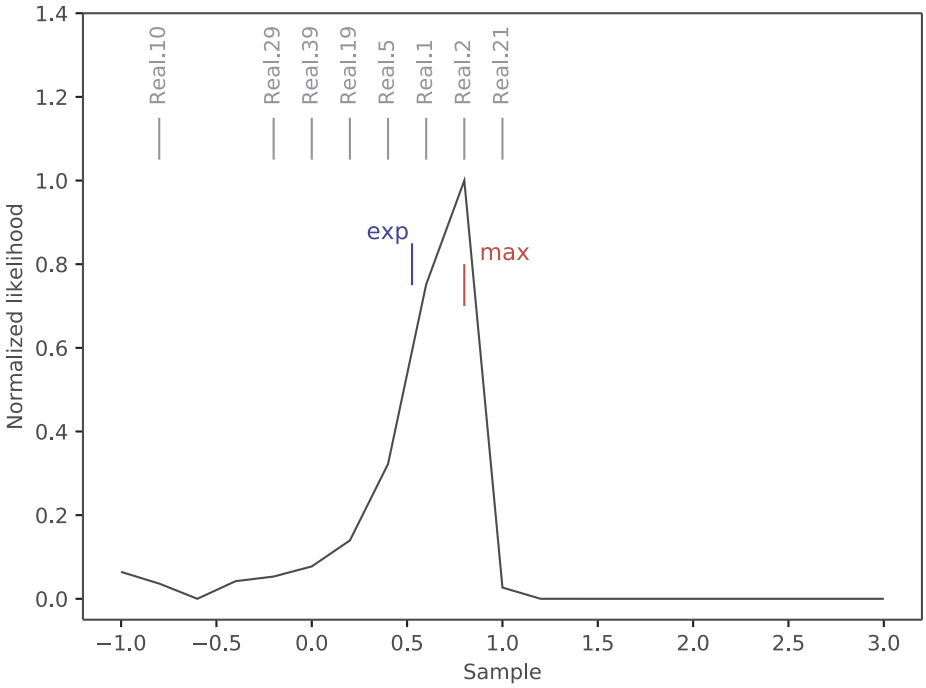

Figure 5.3: Representation of the DustBFF outputs: the 'max' corresponds to the maximum likelihood, 'exp' to the weighted average likelihood. A few realizations are shown as well.

$$\mathcal{M}_{\rm corr}^{\rm PACS} = \begin{pmatrix} 0.1^2 & 0.1^2 \\ 0.1^2 & 0.1^2 \end{pmatrix}, \tag{5.13}$$

$$\mathcal{M}_{\rm corr}^{\rm SPIRE} = \begin{pmatrix} 0.08^2 & 0.08^2 & 0.08^2 \\ 0.08^2 & 0.08^2 & 0.08^2 \\ 0.08^2 & 0.08^2 & 0.08^2 \end{pmatrix} \quad \text{and} \tag{5.14}$$

$$\mathcal{M}_{\rm corr} = \begin{pmatrix} \mathcal{M}_{\rm corr}^{\rm IRAC} & & & (0) \\ & \mathcal{M}_{\rm corr}^{\rm MIPS} & & \\ & & \mathcal{M}_{\rm corr}^{\rm PACS} & \\ (0) & & & \mathcal{M}_{\rm corr}^{\rm SPIRE} \end{pmatrix}. \tag{5.15}$$

The DustBFF tool outputs the n-D likelihood function of the fits, and marginalizes it on each parameter space to create 1D likelihoods. Several estimates can then be used. The 'max' value is defined as the maximum likelihood, or sometimes traditionally referred to as the χ^2; it reflects the closest model to the observations, and in this study I use it for residual calculations (see Section 6). The expectation ('exp') value translates more the whole likelihood in the sense that it is a weighted average. It has the advantage of giving a more global picture of the likelihood function. A very useful approach is to randomly extract multiple values of a likelihood function. This 'realization' method reflects the shape of the function and the fitting noise. This will be used to study parameter behavior, and namely derive dust masses. These outputs are represented on a schematic view in Figure 5.3.

5.3 Model (re-)calibration

Since I want to investigate the differences between two dust-grain models independently of the fitting algorithm, it is critical to make sure that they share the same calibration. Moreover, this calibration should be made using the same measurements with the same technique. Usually, dust grain models are calibrated to reproduce the diffuse MW dust emission (e.g., Boulanger et al. 1996) and extinction, with constraints on elemental abundances from depletion measurements (e.g., Jenkins 2009; Tchernyshyov et al. 2015). However, they often do not share the same calibration technique or the same constraint measurements.

MC11 and THEMIS size distributions are calibrated on the diffuse extinction in the MW. Measurements at high Galactic latitude from the Cosmic Background Explorer (COBE; Bennett et al. 1996), coupled with the Wilkinson Microwave Anisotropy Probe (WMAP; Jarosik et al. 2011) and Infrared Space Observatory (ISO; Mattila et al. 1996) trace the global SED of dust emission. It was correlated with H I measurements and is expressed in flux units per hydrogen atom. Hence, in both models, the dust grain 'masses' are given as dust-to-hydrogen ratios $M_{\rm dust}/M_{\rm H}$. The total dust mass in each model implies a hydrogen-to-dust ratio that varies from one model to the other. Although each model fits the MW dust emission at high latitude, given their different dust descriptions, they do not necessarily share the same gas-to-dust ratio. However, this should be a reference point in calibrating dust models as this can be measured with other methods. In the MW, I follow the value of Gordon et al. (2014) and set the diffuse MW hydrogen-to-dust ratio at 150 (derived from Jenkins 2009, for $F_* \sim 0.36$).

To ensure that both models produce the same result when fitted to the MW diffuse ISM, I "recalibrate" the models using the ISO, COBE, and WMAP measurements of the local ISM as described in Compiègne et al. (2011). I do not take into account the 0.77 correction for the ionized gas in order to be consistent with the depletion work of Jenkins (2009), which does not correct the ionized gas contribution. I integrated this spectrum in the *Spitzer* and *Herschel* photometric bands and obtained a SED whose values are shown in Table 5.1. The PACS and SPIRE values are very close to those displayed in Gordon et al. (2014) (Section 5.1 in their paper).

I used the DustBFF fitting technique to scale the full spectrum of each model to the SED described in Table 5.1 and found the factor that gave the adopted gas-to-dust ratio of 150. I did not allow the grain species to vary from one another, and I chose to keep the same ratios between populations as described by the model. I set the ISRF at $U = 1$, that is, the same used for the model definition. The fits thus consist of adjusting the global emissivity, and scaling the *total* emission spectrum. I built a different correlation matrix for the estimated flux uncertainties from the observing instruments quoted. Following Gordon et al. (2014), I assumed 5% correlated and 2.5% uncorrelated uncertainties at long wavelengths for the COBE, FIRAS, and DIRBE instruments (accounting for PACS and SPIRE bands). I presumed a 10% error for both correlated and uncorrelated uncertainties at short wavelengths given the resolution of ISO (accounting for IRAC and MIPS bands). I derived a scaling factor that is the result of the fit of the models. The final correction factors are 1.6 and 2.42 for the whole spectrum of THEMIS and the MC11 model, respectively. These factors aim at self-calibrating the models to give the same gas-to-dust ratio of 150 for the same MW SED. This step is crucial as the goal is to compare two models, independently of the fitting method, for which differences are eliminated by the use of a common fitting procedure. It should be noted that, if the first step aims at a rigorous fit to the MW SED, the second step's goal is to adjust the GDR and therefore moves away from a good fit.

I convert the emission output from DustEM $4\pi\nu I_\nu$, in erg s^{-1} cm^{-2} (H cm^{-2})$^{-1}$ to surface

Bands	Diffuse ISM	Bands	Diffuse ISM
IRAC3.6	0.00235	PACS100	0.714
IRAC4.5	0.00206	PACS160	1.55
IRAC5.8	0.0134	SPIRE250	1.08
IRAC8.0	0.0431	SPIRE350	0.561
MIPS24	0.0348	SPIRE500	0.239
MIPS70	0.286		

Table 5.1: The values of the local diffuse ISM integrated in the *Spitzer* and *Herschel* bands, used for calibration, in MJy sr^{-1} $\times 10^{20}$ H atom^{-1}.

brightness units, expressed in MJy sr^{-1}, with the scaling factors as follows:

$$S_\lambda = 4\pi\ \nu I_\nu \times 2.65\ 10^{21} \times \lambda \times \begin{cases} 1.6 \text{ if we use THEMIS} \\ 2.42 \text{ if we use MC11} \end{cases} . \tag{5.16}$$

6 Model comparison

I vary a number of dust model parameters that affect the SED shape and fit these new spectra to the data. In this study, I mainly examine dust emission when it is illuminated by different ISRF mixtures. At higher ISRFs, we expect the IR peak to shift to shorter wavelengths. I focus on this behaviour after considering the shape of global SEDs in the MCs. In all cases, I vary the $Y_{\rm i}$ parameters, which adjust each grain abundance. I also change the ISRF intensity, scaled by the free parameter U. In the whole study, I use the standard radiation field defined by Mathis et al. (1983). The $U = 1$ case corresponds to the solar neighborhood ISRF $\mathrm{U}_{\odot}$. In one case only, I vary the small grain size distribution. Throughout the fitting, I do not change the large grain size distributions, and therefore assume no change between the MW and the MCs, regarding this aspect.

I choose to fit each pixel that is detected at least 3σ above the background in eight bands (IRAC8.0, MIPS24 and MIPS70, PACS100 and PACS160 and all SPIRE bands): I do not impose the detection condition at 3.6, 4.5, and 5.8 μm as these bands can include a significant contribution from stars. I do include all the IRAC observational data in the fitting. In the following, the 'faint' or 'bright' aspect of a pixel is based on its emission at 500 μm.

To study the fits quality, I use fitting residuals. They illustrate how the models match the data and are expressed as the error $(\mathrm{data} - \mathit{model})/\mathrm{data}$.

Figure 6.1 shows fitting results for two pixels in the SMC, one with faint emission (left) and one with bright emission (right), for THEMIS only. This figure gives an idea of the different model variations that are described in the following sections.

6.1 Using a single ISRF

I first used the models with a single ISRF environment. This simply means that each spectrum is calculated from the emission of grains illuminated by a single ISRF, the strength of which varies. I do not change the shape or hardness of the ISRF. In Figure 6.2, I show the distribution of fractional residuals expressed as $(\mathrm{data} - \mathit{model})/\mathrm{data}$, in the SMC (top) and the LMC (bottom) for the two different models. The red bars shows the results for THEMIS and the purple bars, the MC11 model.

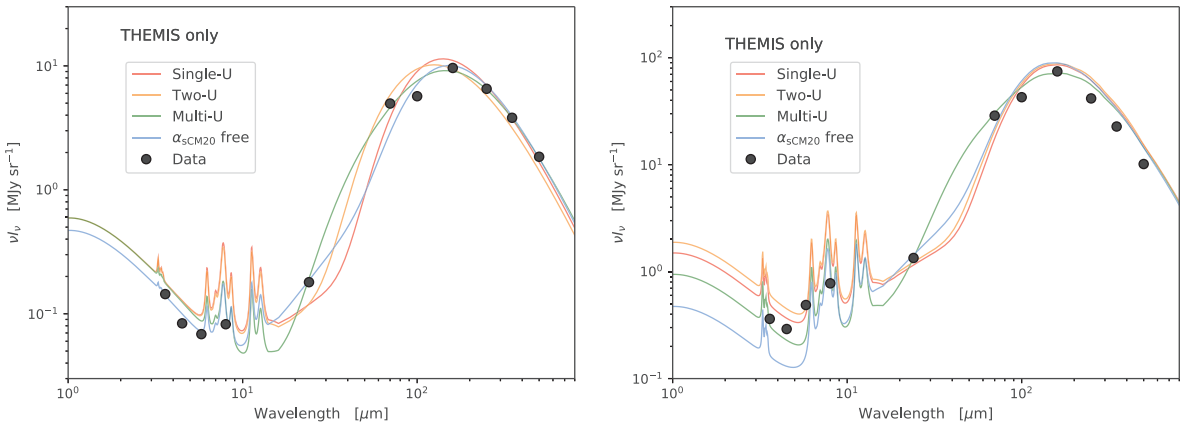

Figure 6.1: Examples of the fit results in the SMC for faint (left) and bright (right) pixels . We note that the FIR is best fit in faint (diffuse) environments. We also see the impact of a change in the 8/24 μm slope on the fits in the MIR.

First, the residuals do not have a Gaussian shape. In some bands (e.g., PACS160 in the upper image of Figure 6.2), the residuals have a large negative tail.

Second, the large grain population (aSil+LamC tied) in the MC11 model does not reproduce well the FIR emission at $\lambda \geqslant 100$ μm in the SMC, where the fractional residual distribution is broad. THEMIS, with a single ISRF, on the other hand, seems to reproduce the long-wavelength part of the SED in the SMC better than the MC11 model. We notice that the model is still, on average, slightly too high to properly reproduce the observations (noticeable by a mean of the residuals below 0) in the SMC and the LMC.

The FIR slope of the big grains in the MC11 model, described by a $\beta \sim 1.7 - 1.8$, is not compatible with the observed SEDs in the SMC, which show peculiarities: flat FIR emission and broad IR peak. The modeled slope is too steep to reproduce the flatter emission spectrum observed below 500 μm. Another explanation of the broad residuals may come from the ratio between silicate and carbonaceous material. This ratio is believed to be fairly constant across the Galaxy. Tying aSil+LamC as one component implies that this ratio, imposed by the original model, is kept throughout the fitting. Further tests showed that the initial assumption of tying these two populations is justified and does not prevent a better fit to the long-wavelength observations. In THEMIS, the large carbonaceous grain emission, in particular, exhibits a flatter FIR slope than the MC11 model (see Figure 5.1). This is likely why THEMIS reproduces the FIR SED better and is likely the reason for a better reconstruction of the observations.

The excesses visible at 70 and 100 μm with the MC11 model are better fit with the THEMIS model. At short wavelengths, and especially at 8 μm, the MC11 model shows smaller residuals than THEMIS. This is likely the consequence of an additional degree of freedom in that part of the spectrum. THEMIS uses a single population to depict the small grains emission, whereas MC11 uses two distinct grain species (PAHs and SamC, Figure 5.1).

A single ISRF intensity is arguably not a good reproduction of the physical environment of dust and the nature of the observations. Mixture of the starlight along the line of sight is likely to occur. A single ISRF remains nonetheless the simplest model and can be used to compare with simpler models, such as SMBB or BEMBB, as they also only assume a single ISRF heating. Figure 4 of Gordon et al. (2014) shows the residuals at 250 μm. On average, the BEMBB model (the one they retain as best in their study) gives better residuals than the fitting. In both cases, we notice a slight shift toward negative values, indicating the BEMBB model is too high with

respect to the observations. Yet, their results better match the data. This is likely due to the fact that the FIR slope can be directly adjusted using the β_2 parameter in each pixel independently.

6.2 Using multiple ISRFs

The next level of complexity for the heating environment is to use two ISRFs. In this case, I consider two components of dust: I calculate the emission of each grain population when irradiated by two ISRFs with different strengths, which leads to a "warm" dust and a "colder" one, and then mix the spectra with a fraction $f^{\rm warm}$:

$$I_\nu = \sum_X Y_{\rm X} \left(f^{\rm warm} I_\nu^{\rm X^{warm}} + (1 - f^{\rm warm}) I_\nu^{\rm X^{cold}} \right), \tag{6.1}$$

where X = {aSilM5; lCM20; sCM20} (THEMIS). The fraction parameter $Y_{\rm X}$ is identical for all grain populations. Effectively, we have two parameters $U^{\rm warm}$ and $U^{\rm cold}$, that both scale up and down the ISRF. It physically means that I model two dust masses $M_{\rm dust}^{\rm warm}$ and $M_{\rm dust}^{\rm cold}$, instead of a single effective dust mass as in Section 6.1. The $I_\nu^{\rm X^{warm}}$ and $I_\nu^{\rm X^{cold}}$ refer to the dust SEDs heated by $U^{\rm warm}$ and $U^{\rm cold}$, respectively, with $U^{\rm cold} < U^{\rm warm}$. Meisner & Finkbeiner (2015) used a similar approach to fit the Planck HFI all-sky maps combined with IRAS 100 μm. They showed that this provides better fits in the wavelength range (100 - 3 000 μm) than a simple modified blackbody.

Finally, one can use a more complicated combination of ISRFs. Thus, I also follow the work of Dale et al. (2001) in which the final SED is a power-law combination of SEDs at various ISRFs, integrated over a range of strengths:

$$dM_{\rm d}(U) \propto U^{-\alpha_{\rm ISRF}} dU, \qquad 10^{-1} {\rm U}_\odot \leq U \leq 10^{3.5} {\rm U}_\odot \tag{6.2}$$

The $\alpha_{\rm ISRF}$ coefficient is the parameter that regulates the weight of strong/weak ISRFs in the mixture used to irradiate the dust in a multi-ISRF model. A low $\alpha_{\rm ISRF}$ gives more weight to the high ISRFs. I allow the $\alpha_{\rm ISRF}$ parameter to vary between 1 and 3, as suggested by previous studies (e.g. Bernard et al. 2008).

Figure 6.1 gives a representation of the differences on the dust emission brought by changing the ISRF. The results are shown for THEMIS, in a faint (left) and bright (right) pixels (based on SPIRE500 emission). In Figure 6.1, we note that the use of multiple ISRFs leads to a better match of the 24 μm data. In the faint pixel, the emission in the IRAC bands is dominated by starlight and not extremely sensitive to small carbon grains, except at 8.0 μm. The differences in the fits in a faint or bright pixel could mean that diffuse regions are better reproduced by THEMIS than brighter regions, which are most likely denser. In these regions, dust may be significantly different in terms of dust properties, and a fixed dust grain model may not be appropriate.

In Figure 6.3, I show the residuals for THEMIS used in a two-ISRF environment (orange bars), and THEMIS and MC11 models in a multi-ISRF environment (green bars). As a reference, I keep the results for the simplest THEMIS model (i.e., "single ISRF"; red bars). The FIR residuals for the MC11 model do not show improvements with respect to those of a single ISRF environment (Figure 6.2, purple bars). At $\lambda \leqslant 24$ μm, it follows THEMIS with the same environment, and hence does not have strong assets. At long wavelengths ($\lambda \geqslant 100$ μm), THEMIS, in the two environments described in this section, has residuals centered on 0, and are no longer shifted below 0 as is the case for the single-ISRF model. This is most visible in the SMC (top

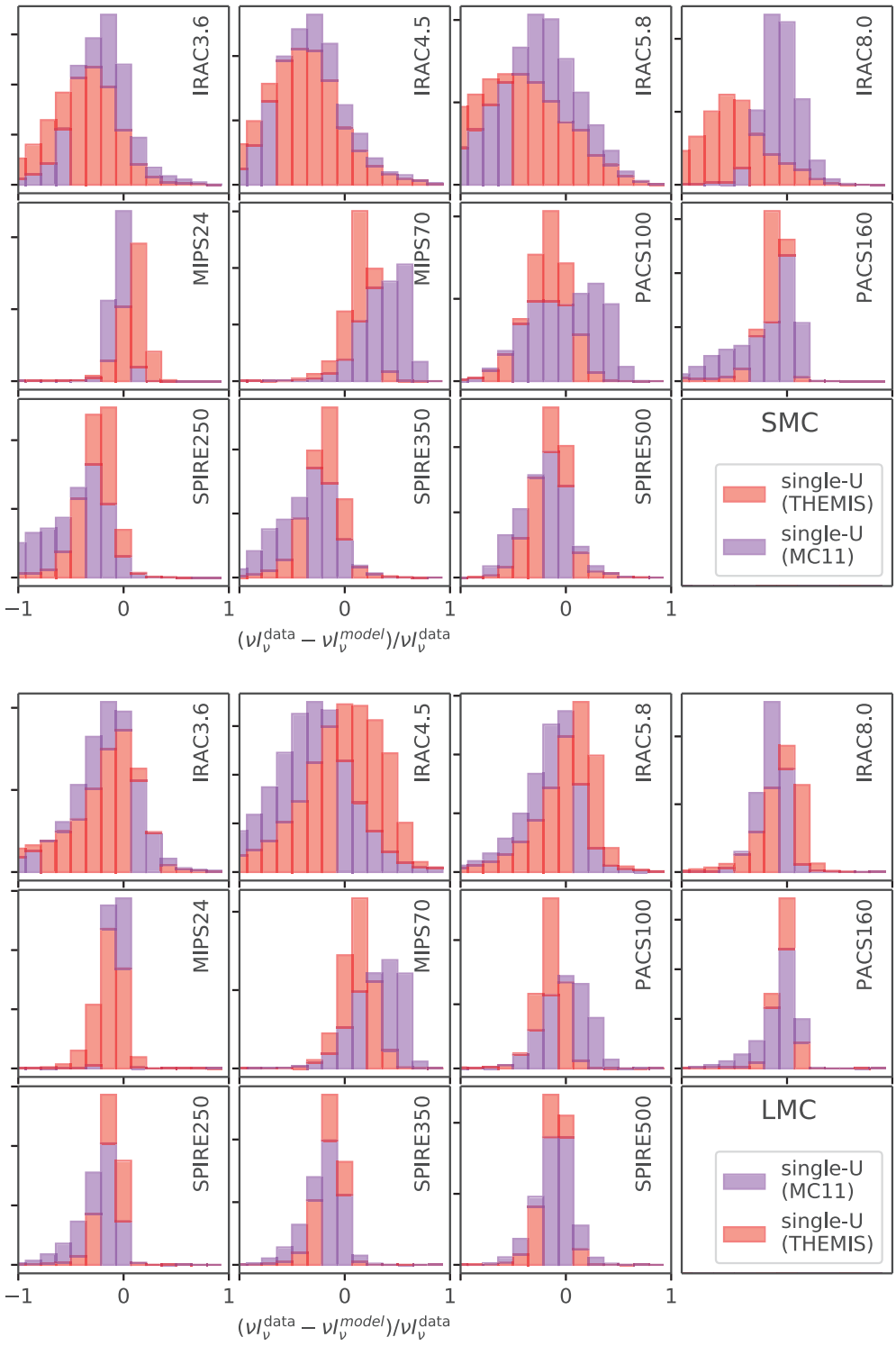

Figure 6.2: Histograms of fractional residuals for the MC11 (purple) and THEMIS (red) models in a single ISRF environment in the SMC (top) and the LMC (bottom). On the upper panel, triangles and squares show the residuals for the same faint and bright pixels, respectively, as Figure 6.1; colors correspond to the models.

panel). In the LMC (bottom panel), the single-ISRF model provides a relatively good fit, and the improvements of the other models are less significant.

We can see the multi-ISRF model improves the fits at 5.8 μm $\leqslant \lambda \leqslant$ 70 μm in both the SMC and LMC. Mixing the dust heated by different ISRFs notably helps to match the data at 8.0 and 24 μm. Using only two ISRF components does not seem enough, and this model reproduces the same SED as a single-ISRF model at these wavelengths. The efficiency of using a power-law is due to its effect on the 8/24 μm slope. By steepening it, it matches both the NIR and MIR data better. After this section, I no longer use the MC11 model. It suffers from strong divergence with the data and the effects brought by using more than a single ISRF do not improve the quality of the fits.

6.3 Varying the small grain size distribution

We saw in Section 6.1 that a single ISRF does not match the data at short wavelengths very well: the residuals are broad and mostly negative (i.e., the model overpredicts the observations). In Section 6.2, I tested different environment changes to try to better account for the shape of SEDs. But variations in grain size distribution can also have an impact on the shape of the dust emission. In THEMIS, the small grain size distribution is described by a power-law, partly defined as $dn/da \propto a^{-\alpha_{\rm sCM20}}$, where a is the grain radius. In order to obtain better fits at these wavelengths (3.6, 4.5, 5.8, 8.0, 24 μm), I investigate the impact of changing the sCM20 size distribution. In this approach, I keep a single ISRF but allow the $\alpha_{\rm sCM20}$ parameter to vary.

In Figure 6.4, I show the residuals for this variation (light blue) in the SMC (top), and the LMC (bottom). In both galaxies, the fits at $\lambda \geqslant 70$ μm are not improved by this model compared to a simple single ISRF (red bars). However, the residuals show that this model matches the data better at short wavelengths, particularly in the SMC. The peak of the residuals are centered on 0 and the residuals are less broad. This improvement is due to the change in the shape of the SED brought by the free parameter $\alpha_{\rm sCM20}$. When $\alpha_{\rm sCM20}$ decreases, the 8/24 μm slope steepens. This helps to decrease the model values in the MIR. In a more physical aspect, when $\alpha_{\rm sCM20}$ is lower, the sCM20 mass distribution is rearranged and it leads to fewer very small grains.

The SMC and the LMC exhibit two different fitting results to the $\alpha_{\rm sCM20}$ parameter, which can vary between 2.6 and 5.4. In the LMC, I find $\langle\alpha_{\rm sCM20}\rangle \sim 5.0$, that is, the default value set in the THEMIS model to reproduce MW dust emission. In the SMC, I find $\langle\alpha_{\rm sCM20}\rangle \sim 4.0$, with $\alpha_{\rm sCM20} < 4.0$ in bright regions (e.g., N66, N76, N83) or H II regions (e.g. S54). The improvement in the residuals comes from a better fit in these regions allowed by a different SED shape in the IRAC and MIPS24 bands. Bernard et al. (2008) found that changing the power-law coefficient of the VSG of the Desert et al. (1990) model from 3.0 to 1.0 helps matching the data and decreases the 70 μm excess, and the estimate goes in the same direction.

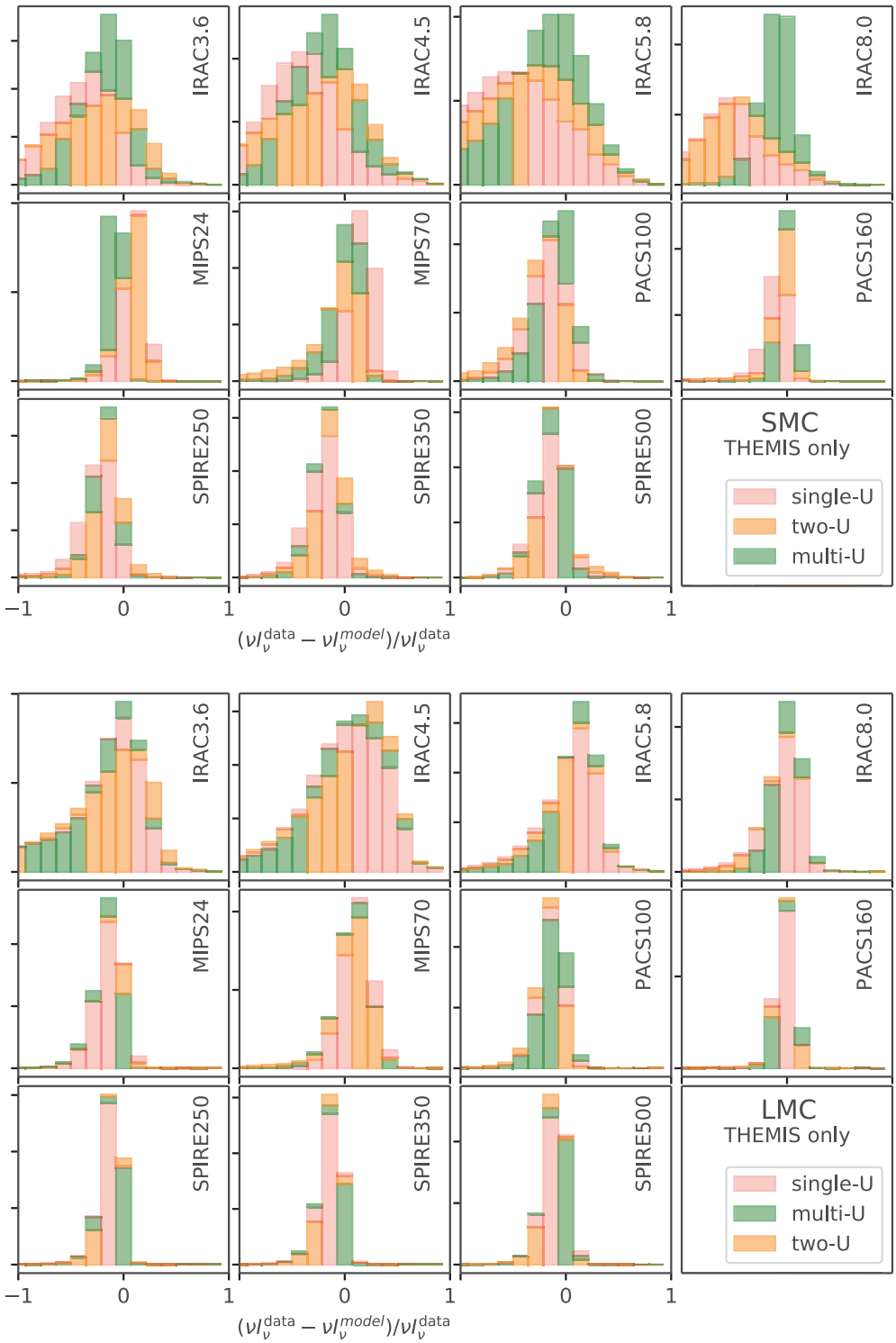

Figure 6.3: Histograms of fractional residuals for THEMIS in a two-ISRF (orange bars) and a multi-ISRF (green bars) environment, in the SMC (top), and the LMC (bottom). For reference, THEMIS in a single ISRF is shown in red bars.

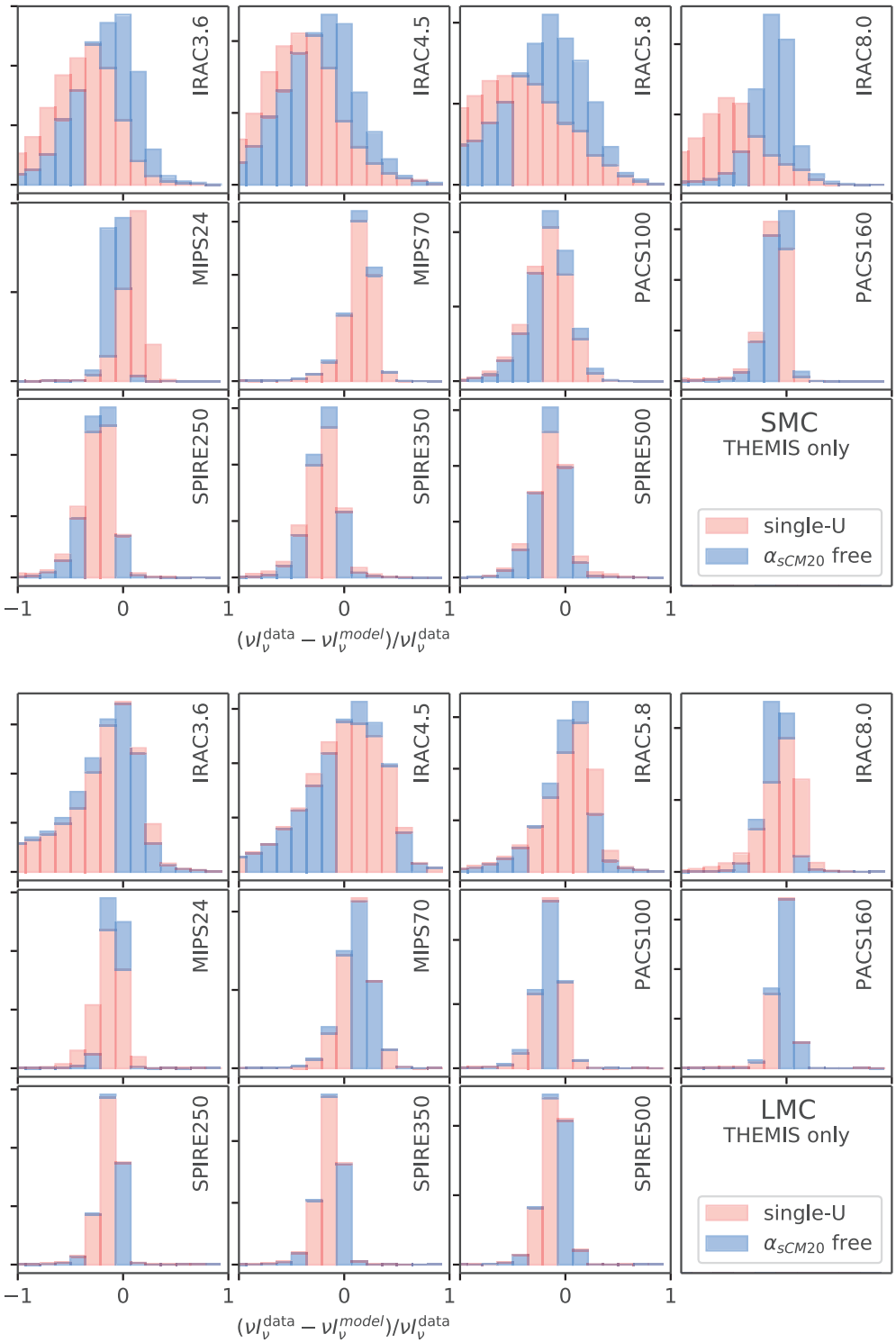

Figure 6.4: Histograms of fractional residuals for THEMIS in a single ISRF environment with a change of the sCM20 size distribution (blue bars) in the SMC (top) and the LMC (bottom). For reference, THEMIS in a single ISRF is shown by red bars.

7

Dust properties inferred from modeling

Based on the results from the residual study (described in Section 6), I focus on the output from the models that best reproduces the observations: THEMIS, in a two-ISRF environment, a multi-ISRF environment, and with α_{sCM20} free in a single-ISRF environment. I investigate the dust properties that are inferred that way.

7.1 Parameter spatial variations

I investigated the spatial variations of the parameter distribution by building parameter maps. The maps show strong differences from one model to another.

In Figures 7.1 and 7.2, I show the maps of the resulting scaling factors Y_{i} for i={aSilM5, lCM20 and sCM20} (first, second, and third rows, respectively), in the SMC (top) and the LMC (bottom), for the two-ISRF, multi-ISRF, and α_{sCM20} free models (first, second, and third columns, respectively). The first and third rows (Y_{aSilM5} and Y_{sCM20}) show the most striking variations. I only display meaningful pixels, that is, pixels where the result is higher than its uncertainty, in color. For example, in the upper-right corner of Figure 7.1 (top), the very few pixels displayed are the only significant pixels. I emphasize that the same pixels were fitted in each case, and the discrepancies in the images come from variations in results. As a guide, the faint gray patterns show all fitting pixels, including those with no good fits.

The silicate fitting, discussed in the following section (7.2), is strongly affected by the choice of heating environment in both galaxies, although it is particularly noticeable in the SMC. Using a multi-ISRF model reduces the number of poorly-constrained fits (i.e., with an upper limit). On the other hand, the α_{sCM20} free model leaves an extensive portion of the galaxy with unconstrained fits (not-shown pixels, with an upper limit on silicate abundances, that is, a large uncertainty). The results in the LMC appear to be less variable from one model to another. As seen from the residuals, the models match the LMC observations better than they match the SMC observations. This difference may come from the constraints put on the silicate spectrum shape, which seem to vary from one model to another. In the case of a multi-ISRF model, the emission of silicates is significant at 70 μm. The total flux in this band (MIPS70) thus has a stronger silicate contribution. This means the silicate spectrum has one more constraint, at a shorter wavelength. This could be the reason for the improved fitting result compared to other

models where the MIPS70 bands are mostly constrained by smaller grains. The more "constant" results in the LMC likely come from the fact that they are closer to MW SEDs, upon which the dust grain models are calibrated.

The $Y_{\rm lCM20}$ fitting results (second rows) do not show strong variations from one model to another. In the SMC, all the pixels are fitted, and the discrepancies are actual fitting results. In the LMC, the results are once again less variable and seem to be trustworthy. I compared the resulting fitting parameter maps to those derived by Paradis et al. (2009). They used the Desert et al. (1990) model to fit the *Spitzer* emission of the MCs. It should be noted that their study and ours do not use the same model nor the same fitting technique. They found that the $Y_{\rm PAH}/Y_{\rm BG}$ ratio is higher in the LMC bar, in both cases, with a single ISRF and with a multi-ISRF model. Such a behavior does not appear in these maps. I do not find any spatial trend in the distribution of $Y_{\rm sCM20}/(Y_{\rm aSilM5}+Y_{\rm lCM20})$. However, it is difficult to rigorously establish a comparison as even the grain species are not defined in the same way in the different studies.

The $Y_{\rm sCM20}$ fitting results are sensitive to the model. The results from the $\alpha_{\rm sCM20}$ free model shows regions with more sCM20 that can be correlated to some extent with H II regions, traced by H_α (Gaustad et al. 2001). The distribution of the $Y_{\rm sCM20}$ parameter in the last column is due to the change of size distribution of the small grains. Changing the power-law coefficient of the sCM20 size distribution has one main advantage: it steepens the 8/24 μm slope. This helps to fit the 8 and 24 μm bands in the SMC, as shown in Figure 6.4. However, it raises the IR emission peak of the small grains. In regions where $\alpha_{\rm sCM20}$ is very low, the IR peak can be fitted by the sCM20 species, and requires only a small contribution of the large grains.

7.2 Silicate grains abundance

In Section 7.1, we saw that the silicate grains component is highly model-dependent, and that most of the pixels are not fit with a reliable uncertainty (Figure 7.1). The figure shows that the SMC and the LMC do not exhibit the same results, and that the SMC is more sensitive to the model than the LMC.

In both galaxies, I find pixels that show a likelihood where the silicate component is only constrained as an upper limit (i.e., all models below a given abundance of silicates have the same probability). From the likelihoods in the pixels with an unconstrained value of the silicate component, I can quote a 3-σ upper limit for the absence of the silicate in the fitting. This upper limit is $Y_{\rm aSilM5} \sim 10^{0.4} {M^{\rm aSilM5}}_{\odot}/M_{\rm H}$, in both the SMC and the LMC.

In Figure 7.3, I show likelihoods of the free parameters $Y_{\rm aSilM5}$, $Y_{\rm lCM20}$, $Y_{\rm sCM20}$, and Ω^* in two pixels: one that shows a good constraint on the amount of silicates (blue line), and one constraining $Y_{\rm aSilM5}$ with an upper-limit only. The results in the two galaxies differ: in the LMC, $\sim$ 10% of the pixels show this kind of likelihood; in the SMC, more than 50% do not show a fully-constrained fit. In Figure 7.4, I display two representations of the SED fitting in the same pixels used for the likelihoods of Figure 7.3. I used 'realizations' of the likelihoods (as in Gordon et al. 2014, see Section 6). The realizations are a weighted sample from the likelihood. The opacity of the color in Figure 7.4 represents the probability of the value in the SED (the more opaque the color, the higher the probability). The top panel shows a very broad region with decreasing probability (i.e., increasing transparency) towards the observational values, whereas the bottom panel depicts a constrained fit (i.e., opaque colors).

Using the upper limit, the silicate/carbon mass ratios for the variations on THEMIS (single-, two-, multi-ISRF and $\alpha_{\rm sCM20}$ free) ranges from $\sim 0.2-0.7$ in the SMC and $\sim 0.3-1.0$ in the LMC. The ratios vary from one model to another. There is only a slight evolution between the two galaxies, but this ratio considerably differs from that of the MW ($\sim$ 10). In all cases,

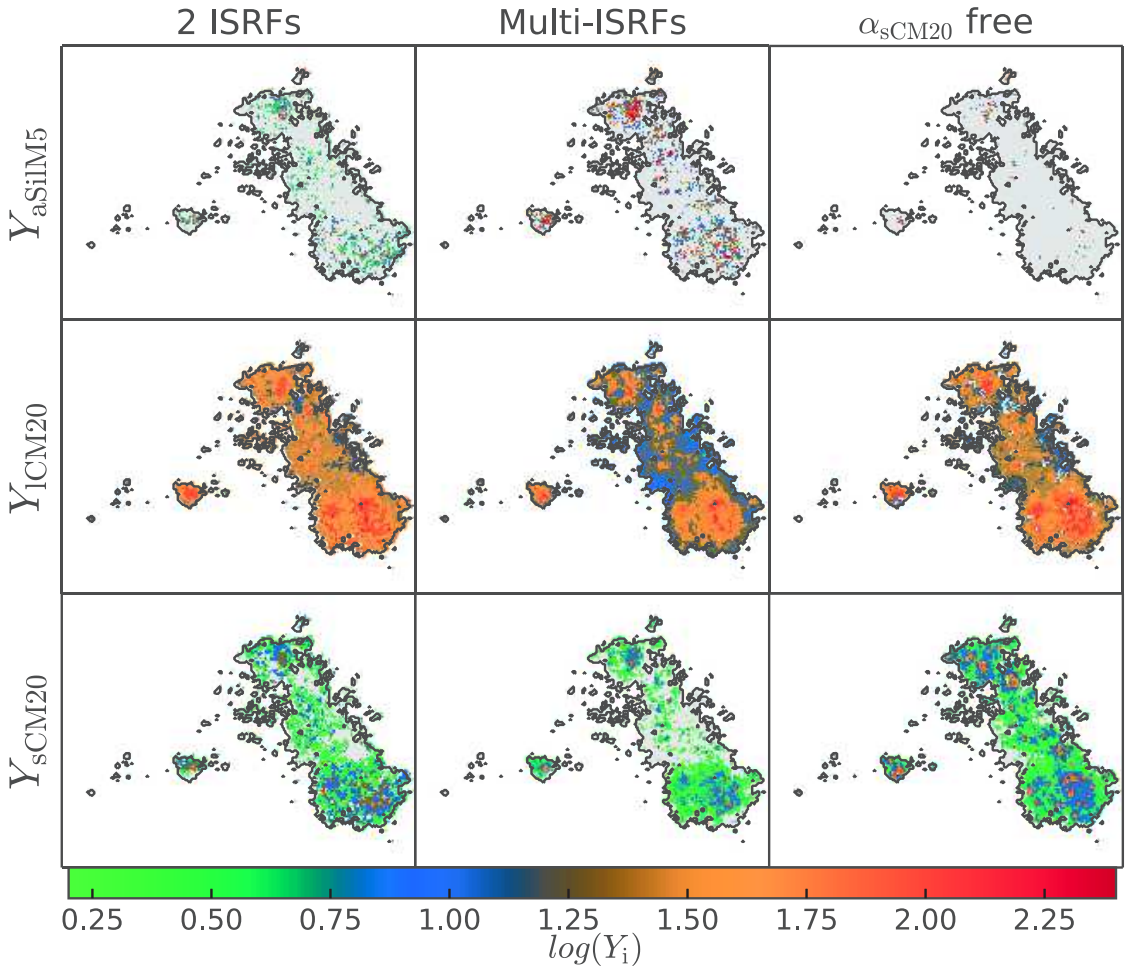

Figure 7.1: Parameter maps in the SMC from THEMIS fits of $Y_{\rm aSilM5}$, $Y_{\rm lCM20}$, and $Y_{\rm sCM20}$ (first, second, and third rows, respectively) for the two-ISRF, multi-ISRF, and $\alpha_{\rm sCM20}$ free (first, second, and third column) models. The gray background represent all fitted pixels. We notice strong discrepancies from one model to another. The spatial variations are dependent on the dust heating environment, especially for the silicate and small carbonaceous grain components.

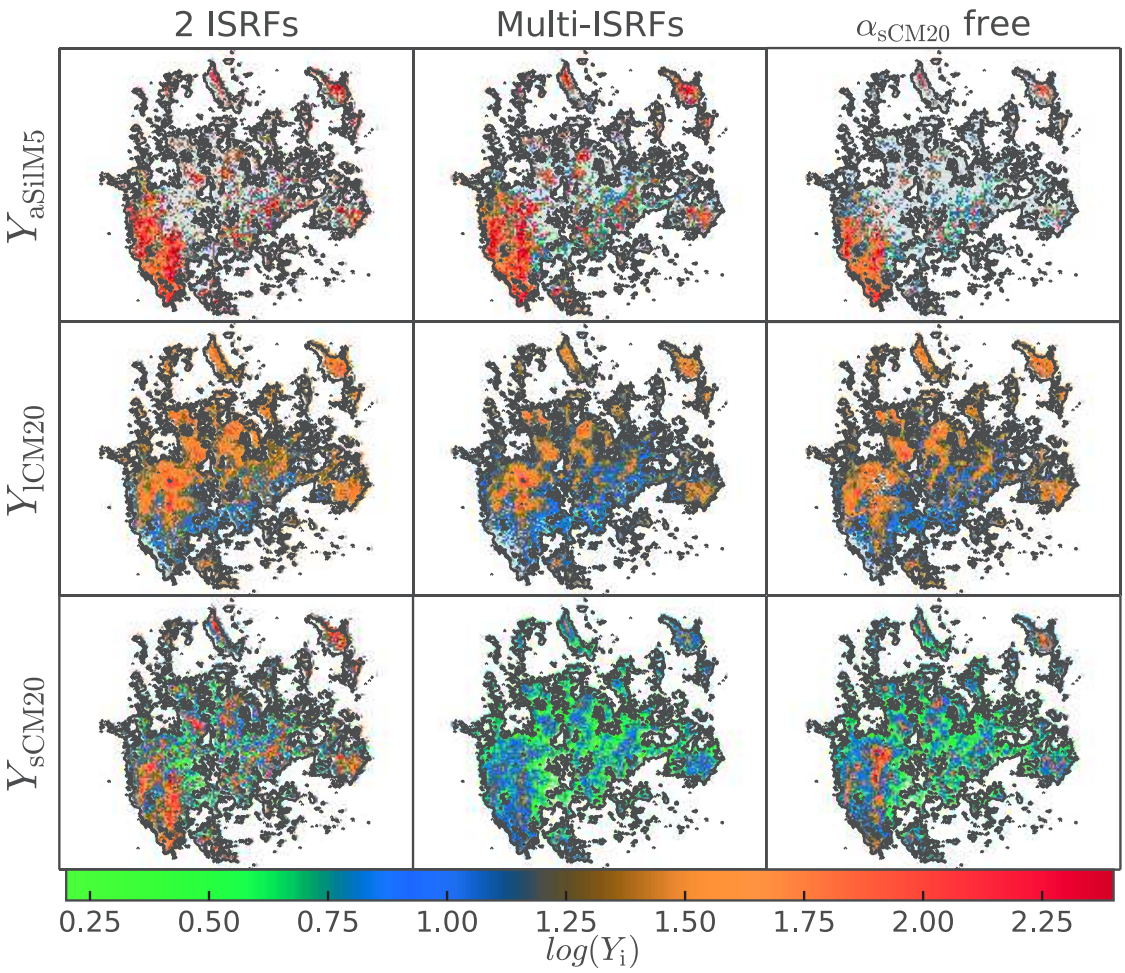

Figure 7.2: Parameter maps in the LMC from THEMIS fits of $Y_{\rm aSilM5}$, $Y_{\rm lCM20}$, and $Y_{\rm sCM20}$ (first, second, and third rows, respectively) for the two-ISRF, multi-ISRF, and $\alpha_{\rm sCM20}$ free (first, second, and third column) models.

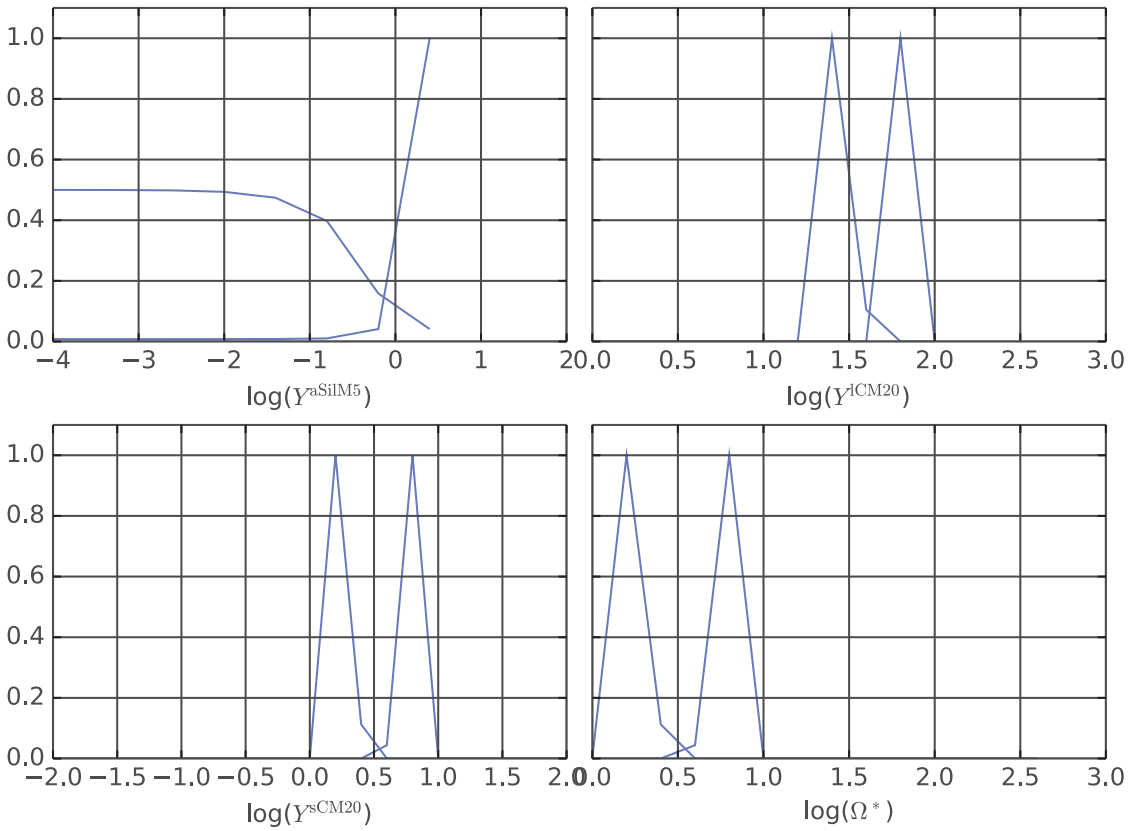

Figure 7.3: Marginalized and normalized likelihoods of the Y_{aSilM5}, Y_{lCM20}, Y_{sCM20}, and Ω^* parameters for two pixels in the SMC: a pixel showing an upper-limit in the Y_{aSilM5} fit (red-dashed line) and a pixel showing well-constrained fits (blue line).

more than 97% of the fitted pixels exhibit a ratio well below the MW value. It appears that the abundance of the silicate component should vary spatially in the MCs, and should be different from that of the MW.

In order to test the requirement of the silicate grains component in the fit, I performed fits using a single large grain species with THEMIS, either carbonaceous or silicates, instead of allowing the two to vary. The large carbon species alone provides a good fit to the SMC IR peak: the residuals strictly follow that obtained for THEMIS with a single ISRF and both, independent, grain components, and show no requirement for an additional silicate component. On the other hand, if I only allow a silicate population, we observe a very broad and multi-modal residual distribution. This is expected as the silicate emission is too narrow to fit the SMC IR peak between 100 and 500 μm. Unlike the SMC, the LMC SEDs require both species to reproduce the data. A model without silicate grains follows the trend of a "complete" model but does not match the data as well and a model without large carbon does not follow the observations.

I also perform a fit for which I tie the two populations, meaning that the silicate and the large carbon populations have to vary together the same way and keep the same initial ratio, that of the local ISM, given by Jones et al. (2013) to be ~ 10. In this case as well, the residuals are again large and bi-modal at long wavelengths.

These results indicate that the silicate/carbon mass ratios in the SMC and LMC are not the same as that in our Galaxy.

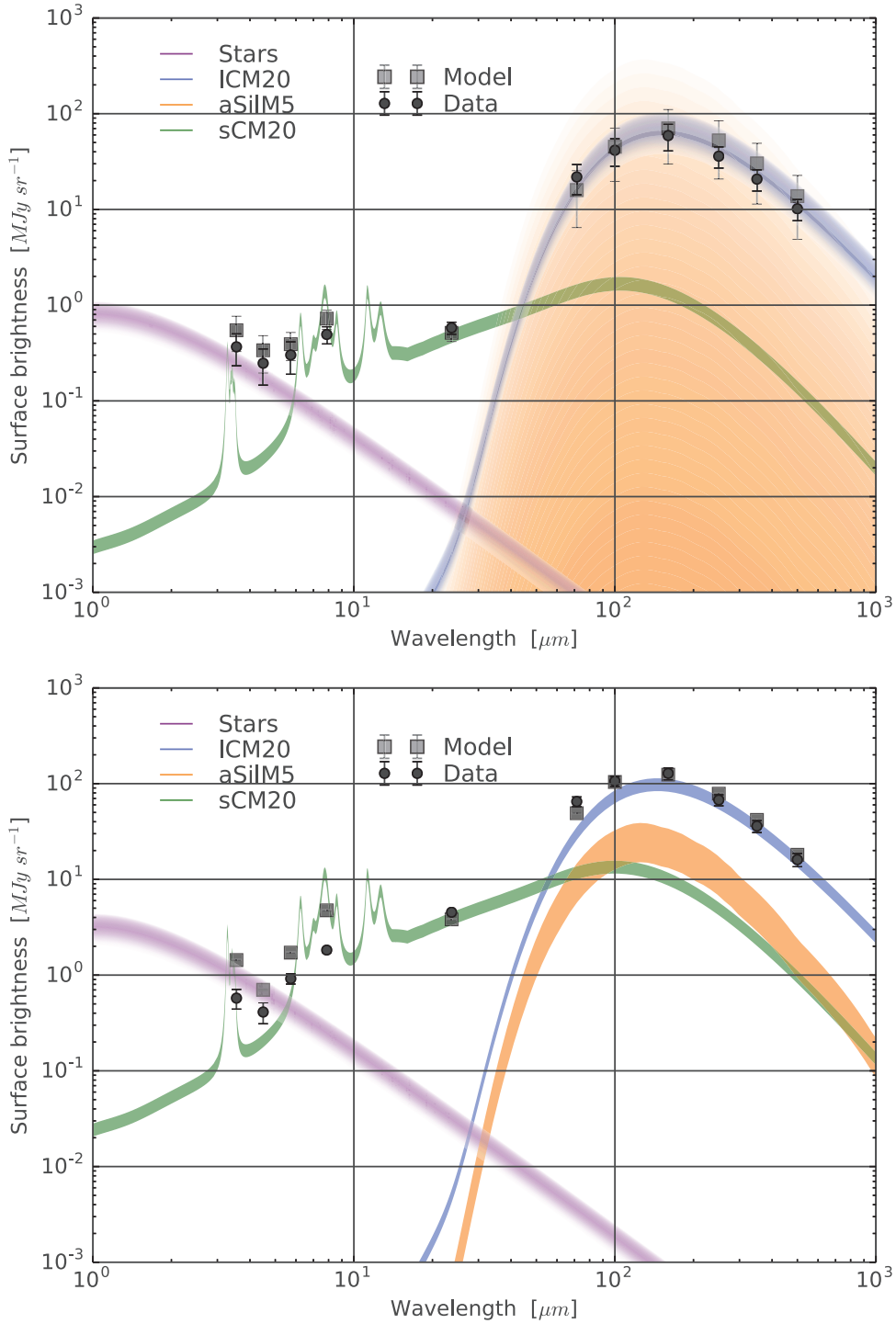

Figure 7.4: Visualization of the unconstrained (*top*) and constrained (*bottom*) silicate fit. In the top panel, the different transparency surfaces show the possible range for the final silicate value, that is, very broad and uncertain. On bottom panel, the same technique is used to draw a constrained fit.

7.3 Dust masses and gas-to-dust ratios

I computed total dust masses to assess whether or not the models produce reasonable amounts of dust in each case. I use multiple realizations of the likelihood in each pixel to estimate the total dust mass uncertainty. Contrary to the maximum likelihood or the expectation value, the realization samples the likelihood and therefore takes into account the contribution that the fitting noise, for each pixel, makes to the uncertainty in the total dust mass.

I created 70 maps from the realizations; where the sum of every one of these maps gives a total dust mass. The final total dust mass is the average of the realizations. Uncertainties on this value are given by the distribution of the total dust masses. I derive the total dust mass from pixels that are detected in eight bands (see beginning of Section 6) of the fit, at a level of at least 3σ above the background noise. This corresponds to a surface of $\sim 2.1 \times 10^6$ pc^2 ($\sim 1.8^{\circ 2}$) in the SMC and $\sim 1.0 \times 10^7$ pc^2 ($\sim 14^{\circ 2}$) in the LMC. The dust masses are given in Table 7.1; they range from ~ 2.9 to 8.9×10^4 M$_\odot$ in the SMC and ~ 3.7 to 4.2×10^5 M$_\odot$ in the LMC, for THEMIS. I gather the results in the form of dust mass $\pm$ statistical uncertainty $\pm$ systematic uncertainty. The statistical uncertainty comes from the quality of the fits. It is very low due to the number of constraints I have. The systematic uncertainty comes from our understanding of the models and their limitations. More precisely, I refer to the uncertainty on dust properties such as emissivity (e.g., Weingartner & Draine 2001; Draine & Li 2007; Gordon et al. 2014), density, and the approach to building the optical and heating properties of dust grains (e.g., Mie theory, spherical grains). I also include degeneracies that come from the choices of ISRF (e.g., a softer ISRF with more dust mass or a stronger ISRF with less dust mass).

Given the constraints on the requirement for a pixel to be fitted, there are a large number of 'undetected' pixels. However, altogether, these regions may contribute significantly to the dust-mass estimation. In order to take these pixels into account, I average their emission in each band to get an average SED. I fit this SED with the same models, and multiply by the surface area of all the undetected pixels to obtain a total dust mass. In the SMC, including the contribution from pixels below the detection threshold increases the dust masses given in Table 7.1 from 50 to more than 100%, doubling the mass in some cases. This is due to the very sparse pixel detection in this galaxy. The 'undetected' area is approximately 10 times larger than the area covered by pixels detected. In the LMC, the 'undetected area' is approximately the same size as the fitted area and accounts for $\sim 10-20\%$ of the dust mass; H I mass, and GDR for detected and undetected pixels are given in Table 7.1.

In Figure 7.5, I gather some of the dust masses found in the literature for the Magellanic clouds and this work. The dust masses I derived in this study are smaller than those estimated by previous studies, especially for the simplest model. One interpretation of this difference lies in the carbon grains dominating this model fitting. The silicate emissivity is lower than that of large carbonaceous grains (~ 5 cm^2 g^{-1} and ~ 17 cm^2 g^{-1} at 250 μm, respectively). Therefore, for identical luminosity, if the fit uses only carbon grains, it requires less dust to produce the same flux than if it used both carbon and silicates. Because the best results indicate a very small contribution of silicates, this eventually leads to a lower dust mass. The environment, through the definition of the ISRF, seems to have a strong impact on the dust masses. Although it is hard to evaluate a quantitative difference with residuals (Section 6), the final dust masses with a mixture of ISRF are closer to the values found in other studies.

I performed a test fit to verify this assumption: in THEMIS, I tied the large grain populations (aSilM5 + lCM20) together, using a single-ISRF approach. In this process, the information regarding the independent distribution of the two types of grains is lost, but this resulted in dust masses that are closer to those from Gordon et al. (2014), especially in the SMC; the LMC

Table 7.1: Dust masses and GDR in the SMC and the LMC.

Model	Pixels > 3σ detection		Including pixels < 3σ detection	
	M_{dust} [$M_\odot$]	GDR	M_{dust} [$M_\odot$]	GDR
		SMC		
THEMIS single ISRF	$2.86 \pm 0.005 \pm 0.8 \times 10^4$	~ 4100	$6.83 \pm 0.007 \pm 1.9 \times 10^4$	~ 1750
THEMIS 2 ISRFs	$8.93 \pm 0.04 \pm 2.5 \times 10^4$	~ 1300	$2.65 \pm 0.08 \pm 0.8 \times 10^5$	~ 500
THEMIS multi-ISRFs	$7.68 \pm 0.02 \pm 2.3 \times 10^4$	~ 1500	$1.20 \pm 0.07 \pm 0.3 \times 10^5$	~ 1000
THEMIS α_{sCM20} free	$6.25 \pm 0.01 \pm 1.7 \times 10^4$	~ 1900	$1.01 \pm 0.009 \pm 0.3 \times 10^5$	~ 1200
MC11	$3.44 \pm 0.006 \pm 1.0 \times 10^5$	~ 350	$3.71 \pm 0.006 \pm 1.1 \times 10^5$	~ 910
		LMC		
THEMIS single ISRF	$3.74 \pm 0.004 \pm 1.1 \times 10^5$	~ 650	$4.51 \pm 0.008 \pm 1.3 \times 10^5$	~ 550
THEMIS 2 ISRFs	$4.25 \pm 0.01 \pm 1.2 \times 10^5$	~ 570	$4.89 \pm 0.04 \pm 1.4 \times 10^5$	~ 500
THEMIS multi-ISRFs	$3.81 \pm 0.004 \pm 1.1 \times 10^5$	~ 650	$4.73 \pm 0.005 \pm 1.4 \times 10^5$	~ 520
THEMIS α_{sCM20} free	$4.21 \pm 0.005 \pm 1.3 \times 10^5$	~ 580	$4.88 \pm 0.008 \pm 1.4 \times 10^5$	~ 500
MC11	$2.05 \pm 0.001 \pm 0.6 \times 10^6$	~ 120	$2.11 \pm 0.002 \pm 0.6 \times 10^6$	~ 170

Note: The total H masses in the SMC and the LMC are 1.2×10^8 $M_\odot$ and 3.3×10^8 $M_\odot$ for pixels above the 3σ detection, and 2.4×10^8 $M_\odot$ and 3.62×10^8 $M_\odot$ when accounting for pixels below the 3σ detection.

being only slightly affected by the change. This seems to confirm the assumption that the low dust mass I find comes from the carbon grain-dominated fitting results.

The gas-to-dust ratio (GDR) estimation of a galaxy varies depending on the approach. Following Roman-Duval et al. (2014), I determined GDRs using H I measurements (Stanimirovic et al. 2000; Kim et al. 2003), and CO measurements (Mizuno et al. 2001) converted to H_2 mass estimations. The GDR estimations are thus really *hydrogen*-to-dust ratio, but, for clarity, I keep the 'GDR' notation. I use the conversion coefficients $X_{CO} = 4.7 \times 10^{20}$ cm^{-2} (K km s^{-1})$^{-1}$ from Hughes et al. (2010) for the LMC and $X_{CO} = 6 \times 10^{21}$ cm^{-2} (K km s^{-1})$^{-1}$ from Leroy et al. (2007) for the SMC. I report values of GDR in Table 7.1. As mentioned above, the dust masses with this model fitting are lower than the masses found by other works. This translates to higher gas-to-dust ratios. Roman-Duval et al. (2014) found GDR of $\sim$ 1200 for the SMC and $\sim$ 380 for the LMC, using dust surface density maps from Gordon et al. (2014). From Table 7.1, the GDR values derived from the favored fits (two-ISRF and multi-ISRF models) range from 1000 to 1200 in the SMC, and from 500 to 520 in the LMC. Using the model with tied large grains, we find GDRs lower than those found by previous studies ($\sim$ 700 in the SMC and $\sim$ 400 in the LMC), and the shape of the observed SED is not well reproduced.

These GDRs show some variations (a factor of $\sim$ 2 in the SMC between the higher and lower values). In order to assess a stronger constraint on the GDR, I compare these results to independent results given by depletion measurements or extinction.

Using the MW depletion patterns and the MCs abundances, one would expect GDRs of 540-1300 in the SMC, and 150-360 in the LMC. This assumes a similar dust composition and evolution between galaxies at different metalicities. I find values approximately 2 times higher than this. Tchernyshyov et al. (2015) used UV spectroscopy to derive depletions in the MCs. They found that scaling the MW abundances to lower metalicity, although approximately

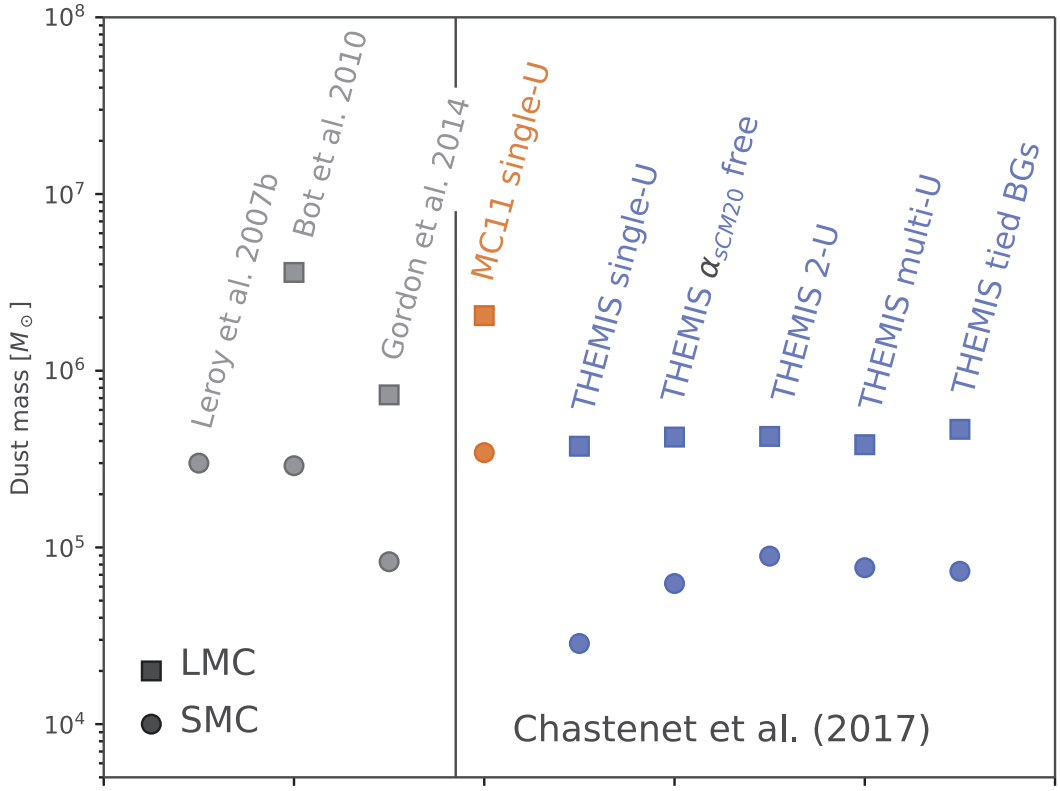

Figure 7.5: Summary of the dust masses. Results from this work (right of the dashed line) are lower than previous studies. This likely comes from the low silicate abundances found in this paper.

correct in the LMC, can lead to significantly different numbers in the SMC than those derived with depletions. From their results, they predict a range of GDRs: 480-2100 in the SMC and 190-565 in the LMC. My results fall within these limits. Their measurements were restricted to the diffuse neutral medium (DNM). Since I cover the diffuse to dense parts of the galaxy, one would expect more dust inferred from my fitting and thus, slightly lower GDRs.

Another way to predict GDR is to use extinction measurements. Gordon et al. (2003) measured the dust extinction and H I absorption column in the SMC and LMC, deriving N(H I)/A(V) values. I determined the corresponding GDR expected from their results, using:

$$\frac{1/\mathrm{GDR_{SMC}}}{1/\mathrm{GDR_{MW}}} = \frac{[\mathrm{N(H\,I)/A(V)}]_{\mathrm{MW}}}{[\mathrm{N(H\,I)/A(V)}]_{\mathrm{SMC}}} \tag{7.1}$$

with $\mathrm{DGR_{MW}} = 1/150$. I used the averaged values in the SMC Bar, LMC, and LMC2 (supershell) from their sample. I find reasonable values compared to their work.

Globally, my GDRs are in agreement with other studies that use different sets of measurements than IR emission. My fits manage to reproduce the observed SEDs and fall within reasonable ranges for dust masses and GDR. Previous studies have gathered GDR estimations from numerous programs and estimated a trend between the metalicities of galaxies and their gas-to-dust mass ratios (e.g., Engelbracht et al. 2008a,b; Galametz et al. 2011; Rémy-Ruyer et al. 2014). I report my GDRs with the metalicity of the MCs (12+log(O/H) $\sim$ 8.0 in the SMC and $\sim$ 8.3 in the LMC Russell & Dopita 1992) and found that the values are in agreement with the trend.

8

Exploring the impact of inferred dust properties

8.1 Grain formation/destruction

Results from this first study on dust emission in the Magellanic Clouds indicate that the silicate grains are not found in the same amounts in the LMC and the SMC with respect to carbon grains. The fits show that the silicate/carbon ratio is unlikely the same in the MW, LMC, and SMC.

The lack of fully constrained fits of the silicate component suggests a deficit in silicate grain abundance, particularly in the SMC. This deficit could either be explained by less formation or by more destruction of silicate grains. Bocchio et al. (2014) showed that silicate grains are less easily destroyed than carbon grains in supernovae (SNe) due to their higher material density. This may therefore indicate that the higher abundance of carbon grains that I obtain is due to more efficient carbon dust formation rather than selective silicate destruction. This could be consistent with the low metalicity of this galaxy. It is well established that carbon stars form more easily at low metalicity (e.g., Marigo et al. 2008). Nanni et al. (2013) showed that such carbon stars are efficient producers of carbonaceous dust. With the carbon excess, O-type dust is unlikely to form due to the absence of M-type stars. Recent work by Dell'Agli et al. (2015) investigated the evolution of AGB stars in the SMC using *Spitzer* observations. Using color-color diagrams built from photometry and modeling, they identify C-rich and O-rich stars at various masses. They found discrepancies between their distribution in the LMC and SMC. The amount of O-rich AGB stars in these samples is lower in the SMC than in the LMC, which is $\sim 5\%$. This idea is in agreement with depletion studies (e.g., Welty et al. 2001; Tchernyshyov et al. 2015).

Yet, other studies have found constraints on the amount of silicates in the SMC. Weingartner & Draine (2001) constrained grain size distribution in the MW, LMC, and SMC from elemental depletions and extinction curves. They adjust a functional form for each grain population (carbonaceous and silicate). In the case of the SMC, they reproduced the extinction curve toward AzV398 from Gordon & Clayton (1998), in the SMC-bar. Their results indicate a larger amount of silicate dust than carbon dust. Their result is therefore opposite to ours. However, I did not

make observations of the same nature, nor did I use the same dust models. In the following sub-section, I investigate the extinction curves in the MCs.

8.2 Extinction curves

Past programs measured extinction curves in the MCs, and have assessed discrepancies with the extinction curves in the MW (steeper far-UV slope, absence of 2175 Åbump). Gordon et al. (2003) analyzed observed extinction curves in the MCs (5 in the SMC and 19 in the LMC) and derived R_V values. In their sample, most of the curves could not be reproduced using the relationship based on MW extinction curves. They found 4 curves in the LMC (Sk -69 280, Sk -66 19, Sk -68 23, and Sk -69 108) that show a MW-like extinction curve.

The goal here is to verify if a fit of the dust emission in the MCs allows us to reconstruct the observed extinction in the line of sight available. I did not try to directly fit the MCs extinction curves and the corresponding SED in emission at the same time. I extracted extinction curves at the same positions indexed in Gordon et al. (2003) (4 in the SMC – I did not fit the pixel corresponding to the AzV456 position, and all 19 in the LMC). Using the derived quantities for each grain species from my fits, I calculated extinction curves with the DustEM outputs. I only derived extinction curves for the single-ISRF model and the model where $\alpha_{\rm sCM20}$ is free. In the multi-ISRF model, the dust composition does not change when I compute the mixture spectra, therefore each extinction curve is the same and I do not use this variation to infer conclusions.

In the LMC, I reproduce the extinction observations in the four lines of sight that showed a MW-like shape. In the SMC, none of the extinction curves can be reproduced using the dust population derived from IR emission fitting. This is also true for the rest of the LMC sample. In Figure 8.1, I show two results of extinction curves derived from the IR fitting (all curves are shown in Appendix A). I plot the observed and modeled extinctions in AzV -66 88 (LMC) in the right panel. The $\alpha_{\rm sCM20} = 5.4$ is very close to the default value in the single-ISRF model. Given the similar abundance values, the modeled extinctions are therefore comparable. In the SMC (left panel, AzV 398) as well, $\alpha_{\rm sCM20} = 5.4$ and the result is close to that of a single-ISRF. In other lines of sight (e.g., AzV 214), a lower $\alpha_{\rm sCM20}$ (e.g., ~ 3) helps to match the near-IR part of the observed extinction ($1 \leqslant \lambda^{-1} \leqslant 3$). However, in both cases, the steep UV slope is not well fit at all.

When the shape of the extinction curve is different from that of the MW, the dust properties inferred from IR emission correspond to an extinction curve that do not match that observed in the UV. This could be due to the nature of dust grain models that are based on a MW calibration. It could also be due to a poor constraint on the small grain population by the IR emission, because the starlight and dust emission are mixed at those wavelengths. Either fitting the IR emission solely is not a good approach for deriving a quantitative impact of the small grains on the extinction, or the small grain population needs to be split in order to derive various properties that do not affect emission and extinction in the same way. This result accounts for the differences one may find when separately fitting the dust emission and extinction. Weingartner & Draine (2001) used one extinction curve in the SMC (toward Azv398) to constrain a size distribution. They found a larger amount of silicate than carbon. In the same line of sight, the result from fitting the emission reproduces the observed extinction. However, allowing for a larger amount of silicate than carbonaceous grains, as suggested by Weingartner & Draine (2001) results, does not help to match the IR observations.

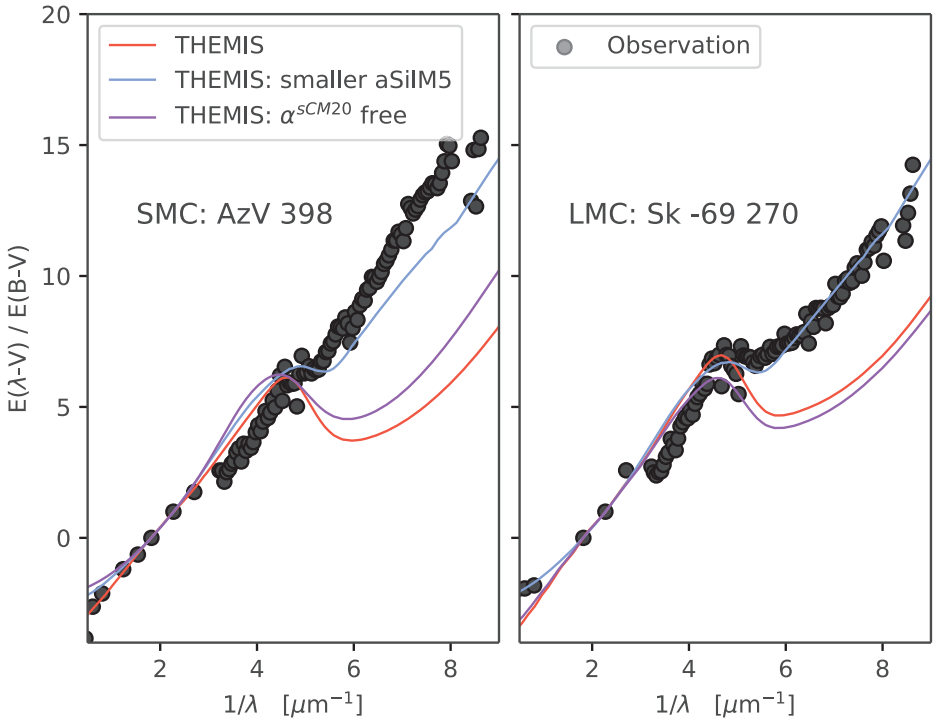

Figure 8.1: Observed extinction curves (grey circles) in the LMC (*right*: Sk -68 129) and the SMC (*left*: AzV 398). I overplot the dust extinction derived from IR-emission fitting for a single-ISRF (dark red line) and a $\alpha_{\rm sCM20}$ free model (purple line), and with smaller silicate grains (blue line, see Section 8.3.2).

8.3 Other variations in dust models

In this study, I investigated the change of model SED shape through variations in the ISRF environments, and by allowing independent grain variations. I showed that such changes significantly increase the quality of the fits, especially in the SMC. Those variations mainly affect the $8-100$ μm range by steepening the $8/24$ μm slope and/or broadening the IR peak around 100 μm. Other studies can provide more suggestions for changing the composition of dust models.

8.3.1 Change in carbon size distribution

Köhler et al. (2015) studied the dust properties evolution from diffuse to dense regions. For example, they showed that grains with an additional mantle have different properties that can lead to a steepening of the FIR slope and a lower temperature. They also investigated the influence of forming aggregates in dense media. In that case as well, the dust properties vary significantly. Such approaches could be helpful for fitting the MCs dust emission. In Figures 6.2 to 6.4, we can see THEMIS is slightly above the observations in the FIR (at 250, 350, and 500 μm). A steepening of the spectral index may suggest that the model would better match the data at these wavelengths.

Ysard et al. (2015) also investigated the variations of dust properties observed with *Planck*-HFI. In their study, they investigated the impact of varying the carbon abundance, while keeping the silicate abundance constant. They found that this variation could help reproduce the observation and account for the dust variations. They showed that changing the size distribution (by changing the aromatic-mantle thickness or the size distribution function) participates in the dust variations. This provides additional evidence that a single model with fixed size distribution is not appropriate for fitting observations on a galaxy scale.

8.3.2 Allowing smaller silicate grains

Bocchio et al. (2014) computed size distribution, emission, and extinction curves for carbonaceous and silicate grains from THEMIS in environments where dust is destroyed/sputtered by shocks with $v \sim 50-200$ km/s. At sufficiently high shock velocities, carbon grains are mostly destroyed, whilst silicates are fragmented into smaller grains due to their collisions with small carbon grains. Using their silicate grain size distribution leads to a steepening of the far-UV extinction. Looking at the peculiar shape of the SMC extinction, this approach seems interesting. Once again, I want to know if fitting the dust emission can yield a good estimation of the dust extinction.

Allowing for smaller silicate grains helps to match the data in the IRAC bands, in the SMC. In the LMC, on the other hand, the residuals are not affected significantly, and the fits are not improved. However, in both galaxies, we notice a change in the extinction shape. The far-UV slope is closer to the observations. In Figure 8.1, the cyan-dashed lines are those derived for a fit of the emission with smaller silicate grains. In the SMC, two lines of sight are significantly improved by the change in the silicate size distribution. My results still exhibit a small bump around 2175 Å, because I allow the small carbonaceous grains to vary. In the LMC, some lines of sight are greatly affected and the extinction can be matched with smaller silicates; see, for example, the left panel of Figure 8.1.

I only applied the new size distribution to a single-ISRF environment to test the resulting extinction with DustEM. In terms of dust masses, the new fits lead to $\sim 4.4 \times 10^4$ $M_\odot$ in the SMC,

and $\sim 2.0 \times 10^5$ $M_\odot$ in the LMC, respectively higher and lower than a single-ISRF environment, without the change in size distribution.

8.3.3 On the recalibration

In this study, I used a different reference SED to rigorously compare models after they were recalibrated on the same Galactic values. However, it should be noted that the models are not defined as such. In THEMIS, the GDR is set to approximately 134 (Ysard et al. 2015). Without recalibration, I would obtain a dust mass of $\sim (1.9-5.6) \times 10^4$ $M_\odot$ in the SMC, and $\sim (2.3-2.7) \times 10^5$ $M_\odot$ in the LMC, for the different variations of environment. THEMIS mass distribution for the grain populations is different than in other dust models (e.g., Draine & Li 2007). For example, the silicate (pyroxene and olivine type) grains have a lower specific mass density. Therefore, the model needs less silicate mass. We can also notice that the carbon mass is mostly found in small carbonaceous grains.

In order to get a more accurate mass estimation, one possible path of investigation is to use the different versions of the model to fit the various media of a galaxy, namely dense or diffuse. In THEMIS, dust in the transition from the diffuse ISM toward dense molecular clouds is described with aSilM5 and lCM20 grains coated with an additional H-rich carbon mantle. Inside dense molecular clouds, further evolution is assumed and THEMIS dust consists of aggregates (with or without ice mantles).

All methods and results up till this section have been publish in Chastenet et al. (2017). I explored other leads after publication, that I describe here.

8.4 Impact of the ISRF shape

As we have seen in the Introduction, the dust emission is dependent on the surrounding energy provided by stars, which is modeled as the ISRF. Thanks to the design of the DustEM tool, it is possible to directly change the ISRF shape, in addition to changing its intensity with a scaling factor. The work of Mezger et al. (1982) and Mathis et al. (1983), presented in Section 1.3 of the Introduction part, has determined the shapes of ISRF at various distances D_G from the Galactic center. Their studies provide us with ISRF at D_G =5, 6, 8, 10 and 13 kpc. Although the ISRF at $D_G = 10$ kpc is the most used, there is no a priori reason to think that a single ISRF shape is a realistic choice to model dust emission in galaxies. Their star formation rates, ages or the distribution of dust are not unique, and they all directly affect the ISRF. Adapting the predicted dust emission in our model based on a different estimations of starlight energies seems to be a reasonable approach.

I fit the same data sets using THEMIS, in environments recreating different ISRF hardness. To do so, I implemented the ISRF from Mezger et al. (1982) and Mathis et al. (1983) at all galacic radii (not just the solar neighborhood), into the right format for DustEM., allowing me to derive new dust emission spectra. I then built a library of dust models following the approach presented in Section 6.1. The goal was to let the fit choose between different shapes of ISRF as well as its intensity.

The maps showing the type of ISRF chosen are displayed in Figure 8.2. The first striking difference is the average ISRF value in each galaxy. In the SMC, a hard ISRF at $D_G = 5$ kpc (dark blue in Figure 8.2) apparently fits well the data, while a softer ISRF at $D_G = 13$ kpc (dark red in Figure 8.2) is mostly chosen in the LMC. We know the two galaxies are not at the same stage of star formation, and we can therefore suspect the global energy absorbed by dust would

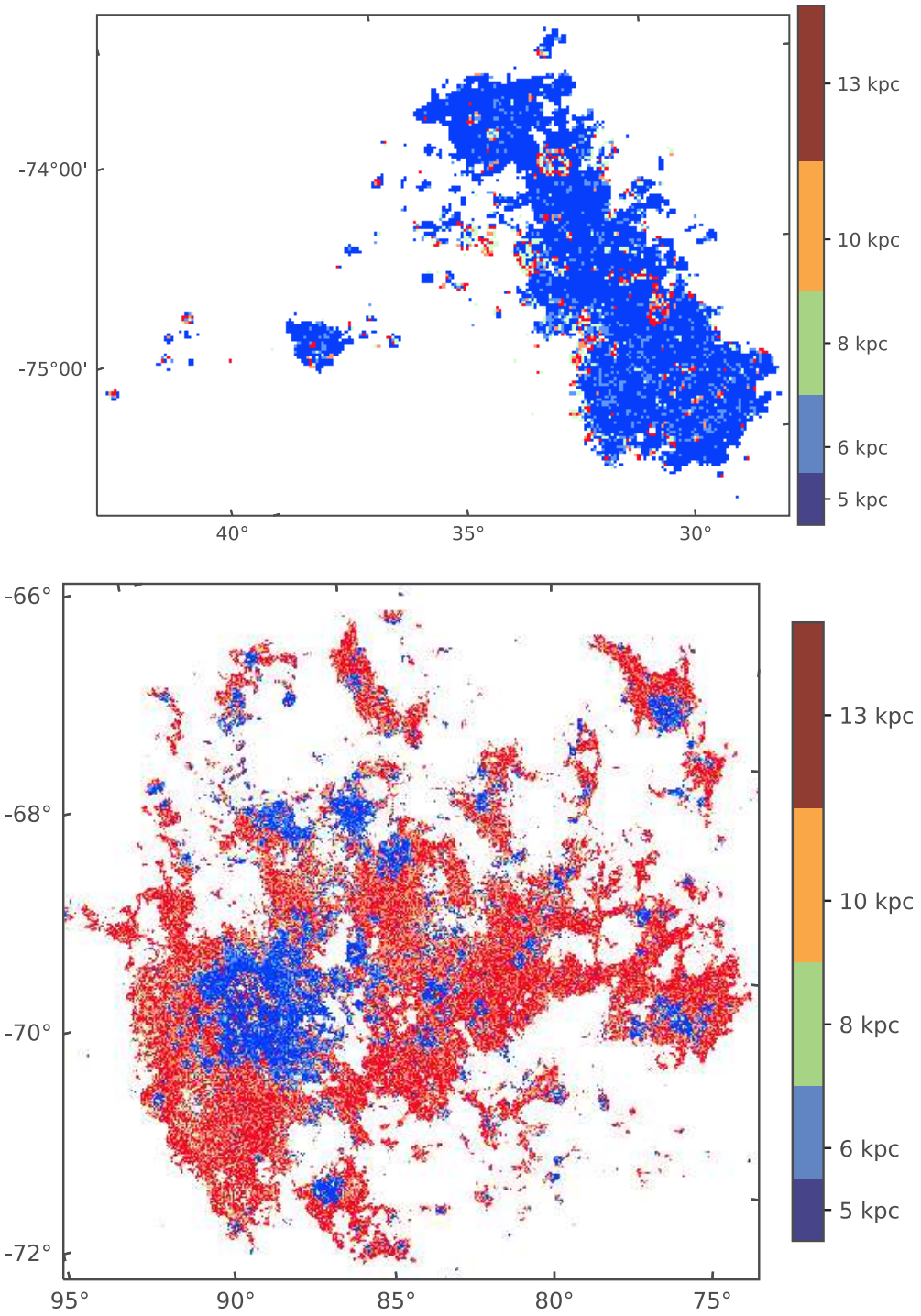

Figure 8.2: Values of the ISRF distance D_G from a fit allowing for various ISRF shapes, in the SMC (*top*) and the LMC (*bottom*). The two galaxies show striking differences: the LMC is better fit with a soft ISRF while the SMC shows the hardest value.

not be identical. This could be the reason of this difference of preferred ISRF shape between the MCs.

However, we can also notice the spatial variations within each galaxy. This is most visible in the LMC, where harder ISRF seems to be better to fit dust emission in brighter regions. These regions, in blue in the right panel of Figure 8.2, appear to be located at the same position as HII regions, where ionized gas is present. The same behavior was noticeable with the α_{sCM20} parameter in Section 6.3. Once again, it indicates that the shape of the dust emission is not the same in these regions, requiring a change in predicting the emission spectrum. In the SMC, it looks like the H II regions also show a different result than the rest of the galaxy, but in a more unexpected way. In these regions, where the energy heating dust should be greater, the fit shows that a softer ISRF is better at reproducing the data. It is surprising, and not understood at this time, but further investigations could bring more insights on this result.

Nonetheless, this approach is interesting as it shows that not all galaxies behave the same way in terms of preferred shape of ISRF. It means that, as suspected, a single ISRF is not necessarily sufficient to accurately reproduce dust emission in other galaxies. At the very least, it depicts a need to change the predicted dust emission spectrum, in a way or another.

8.5 Using Draine & Li (2007)

I fit the Magellanic Clouds dust emission with the DL07 model. I used the MW-based model, and not the size distributions that were based on MCs observations in Weingartner & Draine (2001). Further use of these models has shown that they were not able to fit the MCs themselves.

The D07 model does not provide a significantly better fit to the Magellanic Clouds than THEMIS overall. On Figure 8.3, I show the residuals for the SMC (left) and the LMC (right).

Figure 8.4 shows the parameter maps in the SMC (top), and the LMC (bottom). We can notice some difference in the values of the parameters, which vary between both galaxies. For instance, the q_{PAH} value in the SMC appears to be on average smaller than in the LMC. In the former, the average value for q_{PAH} is around 1%, while in the latter, it is 4%. It is consistent with the Draine et al. (2007) results on q_{PAH} as a function of metallicity. It may indicate a difference in dust evolution, either in PAH formation or their destruction. It is possible that a stronger radiation field sputters the PAH, reducing their abundance. In both galaxies, we do not observe a significant value of q_{PAH} at high U_{min}. The β value (power-law coefficient for ISRF integration in the DL07 model (see Section 12.2.1), also seems slightly higher in the LMC than in the SMC, on average. A higher β translates into more weight of the small U in the integration. In the LMC, we can see a relation between this parameter and γ (the relative weight of the dust mixture at various temperatures, and the dust heated at a single temperature). In regions where β is high, i.e. with more impact of the small U, the best fit chooses a small γ, i.e. putting all the weight on the dust heated at a single temperature. This could be interpreted as, in each pixel, a single bright star dominates the dust heating and can be modeled without requiring multiple sources. This opposition is not as visually striking in the SMC, and does not seem to happen.

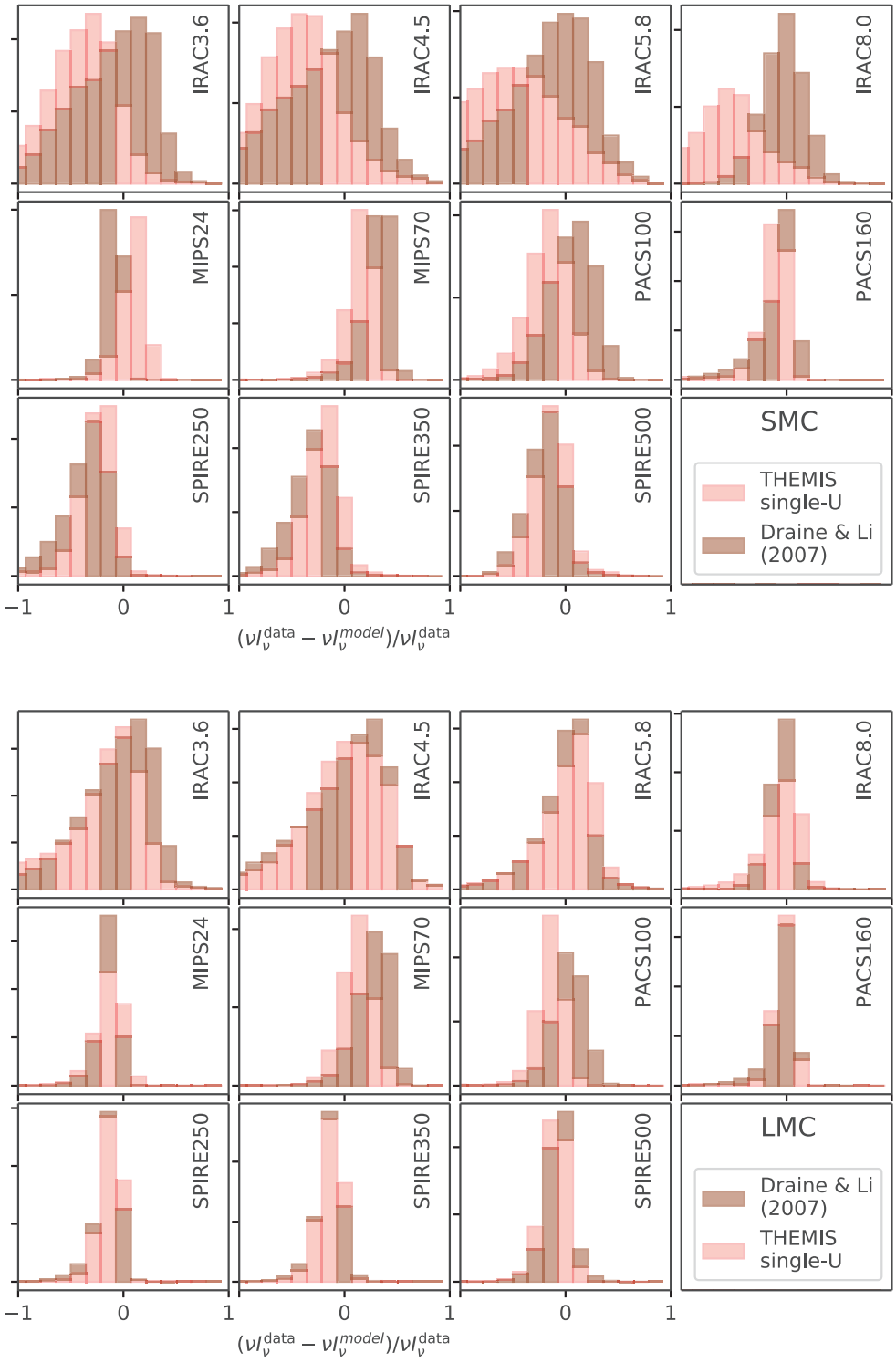

Figure 8.3: Histograms of fractional residuals for DL07 (brown bars) in the SMC (top) and the LMC (bottom). For reference, THEMIS in a single ISRF is shown by red bars.

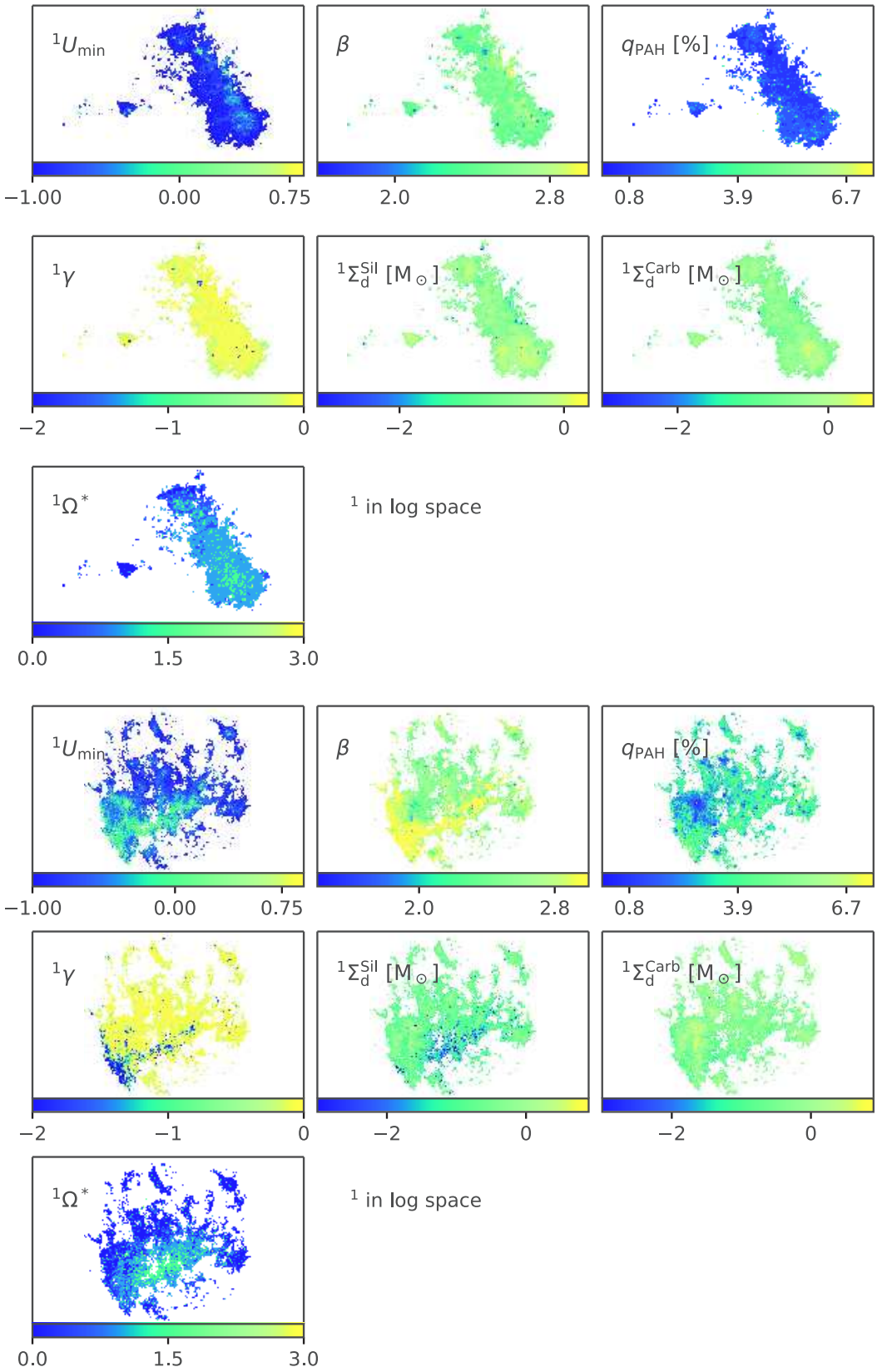

Figure 8.4: Parameter maps of the Magellanic Clouds fit with the DL07 model. Striking differences appear between the SMC and the LMC.

9

Conclusions and perspectives on dust in the Magellanic Clouds

I fitted the *Spitzer* SAGE and *Herschel* HERITAGE observations of the Magellanic clouds at ~ 10 pc, in 11 bands from 3.6 to 500 μm. I used three physical dust grain models: Compiègne et al. (2011), THEMIS (Jones et al. 2013; Köhler et al. 2015) and Draine & Li (2007) to model dust emission in the IR.

Globally, I find that the Compiègne et al. (2011) model should not be used in this context as it suffers from strong discrepancies with respect to the observations (e.g., large-grain steep emissivity in the FIR). Fitting THEMIS on the observations gives better residuals, especially in the SMC. THEMIS leaves a small deficit in the residuals in the FIR, that is, it is too low compared to the observations, in opposition to what has been identified in previous studies at an excess at 500 μm. I find that using more than a single ISRF greatly improves the quality of the fit. More generally, a change in the shape of the model SED will help to get better residuals, either by using more than a single-ISRF environment, or by changing the dust grain size distribution, with respect to the one calibrated on the diffuse ISM in the solar neighborhood. Parameter maps depict very model-dependent spatial variations. The approach chosen for the dust environment (ISRF) strongly affects the quality and result of the fits.

Using the THEMIS dust model, I find that the silicate abundance is estimated only as an upper-limit $Y_{\rm aSilM5} \sim 10^{0.4} M_{\odot}^{\rm aSilM5}/M_{\rm H}$, while the large carbonaceous grain emission is constrained with well defined peaked likelihood distributions. The silicate/carbon ratio implied by the fits indicates an evolution between the MW and the MCs. This ratio is approximately 10 in the MW, but is not the same or constant throughout the MCs ($\leqslant 1$ in the SMC and LMC). Tests forcing a MW-like silicate/carbon ratio lead to very broad residuals and poor fitting, confirming that this ratio should not be kept constant for these galaxies.

The dust masses derived in the LMC from my fitting are lower than those derived by other studies by a factor lower than two, but remain close given the uncertainties (of $\sim 30\%$ total). In the SMC, the values are in agreement with the literature (e.g., Gordon et al. 2014) but suffer from large uncertainties. The numerous pixels with the low upper-limit on silicate abundance are mostly responsible for the slightly lower dust masses (especially in the SMC), because the carbonaceous grains have a lower mass.

I used the dust emission results to create modeled extinction curves. I find that fitting only the emission cannot give results that can be applied directly to match the measured dust extinction in the MCs. These tests showed that a change in the estimated grain size distributions (based on MW measurements) would be needed to (more) accurately match the MCs extinction from an emission fitting (e.g., different silicate grain distribution, namely smaller).

Further work will use additional dust grain models for comparison (e.g., Draine & Li 2007, THEMIS with aggregates), while the goal should remain the same, that is, to compare dust emission/extinction results from various dust models using a strictly identical fitting technique. In order to fully interpret these data, a more detailed approach, for example taking into account the gas-phase transitions, is needed (but is beyond the scope of this paper). A radiative transfer technique should also be used to understand the errors of the assumptions made when developing a dust model. The simplest heating environment 'single-U' is unlikely to be enough to fit dust emission in nearby galaxies, and the more sophisticated one ('multi-U') is empirically chosen. A more realistic approach, compared to the more simple descriptions, could be helpful in improving dust emission fitting techniques.

Linking the emission and the extinction was only briefly mentioned in this thesis. Another approach to what we have seen would be to directly fit the emission *and* the extinction *at the same time*. This is not an easy step, but could provide important clues on the connections between dust properties that can be seen in emission and those that can be seen in extinction. Can both observables be adjusted correctly with our current models? Or can we fit them well only separately? If the ISRF hardness and intensity can be constrained with the emission, what variations does that allow in extinction? Extinction curves can show strong differences from a line-of-sight to the next: how does that affect the fit in emission? Can we see strong difference in the dust properties in those cases?

Even though polarization was not used in this work, it is another dust property that can be observed. A recent appeal to this characteristic is becoming more and more important in dust studies, in particular with the availability of the *Planck* data. Dust grain alignment with the magnetic field is a clue to its composition properties, and its surroundings. It is another observable that could be linked with extinction and emission.

PART II – TAKE AWAY

The results in this second part have been published in Chastenet et al. (2017). We wanted to fit the dust emission in two nearby galaxies with different full dust models, using a consistent fitting technique.

What did we show:

- although they fit the MW diffuse ISM emission, all dust models are not equal when it comes to fitting IR emission of other galaxies. Dust characteristics like the FIR slope is critical in that matter, and THEMIS appears to give better results.
- In terms of dust masses, THEMIS agrees within the errors with results in the literature. Choosing a less well-fitting model to fit the IR emission leads to a difference of an order of magnitude in dust masses.
- The spatial variations of derived parameters are sensitive to the choice of dust heating environment. Considering a single-temperature dust or dust elements heated at various temperature impacts the results.
- Within the Magellanic Clouds and from a galaxy to the other, a varying Silicate/Carbonaceous grains ratio implies that dust composition is not the same as in the MW. Although the Silicate abundance is estimated with an upper limit, the MW reference value for this ratio is rarely found.
- Dust extinction curves from emission properties in the Magellanic Clouds do not match the observations. However, variations in size distributions seem to be promising.
- Studying the impact of the ISRF shape on dust emission fitting appears to bring interesting conclusions, showing striking differences from a galaxy to another.

That last remark will be our starting point for the next part. We will investigate the importance of a better estimation of the dust heating environment, compared to the approaches we have used in this part.

Part III

Systematics in Dust Modeling

10

Using radiative transfer in dust studies

The next part of this thesis focuses on using a more sophisticated and less empirical approach to model the dust heating. As we have seen in the previous parts, dust observables, and therefore the properties that we derive, are highly dependent on the surrounding radiation field, and hence the photons that dust grains can absorb, or scatter. Not only the intensity of the radiation field, i.e. the number of photons available, is an important factor, but also their energy $h\nu$ will strongly change the shape of the spectrum of the resulting dust emission. Moreover, highly energetic UV photons can sputter small dust grains, and generate a new grain size distribution, rendering our dust models inaccurate. To take into account the mixing effects, we use an empirical power-law of the ISRFs, to mix dust elements at various temperatures. However, we do not know for sure the limitations of that assumption. Moreover, in this case, only the intensity of the ISRF changes, and not its shape. Knowing the radiation field at different positions in a cloud with the best accuracy possible is of great importance to model dust. Thanks to the improvements in computer technologies, speed and storage space capacities have rapidly increased, allowing for fast and long computations, necessary for radiative transfer calculations.

10.1 The Radiative Transfer method

The dust radiative transfer (RT) aims at understanding the transport of radiation in a more or less dusty medium. Like we have seen in the Introduction, the interstellar radiation field (ISRF) is defined by its intensity (number of photons) and hardness (energy of the photons). Solving the RT problem means determining the intensity of the radiation field in every position, in all directions, for each wavelength. This leads to greatly increasing the dimensionality of the problem. Dust RT is therefore not a simple thing to do: it is a non-linear and non-local process, and modelers, facing numerous difficulties, are often forced to make assumptions to speed up the calculations. The non-locality happens in the three dimensions: position, direction and wavelengths, making the simplifications very difficult. The RT approach has however become a major problem to tackle in modern astrophysics, since technologies now allow investigating it to some level of details, and because dust remains an –almost– omnipresent component of the universe. It is therefore a critical issue to solve. While observations show structures and complex 3D layouts, the simple (non-RT) approach is unable to convey such intricacy. The

source anisotropy also fails at being recovered if not done with a full 3D geometry. That is why more extensive studies focus on estimating the ISRF in a geometry, and that is why I am interested in using this approach for this study. Using the realistic calculations brought by the RT model, and comparing it to the more simple approach in dust models will allow us to foresee the limitations of our models.

10.2 The Radiative Transfer Equation

The complete radiative transfer equation (RTE) is a 6D integro-differential equation that includes the integral for scattered light and a non-linear coupling between the thermal source term and a double-integral equation. Moreover, the changing nature of the RTE, depending on the varying extinction, makes it very difficult to input into solvers, and is inherently limited by resources, sometimes implying a limitation in the problem itself. We will go over some of the details of the RTE, from a simple form to a more complete expression, and the refinements that can be input.

Solving the RTE means determining the specific intensity $I(\boldsymbol{x},\boldsymbol{n},\lambda)$ of the radiation field, i.e. the amount of energy in a wavelength interval[1]; $\boldsymbol{x}$ represents the position vector, $\boldsymbol{n}$, the direction, and λ the wavelength. The general form of the RTE can be written:

$$\boldsymbol{n}\cdot\boldsymbol{\nabla}I(\boldsymbol{x},\boldsymbol{n},\lambda) = -\kappa(\boldsymbol{x},\lambda)\,\rho(\boldsymbol{x})\,I(\boldsymbol{x},\boldsymbol{n},\lambda) + j(\boldsymbol{x},\boldsymbol{n},\lambda) \tag{10.1}$$

The left hand term describes the specific intensity variation on an infinitesimal distance. The variations are due to interactions with sinks, i.e. a decrease in the intensity: the first term on the right-hand side of the equation (equivalent to absorption), where κ is the the mass extinction coefficient, and ρ the mass density of the medium; or source terms: j, that describe a gain in intensity (due to stars, dust...). The complexity of the RTE depends on the nature of the previous terms (e.g. scattering, dust emission, starlight, absorption...).

It is possible to express the equation in terms of a physical distance s, at position $\boldsymbol{x}$, and in direction $\boldsymbol{n}$. Doing so, and assuming that j does not depend on the intensity I, there is an analytic solution to the general form of the Equation 10.1:

$$I(s,\lambda) = \int_{-\infty}^{s} j(s',\lambda)\,\mathrm{e}^{-\tau(s,s',\lambda)}\,\mathrm{d}s' \tag{10.2}$$

with the optical depth τ being

$$\frac{\mathrm{d}\tau}{\mathrm{d}s} = \kappa(s,\lambda)\,\rho(\lambda) \tag{10.3}$$

In this specific case, it shows that the intensity depends on every position anterior to s.

A physical description of Equation 10.1 is to take into account the primary emission, and the absorption. In that case, the source term becomes $j_*(\boldsymbol{x},\boldsymbol{n},\lambda)$, describing a stellar component adding energy to the radiative transfer. The extinction coefficient is therefore the dust absorption coefficient $\kappa_{\mathrm{abs}}(\boldsymbol{x},\boldsymbol{n},\lambda)$. Although this case is still simple to solve, it leaves a complex part out of the radiative transfer, that unfortunately greatly complicates the problem: scattering.

[1] It can be determined in a frequency interval as well. For notation purposes, we will not use the $I_\lambda(\boldsymbol{x},\boldsymbol{n},\lambda)$ notation, and will get rid of the subscript.

Scattering As explained in the Introduction, scattering is the redirection of the photon in another direction. It is, however, quite complex: the direction in which the photon bounces back is determine by a probability law Φ which depends on dust properties. It is therefore an anisotropic process, and changes the RTE as such:

$$\begin{aligned} \boldsymbol{n} \cdot \nabla I(\boldsymbol{x}, \boldsymbol{n}, \lambda) = & -\kappa_{\text{abs}}(\boldsymbol{x}, \lambda)\, \rho(\boldsymbol{x})\, I(\boldsymbol{x}, \boldsymbol{n}, \lambda) \\ & + j_*(\boldsymbol{x}, \boldsymbol{n}, \lambda) \\ & + \kappa_{\text{sca}}(\boldsymbol{x}, \lambda)\, \rho(\boldsymbol{x}) \int_{4\pi} \Phi(\boldsymbol{n}, \boldsymbol{n'}, \boldsymbol{x}, \lambda)\, I(\boldsymbol{x}, \boldsymbol{n'}, \lambda)\, \mathrm{d}\Omega' \end{aligned} \tag{10.4}$$

where κ_{abs} and κ_{sca} are the absorption and scattering coefficients, respectively. The new direction $\boldsymbol{n'}$ of a photon is given by the scattering phase function $\Phi(\boldsymbol{n}, \boldsymbol{n'}, \boldsymbol{x}, \lambda)$, that describes the probability that a photon moving in direction $\boldsymbol{n}$ will have a new direction $\boldsymbol{n'}$.

The complete RTE equation is quite complex, and some levels of refinement can be implemented but may be less important in some situations. If scattering is inevitable, modelers can decide how much physical input they want to add in the numerical solver. In the following are briefly shown a few of them.

- **Dust mixtures** A dust model, even a simple one, usually describes dust as a mixture of several components, with different chemistry (Section 2.6: carbonaceous and silicate grains), optical properties... To take this variety of properties into account, the RTE can include a sum of terms that translate the presence of multiple extinction coefficients; each κ term in Equation 10.4 is therefore replaced with a sum:

$$\begin{aligned} -\kappa_{\text{ext}}(\boldsymbol{x}, \lambda) &\rightarrow -\sum_i w_i(\boldsymbol{x})\ \kappa_{\text{ext},i}(\lambda) \\ \kappa_{\text{sca}}(\boldsymbol{x}, \lambda) &\rightarrow \sum_i w_i(\boldsymbol{x})\ \kappa_{\text{sca},i}(\lambda) \end{aligned} \tag{10.5}$$

  The $w_i(\boldsymbol{x})$ terms describe the contribution of each grain population to the total dust model.

- **Adding dust emission** Dust absorbs optical/UV light and re-emits the absorbed energy in the infrared. This emission can be included in the RTE with an additional source term $j_{\text{d}}(\boldsymbol{x}, \lambda)$. As seen in Section 2.3, dust grains can be either in thermal equilibrium or stochastic heating. In the first case, the new source term can be written:

$$j_{\text{d}}(\boldsymbol{x}, \lambda) = \sum_i w_i(\boldsymbol{x})\ \kappa_{\text{abs},i}(\lambda)\, \rho(\boldsymbol{x})\, B(T_i(\boldsymbol{x}), \lambda) \tag{10.6}$$

  where $B(T_i(\boldsymbol{x}), \lambda)$ is the Planck function, determined as a function of temperature and wavelength. In the case of stochastic heating, the source term is:

$$j_{\text{d}}(\boldsymbol{x}, \lambda) = \sum_i w_i(\boldsymbol{x})\ \kappa_{\text{abs},i}(\lambda)\, \rho(\boldsymbol{x}) \left[\int_0^\infty P_i(T, \boldsymbol{x})\, B(T, \lambda)\, \mathrm{d}T \right] \tag{10.7}$$

- **Polarization** Dust grains can polarize light. The scattering process leads to polarized photons. In the RTE, it is possible to take this phenomenon into account. If so, we do not solve for the intensity I but for a vector $\boldsymbol{S}$. The scattering term in Equation 10.4 becomes an integral including a matrix which describes the vector $\boldsymbol{S}$.

In the end, one is free to choose the terms to input in the RTE to solve, depending on the amount of resources available and the physical requirements for the chosen situation. Once the RTE is constructed, a technique to solve it must be implemented.

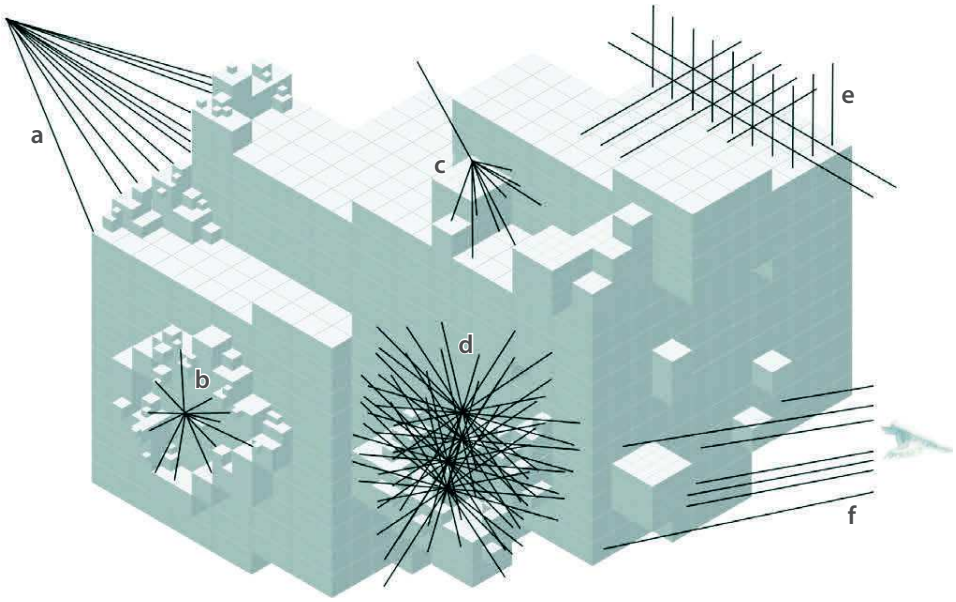

Figure 10.1: The different situations (*a* through *f*) illustrate the possible types of rays used in 3D dust RT, and shows the varying refinement of the grid (see text for situations details). From Steinacker et al. (2013).

10.3 Finding a way to solve

10.3.1 3D Discretization

As evidenced by the numerous terms it can involve, the RTE is a very complex system to solve, just by the very definition of its terms. To be able to numerically solve such equation, discretizing the elements involved in the solution is necessary. It can happen either in the solution space, i.e. a discrete solution vector, or in the dust properties used in the routine. A range of approaches are available to do so. If one chooses to discretize the radiation field intensity grid, they can, among other techniques, either refine it locally, or keep a fixed sampling. They must also choose an approach to discretize the direction space, and the wavelength space. Finally, the dust properties can cover a rather large range of values, if they aim at reproducing the various environments of galaxies (e.g. optical depth from 0.1 to 10); considering the best way to input the dust grain characteristics is a challenging point as well.

10.3.2 Make the photons move

To recreate the reality, a photon package needs to move in the grid, and we must be able to follow its path. A very common method used in computational physics to propagate a wave is the Ray-Tracing method. There again, multiple choices are available, and the level of sophistication depends on the requirements of the solver, and the computational limits. Figure 10.1 shows a sketch of a few kinds of situations that can occur in a 3D grid for radiative transfer. The grid refinement varies according to the situation and the necessity for detailed calculations. The situation *a* corresponds to rays coming from an external source; *b* shows an internal source; *c* shows a ray undergoing a scattering event; *d* is characteristic of multiple scattering events in a high optical depth region; *e* follows a coarse regular grid; and *f* shows rays going to the observers.

10.3.3 Monte Carlo solution

Finally, the solving method needs to be implemented as well. The Monte Carlo (MC) method has been used for a long time in a large number of applications, in various areas, not restricted to physics. Interesting and extensive overviews about MC methods in general, from Whitney (2011) or Steinacker et al. (2013), to name only a few, can be found. For astrophysics purposes, MC methods applied to transport of particles like photons, neutrons or cosmic rays have emerged decades ago (e.g. Mattila 1970; Witt & Stephens 1974). The basic idea in MC is to use random numbers. In the case of RT, this applies to the path of a photon package: along its journey, at each iteration, the new path of the photon package will be determined by randomly sampling a probability distribution function. Essentially, it means that instead of trying to directly solve the RTE previously seen, the MC method treats it in a probabilistic approach. There is therefore a need to generate those random numbers, through an appropriate method. There are multiple ways to do so, and we will review only a few in the following. In both cases presented, the solution emerges after numerous iterations. Each iteration corresponds to a movement of the photons packages. Each package is tracked until it is completely absorbs by dust grains, or until it escapes the grid.

Simple MC

If the dust emission is not used, the simple MC method can be done independently at each wavelength (and therefore can be parallelized).

- The first step is the creation of the photon package, and its input into the computation. It is created according to the source term $j_*(\boldsymbol{x}, \boldsymbol{n}, \lambda)$, and is assigned random position and direction through the respective probability distribution functions.
- The next step is to determine the free path length, or how far the photon package can travel without interacting with a sink/source term. To do so, it uses the optical depth τ, which can be translated into a "physical" distance.
- At the new position, the photon is either absorbed or scattered by a dust grain, and the probability distribution, now discrete, is set by the albedo of the grain $\kappa_{\text{sca}}/\kappa_{\text{ext}}$. In the case of an absorption event, it ends the package path. If the photon is scattered, a new direction $\boldsymbol{n}'$ is determined, and it goes back to the previous step. The repetition and the second and third steps goes on until there are no photons left in the computation space.

In the case of high optical depths, the grain density is high and absorption is more likely to occur than scattering; these situations may induce errors due to the lack of iterations. To compensate, a minimum number of scattering events can be required, and ensure that the calculation is done for a sufficient number of times.

Weighted MC

Although practical, the simple MC method is only valid in 1D and 2D situations, thanks to the multiple symmetries that help to simplify the problem. In the case of 3D RT, such simplifications cannot be made, and one is often required to use acceleration methods. One of them is the weighted MC method, or biasing. It is widely used. The basic idea is to use a different probability distribution instead of the initial one, and then correct it after sampling. The correction is made through a weight, assigned to the photon package, and varies depending on the acceleration method chosen. The recent work from Baes et al. (2016) has focused on this method in this

very kind of application. Here we will name a few possible implementations for acceleration in 3D dust RT:

- if the situation justifies it, one can choose to increase the number of photons in a preferred direction;
- another possibility is to consider each photon package in both absorption and scattering processes: instead of choosing only one outcome, a coefficient is attributed to each process, and propagated through the photons path;
- forcing the photons to scatter, preventing them from escaping the system allows for acceleration, but raises an issue about the end of calculations, if the photons are continuously trapped in the grid;
- to avoid the iteration inherent to the secondary dust emission, one can choose to create a new photon for every absorption event.

These are only a few of the multiple techniques for acceleration, and more extensive reviews will give more insights about each of them.

Dust RT is used in this thesis to create a more accurate distribution of the ISRF. This is meant to contrast with the more simple approach seen in the analysis of dust in nearby galaxies (e.g. for the Magellanic Clouds, in Part II). With the more detailed ISRF, a sample of dust emission spectra is built and analyzed in the same way we would study observations of nearby galaxies. This is detailed in the next Chapters.

11 The DIRTYGrid

The RT calculations used for this thesis come from the RT code DIRTY (Gordon et al. 2001; Misselt et al. 2001). Using this RT routine and a dust emission calculator, Law et al. *(in prep.)* created the DIRTYGrid. This grid provides us with fluxes of dust emission in a number of various environments, re-creating the diverse conditions in nearby galaxies.

11.1 DIRTYGrid description

The DIRTYGrid (Law et al., *in prep.*) uses the DIRTY code and the ISRF determined in each cell to compute the corresponding SED at each position of the grid. Figure 11.1 shows a block diagram of the two routines used to creates the DIRTYGrid. The wavelength range extends from the UV to the submillimeter. Here, we review some important points of this work, crucial to the following study.

The parameters in the DIRTYGrid are meant to cover a large range of galactic properties, as seen in numerous observations. There are seven free parameters in the DIRTYGrid. Three of them are 'discrete':

- grain type: there are three possible choices of grain composition, coming from those used in Weingartner & Draine (2001).
  - The first is a Milky-Way-type dust, based on MW abundances, emission and extinction. Weingartner & Draine (2001) offer different possibilities of such composition, and that in the DIRTYGrid is for $R_V = 3.1$, and $b_C = 6 \times 10^5$ (number of C atoms).
  - The second choice is a LMC-type dust, based on constraints from the super-shell located south-east of 30 Dor[1]. In this case, $b_C = 6 \times 10^5$.
  - Finally, the last choice is an SMC-type grain composition, based on constraints in the SMC Bar (the main structure of the galaxy, see Figure 4.1).

[1] 30 Doradus is the brightest star formation region in the LMC. It is extensively studied for its stellar properties as well as its dust characteristics.

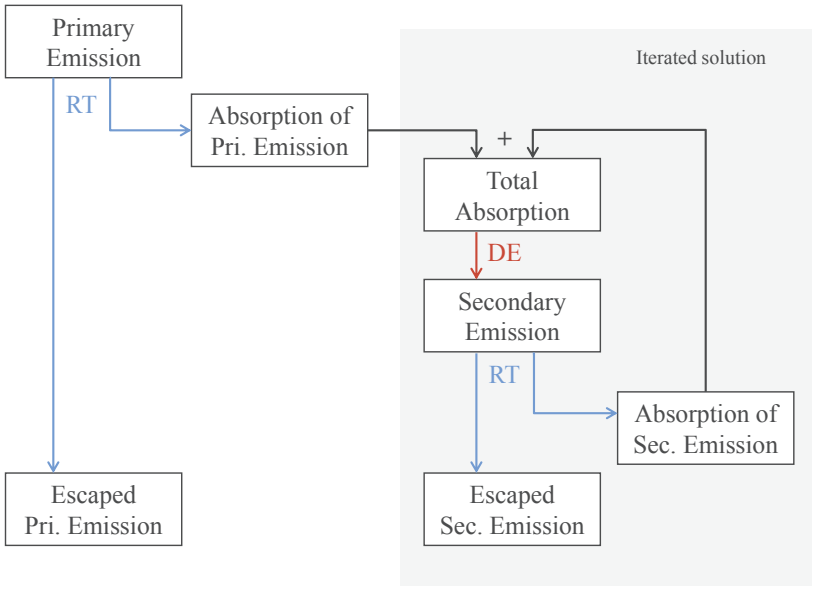

Figure 11.1: Block diagram of the iterations in the DIRTYGrid to produce the dust emission spectra. RT stands for Radiative Transfer; DE is Dust Emission. *Credit:* Law et al. *(in prep.)*

The main difference between these dust compositions are their grain size distributions, calibrated on extinction measurements[2];

- geometry: we can distinguish two points here, the global and local geometries. There are three possible global geometries, changing the relative distribution of dust and stars. Figure 11.2 shows the aspects of the three geometries: Shell, Dusty and Cloudy. The Shell geometry consists of stars embedded in a cloud of dust. The Dusty geometry mixes stars and dust together in the whole space. Finally, the Cloudy geometry is a cloud of dust, embedded in a large volume of stars. For each of these geometries, we can choose between an homogeneous repartition of dust, or a clumpy one, which leads to six possible choices;
- star formation type: for this parameter, there are two choices being the opposite extremes of star formation scenarios: either a burst or a continuous star formation. In the first case, all stars are formed at the same time according to a stellar mass, while in the second case, we define a star formation rate along with an age.

The four other parameters have continuous sampling, to cover a large range of values. The sampling is done in log space, in order to get the best grid possible. First, the stellar parameters are used with the PEGASE.2 tool (Fioc & Rocca-Volmerange 1997, 1999):

- stellar age: it is simply the age of stars included in the grid. It ranges from 1 Myr to 12.4 Gyr;
- star formation rate: as mentioned earlier, this parameter depends on the star formation type chosen. In the case of a burst formation, the values range from 10^6 to 10^{13} $M_\odot$. If it is a continuous formation, the values range from 5×10^{-5} to 5×10^2 $M_\odot$ yr^{-1} .
- metallicity: the stellar metallicity also affects the final spectrum. It ranges from 0.0001 to 0.1;

[2]It should be noted that studies following the work of WD01 showed that the LMC and SMC-type dust did not fit the dust emission in these galaxies.

Figure 11.2: 3D representations of the geometries used in DIRTYGrid. *Left to right:* Shell has a core of stars surrounded by dust, Dusty is a mixture of stars and dust, Cloudy has a core of dust surrounded by stars.

Finally, there is a last free parameter in the DIRTYGrid:

- optical depth: this parameter, τ_V, translates the amount of dust, and ranges from 0.1 to 10.

Outputs

The final output of the DIRTYGrid is a spectrum, for each parameter set detailed above. This spectrum has been integrated in a large number of photometric bands (e.g. GALEX, *Spitzer*, *Herschel*, ...) and these synthetic SEDs are the product I am using for this study. Figure 11.3 shows examples of spectra displaying variations in each parameter space. These spectra are integrated in photometric bands. The final grid eventually provides more than 6 millions models. There are two kinds of outputs available: a library of spectra, and a bigger library of SED points. The different size of the libraries comes from speed-up tricks implemented by Law et al. *(in prep.)* for the calculations.

11.2 Public distribution

I started an extensive work to enhance and publicly distribute the DIRTYGrid, with a series of codes in Python, allowing easy access to the data. I describe here a few keys points written to this day. Since it is a complete dust RT work, it would be useful to a lot of other studies. There are two types of objects accessible in the DIRTYGrid: the full spectra and the integrated SEDs. The distribution offers the possibility of easily accessing these objects and saving them in a variable. They can be retrieved in many ways. The users can use a given set of parameters they wish to study. For experts, the ID tag of a spectrum or the location indices of an SED can also call the object. The saved points can then be plotted.

A major point is to be able to add new photometric points. As explained earlier, the DIRTYGrid uses a lesser number of spectra, integrate them in photometric bands and interpolate these points to create all the SEDs. However, I found it useful to offer the possibility for users to do so in the photometric bands of their choice. Routines to easily launch these processes, with a transmission curve as input, should greatly improve the DIRTYGrid flexibility.

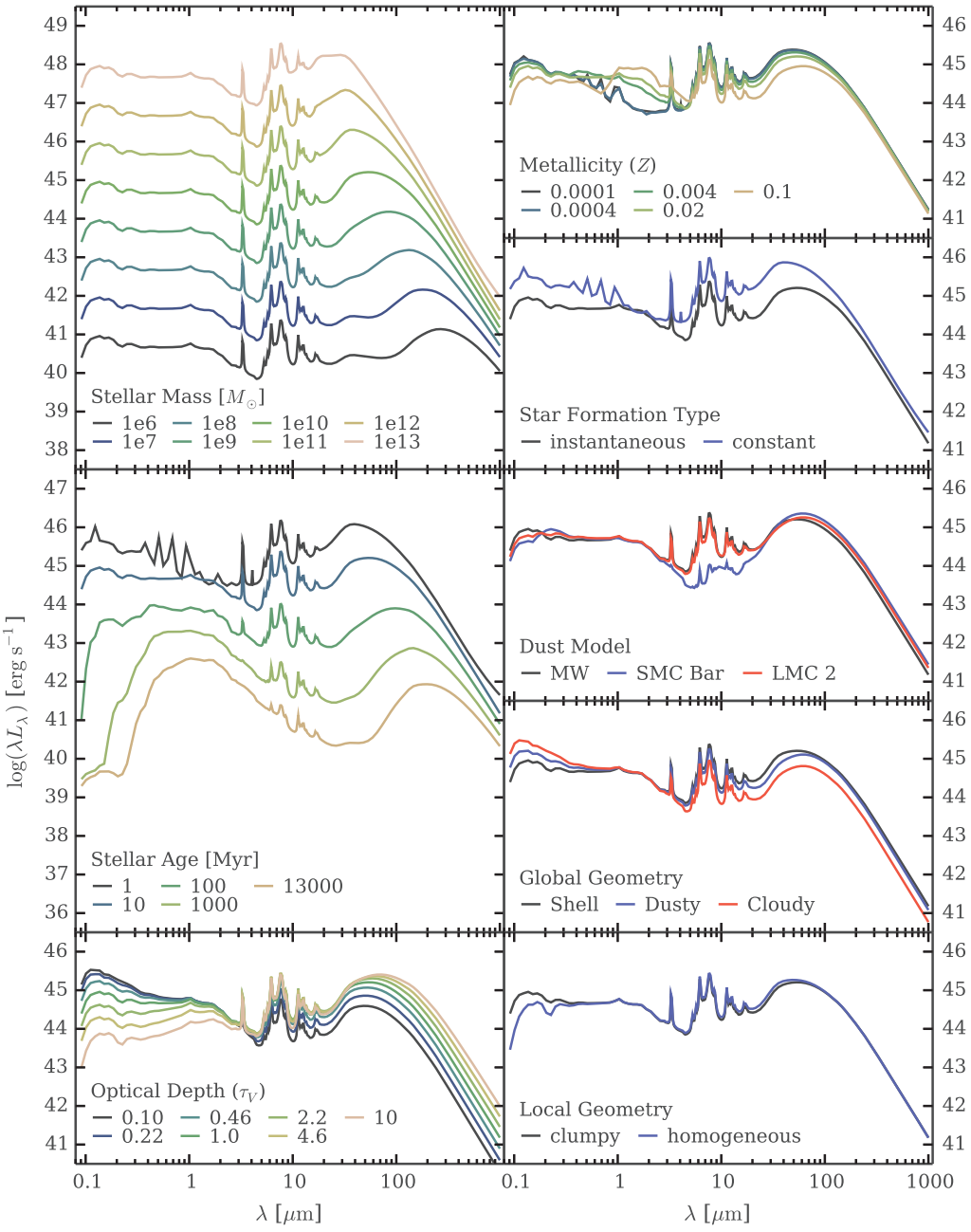

Figure 11.3: A few spectra from DIRTY, representing the variations in each parameter space.

Figure 11.4 shows a sketch of the newly implemented and publicly available tools for the DIRTYGrid.

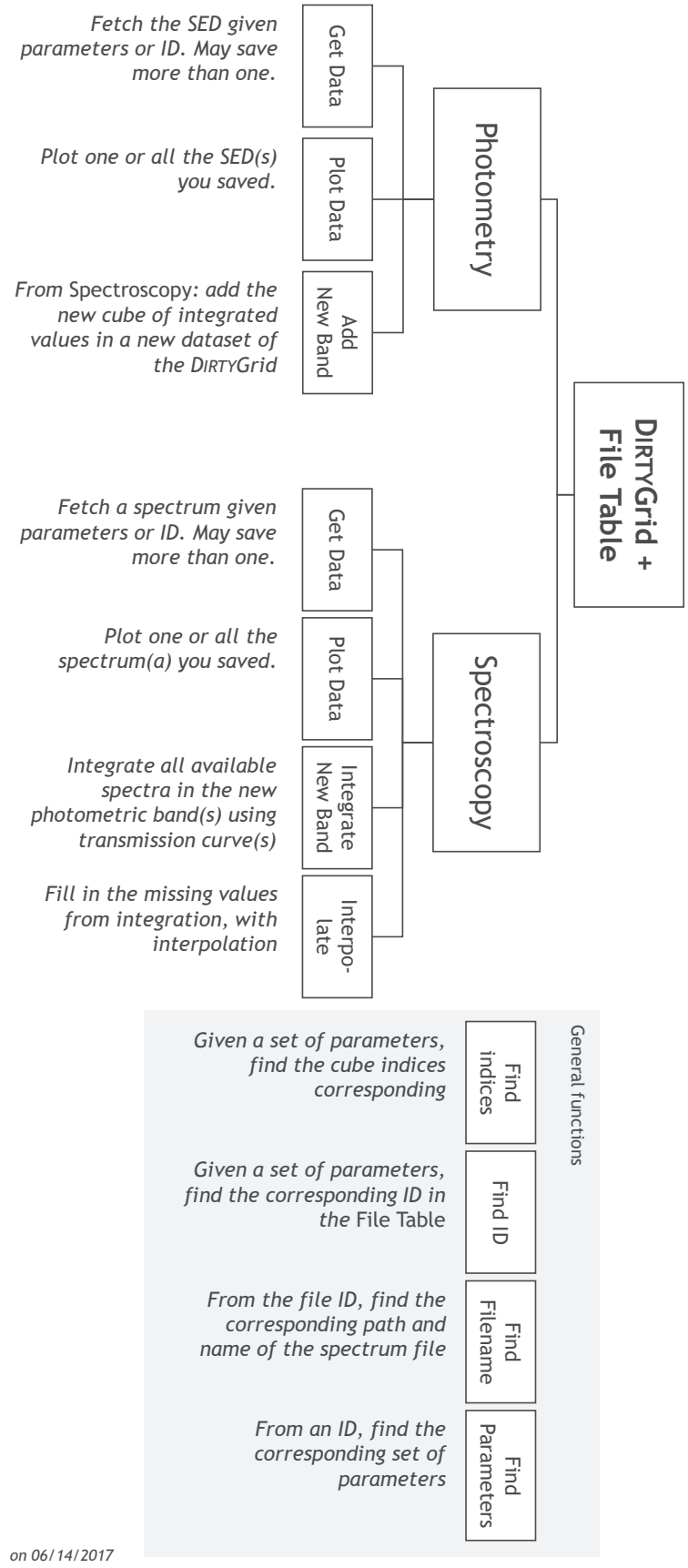

Figure 11.4: Diagram of the public distribution for DIRTYGrid, presenting the main functions implemented so far. It is split into two classes, using the photometry (SEDs) or spectroscopy (full spectra).

12 Methodology

The goal of this study is to use dust emission spectra from the DIRTYGrid as if they were observations, and fit them with the dust models commonly used in nearby galaxies dust fitting studies. RT calculations take into account source and sink terms to determine the local ISRF at each position, direction and wavelength of a grid for a given distribution of stars and dust. In doing so, hardness and intensity of the ISRF vary with the position, and the resulting dust emission spectrum is affected, being more realistic. In full dust models, to take into account the multiplicity of dust heating sources, the emission spectrum is created as a combination of spectra at different temperatures with multiple ISRFs (the ISRFs have the same shape, or hardness, but varying intensities). I want to assess the systematic differences due to the assumptions in the empirical mixing approaches that we use in most dust emission fitting studies of nearby galaxies.

12.1 The fitted: SEDs from the DIRTYGrid

I use dust emission spectra created from RT calculations as the fitted data, as if they were observations. Accounting for emission and absorption sources, and a 3D geometry, these spectra are approaching the reality of nearby galaxies measurements.

The DIRTYGrid (Chapter 11) gives us SEDs determined from the integration of the spectra created by the RT routine. The SEDs are integrated using the transmission curves from instruments. As shown in Figure 12.1, there are initially 25 photometric bands available, covering the wavelength range from the UV (starting at 0.0912 μm) to the far-IR (FIR; 500 μm). In this work, I use 10 photometric bands covering the IR emission of dust: 3.6, 4.5, 5.8, 8.0, 24, 70, and 160 μm from the instruments onboard *Spitzer* (Werner et al. 2004), and 250, 350, and 500 μm from *Herschel* (Pilbratt et al. 2010). The 10 photometric points I use are shown within the light-blue shaded area in Figure 12.1. The corresponding wavelength range in the Draine & Li (2007) model is highlighted on the left part of the figure.

I summarize the DIRTYGrid parameter in Table **??**. More details were given in Section 11.1. In the Table, I underline the type of SEDs I chose for the main part of the results: MW-type dust, in a clumpy geometry, with a continuous star formation. The other parameters are used in the entirety.

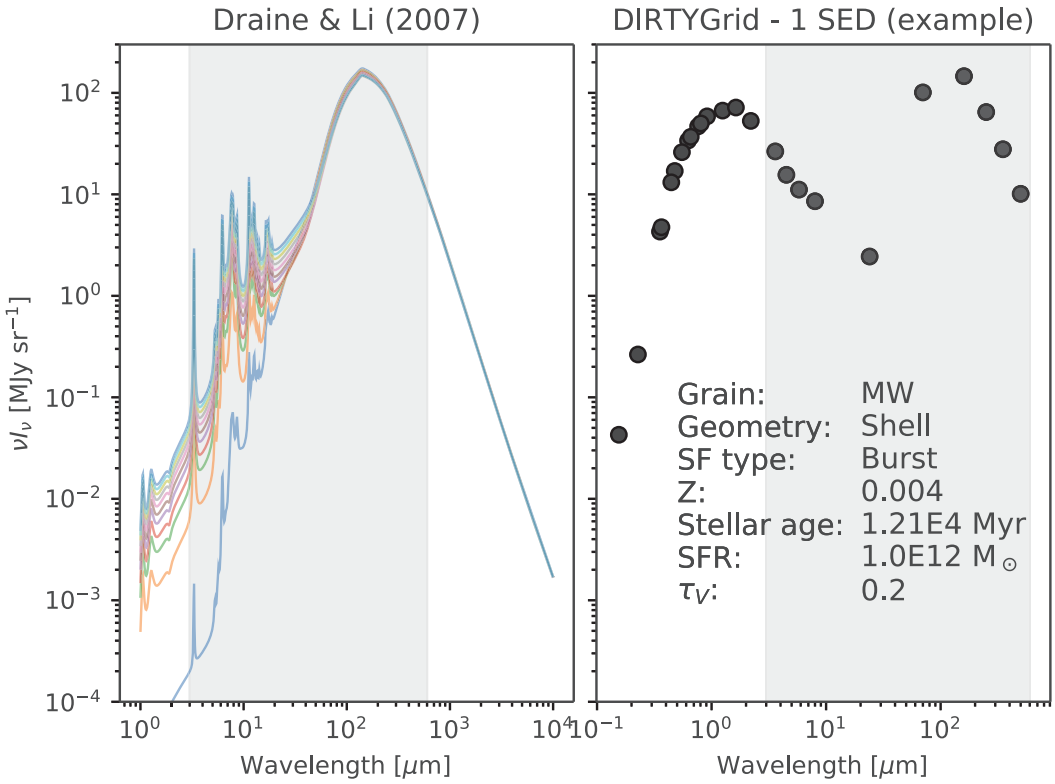

Figure 12.1: *Left:* A few spectra from the Draine & Li (2007) model, with increasing $q_{\rm PAH}$. *Right:* One SED of the DIRTYGrid for one set of parameters. In this study, I fit each SED in the DIRTYGrid with the DL07 model.

Parameter	Range		Number of values
Grain type	MW, LMC, SMC		3
Geometry	Cloudy, Dusty, Shell		3
Clumpiness	Homogeneous, Clumpy		2
Metallicity	[0.0001; 0.1]		5
Stellar age	[1.0; 1.21 10^4] Myr		50
τ_V	[0.1; 10]		25
Star formation type	Burst	Continuous	2
Star formation rate	[1.0 10^6; 1.0 10^{13}] M$_\odot$	[5.0 10^{-5}; 5.0 10^2] M$_\odot$ yr^{-1}	29

Table 12.1: Summary of the DIRTYGrid parameters.

12.2 The fitter: full dust model

I briefly remind here the contents of the dust models I use. For a more complete description I refer the reader to Section 2.6.

12.2.1 Draine & Li (2007)

Since I want to investigate the effects of RT, I use the same dust model to fit the data, that is used in the DIRTYGrid: the Draine & Li (2007) dust model.

The heating environment used in DL07 is described by a power-law to combine dust elements heated at various temperatures, and adds a single-temperature heated dust element to the mixture, corresponding to the diffuse ISM. The relative weight of each term is set by a free parameter γ:

$$\frac{\mathrm{d}M_{\mathrm{dust}}}{\mathrm{d}U} = (1-\gamma)\,M_{\mathrm{dust}}\,\delta(U-U_{\mathrm{min}}) + \gamma M_{\mathrm{dust}}\,\frac{\beta-1}{U_{\mathrm{min}}^{1-\beta}-U_{\mathrm{max}}^{1-\beta}}U^{-\beta} \tag{12.1}$$

The idea of a power-law used to mix dust comes from the work of Dale et al. (2001). They showed that this description, with a coefficient varying between 1 and 3, would reproduce well the RT effects in two extreme cases: a dense medium slab or a diffuse uniform medium. Although efficient in reproducing the shape of the IR SEDs of star-forming galaxies, it is an empirical mixing law that may not be a general solution. Comparing this approach, and ISRFs calculated locally will give us insights about its accuracy in more general situations.

The Draine & Li (2007) model is described by two grain populations: silicates and carbonaceous grains. The carbonaceous component has two types of grains: graphite, rather large, and smaller particles described by poly-cyclic aromatic hydrocarbons (Leger & Puget 1984; Allamandola et al. 1985). In this study, this model has a total of 5 free parameters: $\mathrm{U}_{\mathrm{min}}$ is the minimal ISRF used in the mixture; β is the power-law coefficient for the integration over the range of ISRFs; q_{PAH} is the fraction of small PAH particles; γ, the relative weight of ISRF; Σ_{dust}, the dust surface density.

An additional parameter is used to model the stellar emission, as often done in dust emission modeling in the NIR. I use a blackbody at 5 000 K to account for stellar emission, that I scale through a free parameter Ω^*.

12.2.2 THEMIS

The DIRTYGrid emission spectra are built using the model from Draine & Li (2007), so I started by fitting these with the same model to investigate the effects of RT only. However, I also investigate the response of other dust models to fitting the DIRTYGrid SEDs. The idea is to observe the discrepancies that arise when observations are fit with a dust model that is not the same description that the dust composition creating the dust emission observations. In this work, I thus also use THEMIS (Jones et al. 2013; Köhler et al. 2014; Ysard et al. 2015). THEMIS is used with the DustEM tool, which can output a dust emission spectrum. It uses the local ISRF described by Mathis et al. (1983) to heat dust. I make use of this tool, and compute a dust emission spectra library by combining several outputs using ISRFs of various intensities, to take into account the mixing of temperature. This approach is described as a multi-U environment in Chastenet et al. (2017) (see Part II). In this case, the model has 5 free parameters: α_{U}, is the power-law coefficient for the integration over the range of ISRFs; $\mathrm{U}_{\mathrm{min}}$, is the minimal ISRF used in the mixture; Y^{i} are the grain abundance factors in terms of $M_{\mathrm{i}}/\mathrm{M}_{\mathrm{H}}$,

with i = {aSilM5, lCM20, sCM20}. In this case as well, I add the Ω^* parameter that scales a blackbody at 5 000 K to take into account the stellar emission.

12.2.3 Model Calibration

Following the idea introduced in Gordon et al. (2014) and Chastenet et al. (2017), I re-calibrate the dust model onto the same galactic SED. Although they both manage to suitably fit the MW IR emission, I want to enforce that they strictly share the same gas-to-dust ratio (GDR), based on galactic observations, as it is an independent measurement. Doing so, I hope to minimize the inherent disparities between the models assumptions. I fit the models presented in Section 12.2 to the high galactic latitude SED described in Compiègne et al. (2011). In each case, this fit gives us a new set of dust abundances, scaling the models up or down. From these new abundances, I determine the corresponding GDR for each model. I finally find the factor that scales this updated GDR to 150. This value is based on the work of Jenkins (2009) and its depletion measurements. Because both models do not use the same assumption in terms of gas column density, used to set the GDR, I find important to "reset" this value to a common ground.

12.3 Fitting technique

I use the DIRTYGrid fluxes as data, that I fit with the DL07 model presented in the previous Section. For each DIRTYGrid SED, I want to find the best fit with a full dust multi-U model and check that the parameters recovered from the fit are consistent with the ones used to generate the SEDs.

I run the fits with the DustBFF tool (Gordon et al. 2014), presented in this thesis (Part II). Although this work does not use observations *per se*, I use the DIRTYGrid SEDs as such. In practice, these SEDs are integrated in photometric bands, using transmission curves from multiple instruments, and their associated uncertainties. The DustBFF tool uses correlation matrices to propagate uncertainties throughout the fit. In order to resemble a study that would involve observations, I use the errors of the instruments used to create the SEDs. I therefore use uncertainties from IRAC and MIPS from *Spitzer* , and SPIRE from *Herschel* . The values used for all bands except 160 μm can be found in Chastenet et al. (2017) (or Part II). For the MIPS 160 μm band, I use a 12% uncertainty for repeatability (as a diagonal term), and 2 and 5% uncertainties for correlated uncertainties with the MIPS 24 and MIPS 70 μm bands, respectively (for anti-diagonal terms)[1].

All fits are done in MJy/sr.

[1]The description of correlation matrices can be found in Gordon et al. (2014) and Chastenet et al. (2017).

13 Fitting results

13.1 Using an identical model

First, I investigate the results of fits where the dust composition is the same in the model and the data, i.e. I use the DL07 model to fit the DIRTYGrid fluxes. I run the fits for the three different geometries of DIRTYGrid: Shell, Cloudy and Dusty, with a clumpy distribution of dust, in a continuous star formation scenario. I restrict this study to a single grain type I choose in the DIRTYGrid is MW-type dust, as it seems to be the only one needed in studies that fit the IR emission of galaxies (Draine et al. 2007), including the Magellanic Clouds (Sandstrom et al. 2010). The goal is to check the fit quality, but also look at dust masses and $q_{\rm PAH}$ fraction in the DIRTYGrid, since we know their values, and verify if they are correctly recovered with the fit.

13.1.1 Quality of the fits

I investigate the fits quality using the best fits, or maximum likelihood. Figure 13.1 shows the fractional residuals corresponding to these fits. We notice that all geometries follow the same trend in terms of fit quality. None seem to be a significantly better fit than the others. However, we see that the DL07 model constantly overestimates the fluxes at long wavelengths, at $\lambda \geq 160$ μm. This shows that the shapes of the DIRTYGrid SEDs are not well reproduced with the DL07 model. The fact that the overestimation occurs at $\lambda \geq 160$ μm may be a combination of two problems. The first problem might simply come from the fact that the shape of the IR peak and sub-millimeter slope does not to fit such data. It is possible that the RT calculation for the DIRTYGrid SEDs impacts the FIR slope and/or the IR peak in a way that the DL07 model cannot reproduce. The second issue is that the uncertainties at long wavelengths are greater than at short wavelengths: the uncertainties in the IRAC and MIPS24 bands ($\sim 4\%$) are lower than in the SPIRE bands ($\sim 10\%$). It forces the fit to choose a model that better reproduces the data at $\lambda \leq 160$ μm. But it also means that, in order to appropriately recreate the data in the IRAC and MIPS bands, the model is not adapted for longer wavelengths. After a test-run, it turns out the quality of the fits is not really improved if I allow all bands to vary within the same uncertainties.

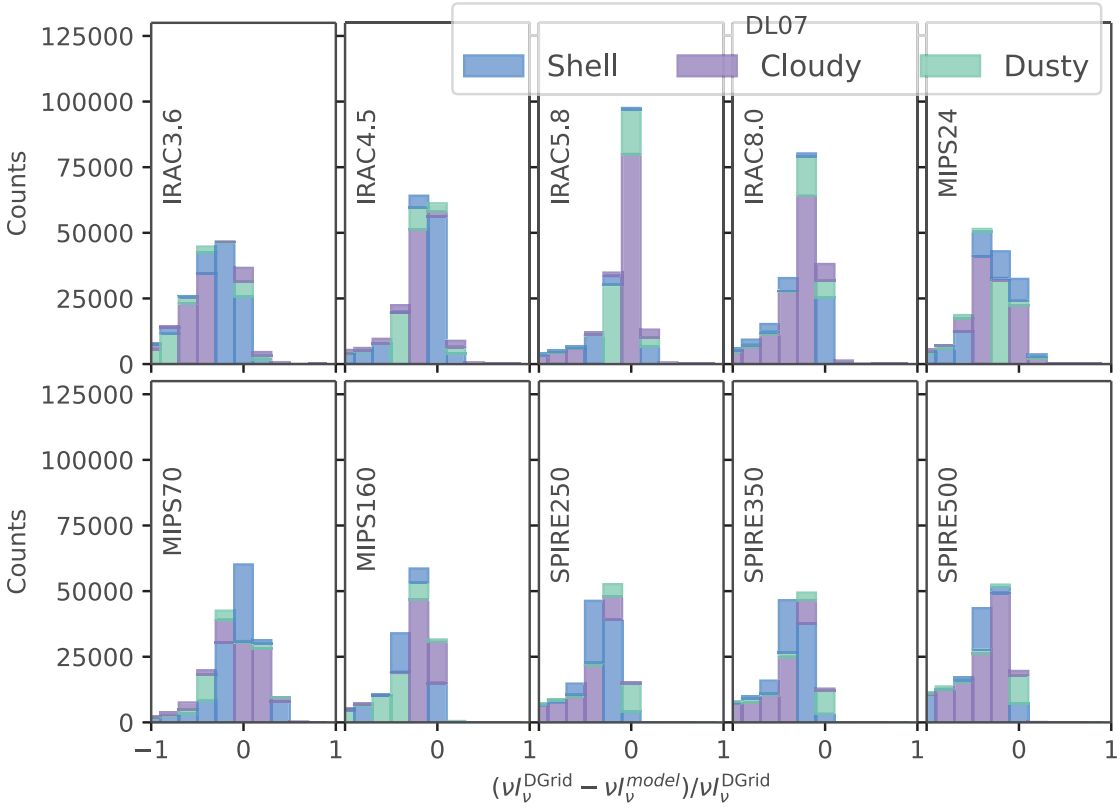

Figure 13.1: Fitting residuals using the DL07 model for the three geometries: Shell (blue), Cloudy (purple) and Dusty (green). All situations follow the same trend in terms of fits quality. A poor recovery of the data can be noticed at long wavelengths.

13.1.2 Recovering dust masses

The optical depth is known in the DIRTYGrid. We can translate this parameter as a dust mass, and then compare the value in the DIRTYGrid to that obtained by the best fit of the DL07 model. Figure 13.2 shows how the recovered $M_{\rm dust}$ scales with that in the DIRTYGrid for each fit, and shows the fractional residuals for these dust masses. On the top panel, I show 2D histograms of the mass in the DIRTYGrid, *versus* the mass found by the fit. If it manages to recover the dust mass, the densest pixels should be aligned on the $x = y$ dashed line. Globally, the results demonstrate positively that using a simple approach for the dust heating environment remains a reasonable assumption. The worst case in Figure 13.2 underestimates dust masses by a factor lower than 2.

The bottom row shows the fractional residuals of dust masses. We can immediately see that the results depend on the geometry. The Dusty geometry, in which stars and dust are well mixed together, shows the best agreement between the DIRTYGrid dust masses and those from the fits (first column in Figure 13.2). The maximum of the residuals is centered on 0, indicating a significant fraction of well-fit masses. But they also show large wings: about 14% of the fits overestimate the DIRTYGrid masses by half or more, and about 12% underestimate them by half or more. The Cloudy geometry (corresponding to a cloud of dust in a shell of stars; second column in Figure 13.2) does not show satisfying results. In this case, the model clearly underestimates the dust mass. About 45% of the DIRTYGrid dust masses are underestimated by the DL07, by half or more, and 75% are underestimated by more than 30%. The corresponding 2D histogram shows than the DL07 model in this geometry constantly underestimates the DIRTYGrid dust masses. The Shell geometry (a clump of stars within a shell of dust; third column in Figure 13.2) seems to follow the trend of the Dusty geometry, only slightly shifted to negative values: 45% of the fits overestimate the dust masses by less than half. However, a significant fraction (30%) underestimate the dust masses.

Since the input dust masses are identical in all geometries, it means that RT effects do have an impact on dust mass estimation. Even though the fit quality is similar in each case, the dust parameters corresponding to the best fits are not. It appears that the parameters used to fit the Dusty geometry are closer to the DIRTYGrid dust masses, without improving the fit itself.

13.1.3 Finding the PAH Fraction

The DL07 model is also interesting as it allows the PAH fraction to vary. The DIRTYGrid model is built assuming a single value of $\sim 4.8\%$ for the PAH fraction. It is interesting to know if the DL07 model fits can retrieve this reference value, in the different situations we have.

Figure 13.3 shows the recovered $q_{\rm PAH}$ for the three geometries[1]. It appears that none of them allows for a correct estimation of the $q_{\rm PAH}$ value. In all cases, the models overestimate this parameter significantly, by choosing the highest value possible ($\sim 7.4\%$) in the DL07 model. This is often linked with a low Ω^* value. This is interesting as it means the fit chooses to use the $q_{\rm PAH}$ parameter to adjust the IRAC bands more than the stellar density parameter. The two parameters however do not impact the SED the same way. The Ω^* parameter mostly scales the data points at 3.6, 4.5 and 5.8 μm up and down. The $q_{\rm PAH}$ parameter helps adjusting these points, but also affects the slope between 8.0 and 24 μm, without changing too much the position and intensity of the IR peak. It is surprising to compare the reasonable quality of the fits in the IRAC bands (Figure 13.1) and the poor recovery of the $q_{\rm PAH}$ parameter. Nonetheless,

[1] At the end of writing this thesis, it appeared that an error on the $q_{\rm PAH}$ results was leading to a wrong conclusion about the quality of this parameter recovery. This point will be checked and corrected before submission of the paper.

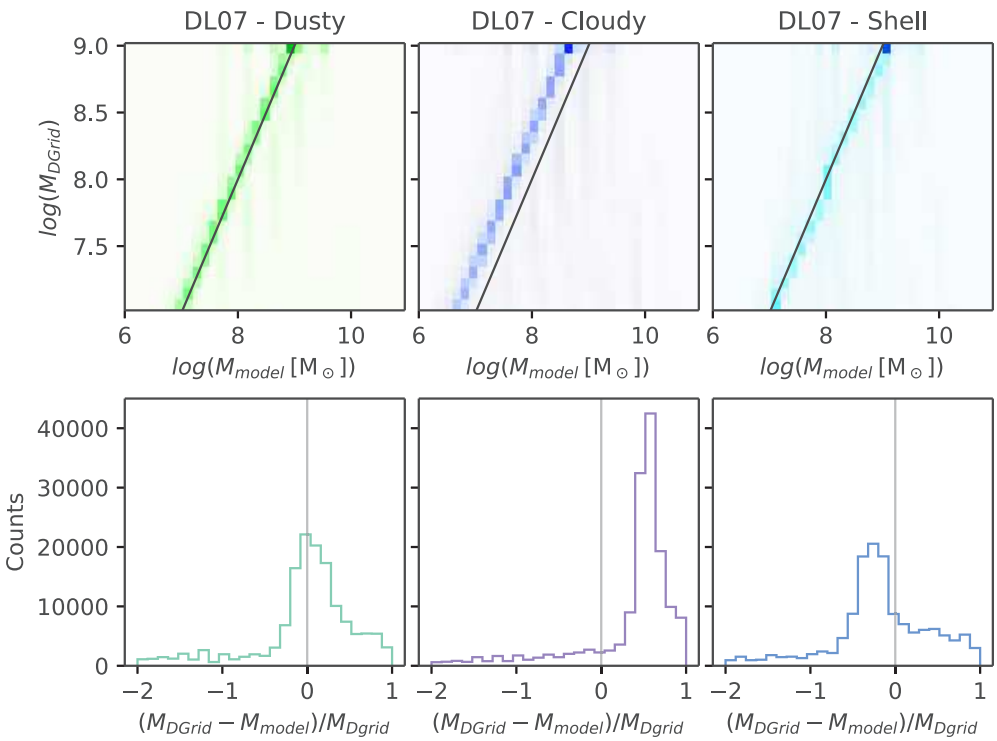

Figure 13.2: *Top row:* 2D histograms of the total dust masses in the DIRTYGrid and the results of these fits for the three geometries. *Bottom row:* Histograms of the dust mass residuals for corresponding geometries. The Dusty case shows a good estimation of dust masses while the Cloudy situation is constantly overestimated.

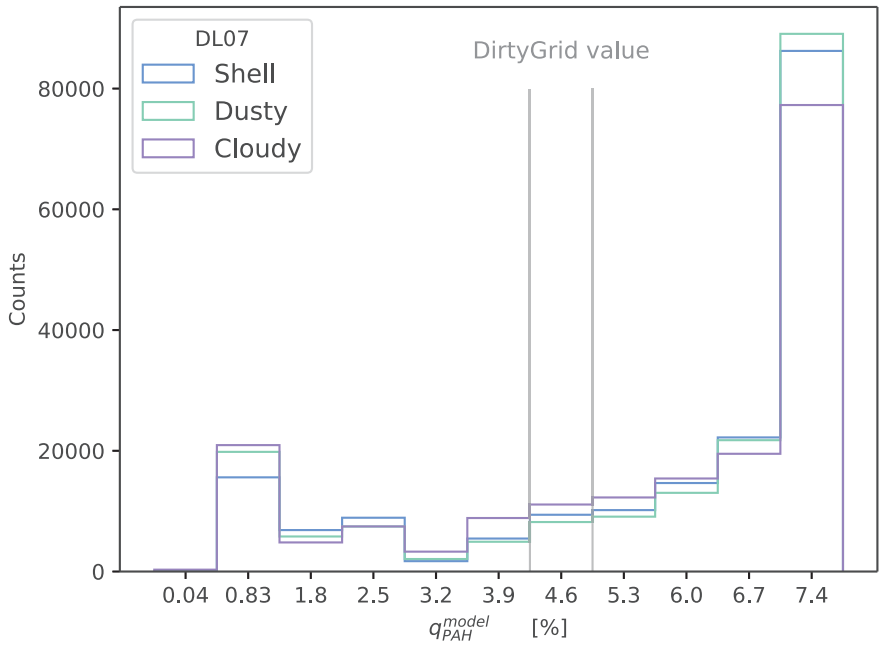

Figure 13.3: Recovered values of the q_{PAH} parameter from DL07 fits, in the three geometries of the DIRTYGrid. The q_{PAH} value in the DIRTYGrid is in the interval marked with grey lines. It is never found by the fits, which mostly choose the maximum q_{PAH} value.

this result indicates that the parameterization of the DL07 model prevents a correct estimation of the PAH fraction, with this set of parameters. It may be due to a strong degeneracy with Ω^* or U_{min}, which both affect this part of the SED as well.

13.1.4 Investigating the parameter ranges

We saw in Figure 13.3 that the fits choose the maximum value in the q_{PAH} sample to fit the DIRTYGrid SEDs. In Figure 13.2, I showed that the dust mass residuals have large wings showing a significant amount of over-/underestimated masses. In order to understand the impact of the sampling boundaries, I looked at the dust masses from the DL07 fit when I take out the fits for which the best parameter is one of the sample limits. For example, the q_{PAH} parameter ranges from 0.04% to 7.4%; here, I discard every fits that has one of these extreme values as best q_{PAH} parameter, and look at the dust mass residuals of only the fits with values in between. This is justified as, if the fit chooses one extreme value, it might imply that a lower/greater one might have been better.

In Figure 13.4 the dashed lines show the dust masses for all the DL07 model fits (same results as Figure 13.2), and the solid lines show the results without the fits whose best parameters include boundary values, as described above. Because it takes out a number of points, I normalized all histograms to have a readable histogram. We see that the residuals are now more peaked. The maximum are not shifted, but the number of over-/underestimated greatly decreases. This means a significant portion of the dust masses that are not well-fitted come from the limits of the sampling space. For all geometries, the same behaviour is observed: the residuals appear more peaked.

After further investigation, it turns out only the U_{min} parameter is responsible for this change. If I leave out the fits where the best fit is the lowest value available, then the underestimated masses (with respect to the peak for each geometry) is gone. If I leave out the fits with maximum

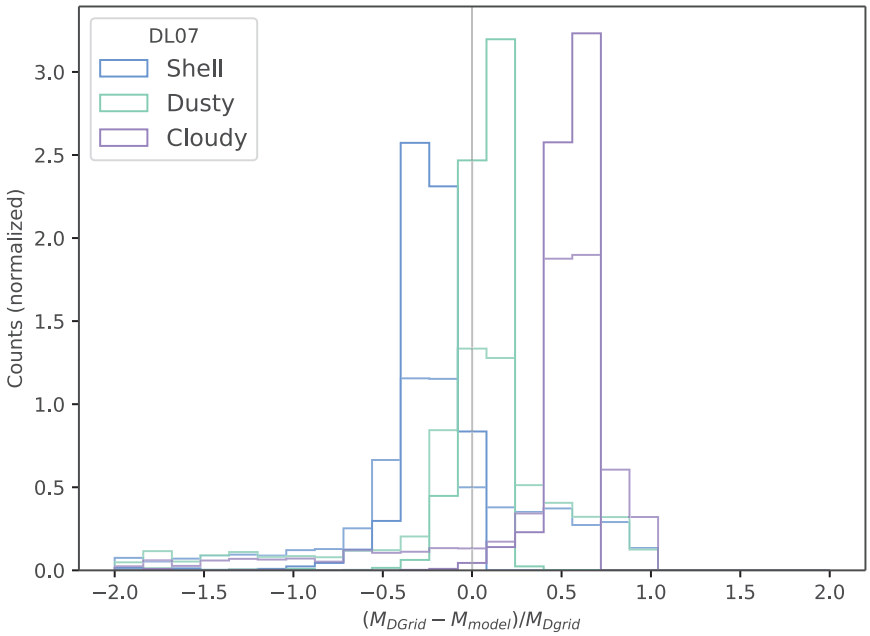

Figure 13.4: Histograms of the dust masses for the three geometries. The dash lines show the results for the full sample, and the solid lines, results when I do not select the edge values of $U_{\rm min}$ parameter. The histograms were normalized.

$U_{\rm min}$ value, the same thing happens for the overestimated masses. It means the limits of the $U_{\rm min}$ sample, from 0.1 $U_{\odot}$ to 50 $U_{\odot}$, should be extended. However, a possible degeneracy with other parameters is likely. Adjusting the $U_{\rm min}$ value changes the shape of the dust emission spectrum, and shifts the IR peak to lower wavelengths, are $U_{\rm min}$ increases. Moreover, an obvious difference depending on geometry is visible: RT effects clearly play a role in the recovery of dust masses.

13.2 Using a different dust composition

Since the fits quality is not perfect, and in studies of nearby galaxies we do not know the dust composition, we can test the impact of using another model to fit the DIRTYGrid SEDs. I test the impact of fitting the DIRTYGrid SEDs, built with the DL07-type dust, with THEMIS (Jones et al. 2013; Köhler et al. 2014; Ysard et al. 2015; Jones et al. 2017). I choose THEMIS because it has been shown that it can better reproduce IR SEDs shapes in the Magellanic Clouds (Chastenet et al. 2017), and that the inferred dust composition implies an evolution of dust composition. One can then wonder whether we are interpreting effects of RT as changes of composition.

Figure 13.5 shows fit residuals using THEMIS, in the Dusty, Shell and Cloudy geometries. Surprisingly, we see better fits at long wavelengths than previously. They appear more centered on 0, with shorter wings. It indicates that having the same dust composition is not necessarily synonym of a good fit. In this case, RT effects are compensated by a better FIR slope in the dust model. The better fits at long wavelengths likely lie in the spectral index β. In THEMIS, the FIR slope of aSilM5 and lCM20 grains (silicates and carbonaceous, respectively) are quite different, while the FIR slope of the two grain populations in the DL07 model are more similar. In THEMIS, an increased flexibility in the FIR range is probably the reason of a better adjustment. However, the fit quality is significantly worse at short wavelengths, especially at 3.6 and 4.5 μm.

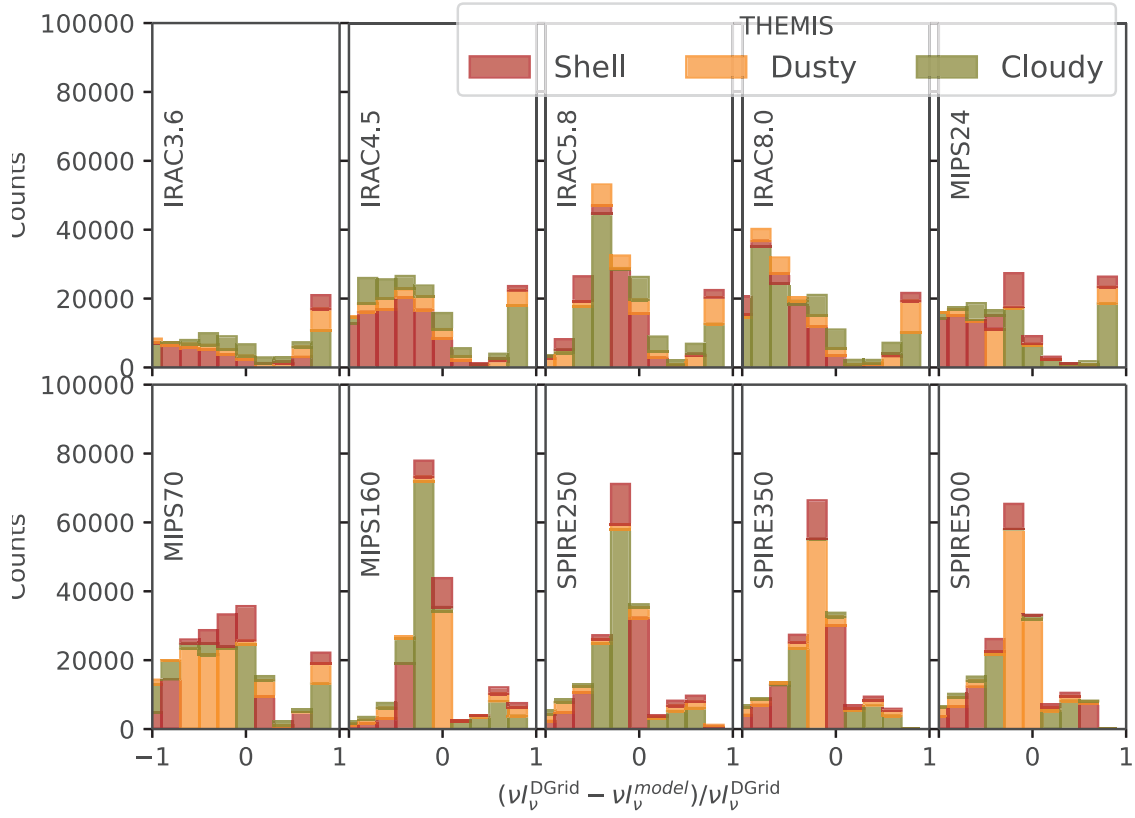

Figure 13.5: Fitting residuals using THEMIS for the three geometries: Shell (red), Cloudy (green) and Dusty (orange).

None of the bands at $\lambda \leq 70$ μm shows a reasonable fit. Although THEMIS has an independent small grain component, its description does not help to reproduce the data. It may come from the very particular q_{PAH} parameter, unique to the DL07 model. This would mean the variations allowed by a higher U_{min} or a simple scaling of the small grain abundance is not enough. The SED shape between 8.0 and 70 μm appears to be critical in fitting the dust emission. The parameters in THEMIS do not allow such variations. A varying size distribution of the small grains would be required to be able to change said slope, but is beyond the scope of this paper.

The dust masses, shown in Figure 13.6, recovered by THEMIS are in general less in agreement with the DIRTYGrid than the DL07 model. The Dusty geometry, which showed the best results in Figure 13.2, only shows 30% good masses within a 15% error. About 50% of the fits either over- or underestimate the dust masses by half or more. The Shell geometry show significant difference when fit with THEMIS or the DL07 model. In the latter case, we saw it recovered dust masses within reasonable errors. If I use THEMIS, about 40% of the fits underestimate the masses by half or more.

13.3 More DIRTYGrid variations

The results exposed in Sections 13.1 and 13.2 are the first results from this study. There are however, other leads to investigate. The fits run up to this section take a long time (about one week per geometry). I therefore chose a single geometry to get preliminary results on the following questions.

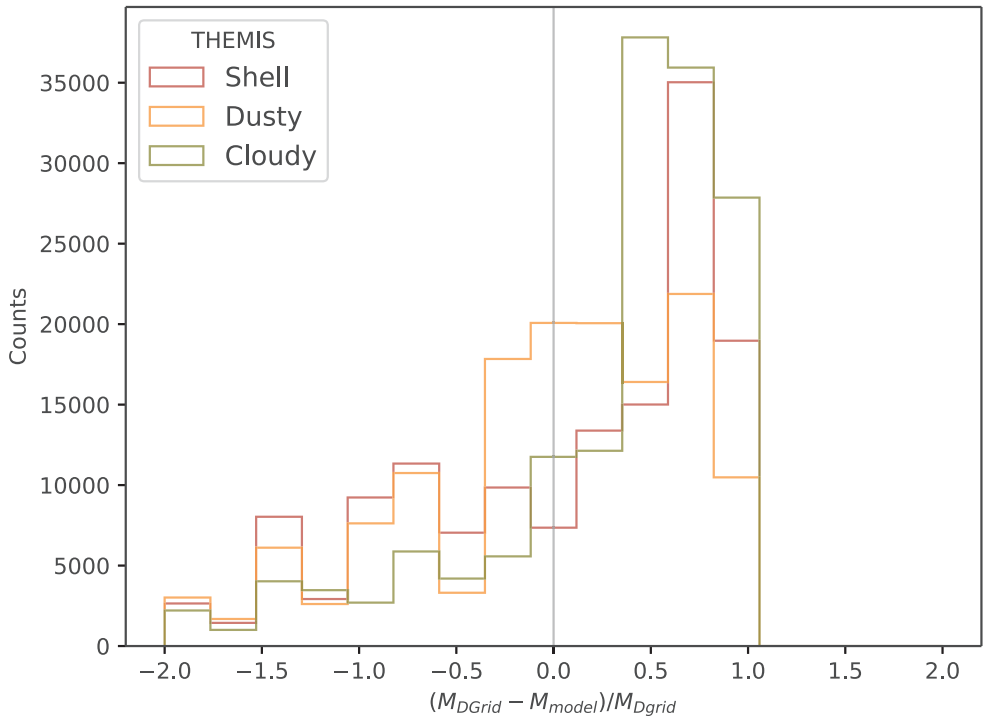

Figure 13.6: Fractional residuals for dust masses using THEMIS. Color code is the same than Figure 13.5.

13.3.1 Continuous vs Burst Star formation

I run a fit to compare the differences between a continuous and a burst star formation. In the previous sections, all fits are done with a continuous star formation. Here, I fit a Dusty geometry only, as it showed the best results in terms of dust masses in the previous section.

In terms of fits quality, there is no major difference between the two situations. Only the IRAC4.5 and IRAC5.8 bands are better fit in a continuous star formation situation. The other bands show very similar results.

In terms of dust masses, the instantaneous-type formation follows almost exactly the results of the constant formation. A larger portion of the data point are being underestimated in the former case, by $50 - 100\%$.

13.3.2 Clumpy vs Homogeneous dust distribution

I also investigate the differences between a clumpy and a homogeneous distributions of dust in the Dusty geometry.

Once again, there is no significant difference in terms of fits quality, between the two distributions. Their residuals both follow the same trend: they still exhibit negative wings at long wavelengths, and reasonable fits at shorter wavelengths. This result is quite in opposition with the study of Witt & Gordon (2000), who showed a clumpy medium was more adequate to reproduce dust extinction, using radiative transfer as well.

The dust mass distributions in both situations are very similar. Contrary to the difference seen in Section 13.3.1, the residuals overlap almost perfectly, and the homogeneous geometry does not show any peculiar result, compared to the Clumpy one.

In both cases, there are few differences between a Burst or Continuous star formation, or between a Clumpy or Homogeneous dust distribution. That indicates that dust emission is likely a poor probe to discriminate between these situation in real observations. On the bright side, it means that dust emission models do not necessarily need to take these parameters into account, as they do not affect much the resulting properties.

14

Dust RT: conclusions and perspectives

The goal of this study was to investigate the effects due to to radiative transfer in dust emission fitting. I used an RT-based library of dust emission SEDs: the DIRTYGrid. The SEDs were created by the integration of dust emission spectra in the photometric bands of the Spitzer IRAC and MIPS instruments, and the Herschel SPIRE instrument. The RT calculations are made in various geometries of stars and dust, representative of the multiple possibilities that can be found in nearby galaxies. These SEDs were fit with the common dust models used in the literature: the Draine & Li (2007) model and THEMIS (Jones et al. 2013). These models use a description of the dust heating environment simpler than that from the RT calculations.

Using the same dust composition on both sides (RT-based and common model), I have still identified some discrepancies between the two approaches. Namely, the shape of the dust SED in the FIR fails at being adjusted by the classical use of dust models like Draine & Li (2007). The fluxes in the DIRTYGrid are underestimated by the DL07 model. The dust masses recovered are geometry-dependent. The quality of the results varies from a geometry to the other. This is indicative that the relative distribution of stars and dust is important in dust emission fitting. It is an aspect that simple descriptions of the ISRF fail at reproducing. In all cases, the dust masses are over- or underestimated by less than a factor 2, which is still a good sign, despite the visible variations. Unique to the DL07 model, the $q_{\rm PAH}$ parameter is never properly recovered by the fits. It is constantly overestimated. The reason of the peculiar behavior still remains unknown, but a lack, or at least, a shortcoming of a parameter definition in the NIR is likely, additionally to the RT effects.

I have shown that using a different dust composition may lead to better results in some part of the SED. For instance, THEMIS reproduces better the FIR SED points. However, it fails at adjusting the fluxes in the NIR and MIR. The same conclusion stands for the dust masses using this model. Contrary to the DL07 model, no geometry seems to present a good recovery of the dust masses that were put in the DIRTYGrid.

The differences that stand out for each model are interesting as they show their respective assets and shortcomings. In all cases, an accurate adjustment of all parameters at once seems impossible. However, investigation leads will stem from these results. For instance, a free size distribution may strongly improve the quality of the fits. The relative mass distribution in a dust model (more weight in the small carbonaceous or the large ones) is also an interesting path to

study. More work following this one will continue to make use of the RT-based and the common dust model, to identify and correct the systematic errors due to our simplifications.

To go further, a general question we can study is the impact of the number of bands on the fits. Is this number critical to the results? Is there a minimal number of bands to recover a correct dust mass, and are there wavelengths to prefer to others? Small and large grains do not emit at the same wavelengths; silicate and large carbonaceous grains emission spectra do not have the same shape. It is thus interesting to know how our results in modeling IR emission of nearby galaxies are sensitive to the choice of wavelengths or ranges.
For example, what are the wavelengths crucial to constraint the IR peak? Works have shown that 100 μm is necessary. However, can we think that using both 70 and 160 μm could play the same role? A lot of studies focus on the FIR/sub-mm part of the dust emission spectrum. In that case, modified blackbodies are often used. Understanding which band is critical to constrain the temperature, and which is critical to the emissivity would bring a useful insights to that type of study.
We can also look closer at the sub-mm and millimeter ranges. Those are the wavelengths where cold dust emits. In a "cold" environment, dust grains form aggregates; these might be non-negligible and contribute to the dust mass budget. As shown in the first study of this thesis (Part II, Chastenet et al. 2017), the sub-mm is also the frame where a distinction can be made between silicate and carbonaceous. It has been shown that their FIR emissivity slope is not identical; at longer wavelength, the distinction could become more evident and, combined with shorter wavelengths, allow for a clear estimation of each population abundance.
The 24-70 μm (or 8-70μm) slope is also interesting as it gives clues about small grain size distribution. Constraining these wavelengths may help to constrain shorter wavelengths, but also have a consequence in our understanding of small grain processing. The project SPICA (Space Infrared telescope for Cosmology and Astrophysics) could be an excellent opportunity to gather data in this wavelength range. Its MIR instrument should provide with data between 12 and 36 μm in spectroscopy and around 34 μm in photometry. It would be an excellent candidate to help constraining the size distribution of small to large grains.

An interesting output of the DIRTYGrid is the distribution of the ISRF computed by the RT routine in each cell. This is a tremendous information to analyze. The current method to mix temperatures is based on empirical fittings and results. Looking directly at what distribution of ISRF the RT calculations determine would be a strong indicator of our accuracy. In the future, using this output can reveal more insights about the differences that may exist, for instance, between different geometries. We might expect a different ISRF distribution between the Dusty geometry, where dust and stars are completely mixed, and Cloudy, where the starlight is much less blocked by dust grains. In these various situations, the relative contributions of ISRFs of different intensities or hardness may change, and not be similar to a power-law distribution. Determining another empirical law of mixing, or validate the current one, based on RT calculations would be a tremendous step forward. A direct application to nearby galaxies would be a good confirmation (or rejection) of the model findings from RT.

PART III – TAKE AWAY

The results presented in this part are gathered in a publication that will be soon submitted. After identifying the differences between models in Part I, we wanted to investigate the biases due to the assumptions made when using a dust model, in nearby galaxies, and in particular in the recipes for mixing environment at different U. To do so, we used dust emission SEDs from radiative transfer (RT) calculations, fit with dust models used in the literature.

What did we show:

- the RT effects do have an impact on the shape of the SED even when the dust composition is the same. The dust modeling we use in nearby galaxies suffers from a "too simple" description of the ISRF, and from not taking into account the distribution of dust and stars.
- My results show biases in the dust masses recovered compared to the ones input in the synthetic data. These biases are geometry dependent and the over-/underestimations can go up to $\sim 100\%$.
- Clues of a insufficient parameterization of the MIR are visible. A parameter, the $q_{\rm PAH}$ fraction, shows no good fits, in any of the geometries.
- Using a different dust composition than that built in the grid may lead to a better fit quality, in some bands; it means the flux recovery is not a strong indicator of the accuracy of dust description.

This whole study is in a paper in preparation, and the first of a series that will use extensively the comparisons between a synthetic grid and the dust models we use to fit IR emission of nearby galaxies.

Part IV

General Conclusion & Perspectives

General conclusion

The goal of this thesis was to question the impact of the assumptions made while fitting full dust models to the IR emission of nearby galaxies. For instance, the dust composition between models changes: graphite or amorphous carbon, and silicates, presence of aromatic mantles, inclusions of metals. This is also true for the grain size distributions: one population or two, extent of the small grains. Different descriptions of the ISRF are also used: power-law mixing of radiation fields, single temperature or mixtures of environments. We can also find different values for the emissivity index β. Despite these differences, all models are designed to fit more or less the same reference: the dust constraints in the solar neighborhood (emission, extinction, and depletions). But our curiosity goes beyond our galaxy, and we are rightful to ask ourselves if using this description in other galaxies is appropriate. My thesis work has hence focused on the impact of assumptions and dust model choices on dust emission modeling in nearby galaxies.

In a first part, I analyzed the IR emission of two nearby galaxies, the Magellanic Clouds (MCs). I have adjusted their emission from 3.6 to 500 μm with different dust models: Compiègne et al. (2011), THEMIS, and Draine & Li (2007). This was done using a common fitting technique, DustBFF, in order to identify variations in the resulting parameters that would be due to the choice of the models only.
I found that THEMIS (Jones et al. 2013; Köhler et al. 2014; Ysard et al. 2015; Jones et al. 2017) reproduces the observations in the MCs better than the Compiègne et al. (2011) model. That is due to a more accurate description of the spectral index in the FIR/submillimeter regime. THEMIS was used in either a single or multiple ISRFs, to investigate the impact of the temperature mixing. I showed that using multiple ISRFs to create dust emission spectra leads to a better adjustment of the data. I derived dust properties from the fitting with THEMIS. This model is described by a population of carbonaceous and silicate grains. I showed that their relative abundance is different on average between each galaxy and the Milky-Way. Variations within each galaxy are also seen. That indicates that the dust composition is different in our Galaxy from the LMC and the SMC. Dust masses were inferred in this study as well, and are in agreement with previous studies.
I used dust properties inferred from emission fitting to create dust extinctions curves, in a few lines-of-sight in the MCs. I showed that using dust properties derived from emission only results in extinction curves that do not match the observed data. It suggests that dust emission properties are not sufficient to completely describes its composition, and that extinction also conveys crucial information. These results have been published in Chastenet et al. (2017).

Following this study, I added the Draine & Li (2007) model to the comparison. My results indicate that this model provides similar results as THEMIS. Finally, using the same data, and THEMIS, I also investigated the impact of the ISRF shape, as opposed to its intensity, on the fit quality. I showed that the preferred hardness of the radiation field is different between each galaxy.

This study highlighted the importance of the dust heating environment on derived properties. The second study presented in this thesis stemmed from this result.

In the second part of my thesis, I explored the implications of the empirical ISRF-mixing laws on dust emission fitting in nearby galaxies. To do so, I used synthetic data created from radiative transfer (RT) calculations (DIRTYGrid: Gordon et al. 2001; Misselt et al. 2001, and Law et al. *in prep.*), and fit them as if they were observations of nearby galaxies. The DIRTYGrid aims at determining the ISRF in each position within a 3D geometry of stars and dust. The dust emission spectrum is hence calculated with a more physically-determined ISRF, at each position of the cloud. I compared this realistic approach to the dust models used in nearby galaxies (multi-ISRF model). First, I used the Draine & Li (2007) model as it is the same dust composition as in the DIRTYGrid. The differences observed between the best fit parameters and the grid inputs are therefore only due to RT effects.
I showed that the relative distribution of stars and dust has an impact on the inferred dust properties, in particular on dust masses. Although this geometry effect does not affect much the quality of the fits, other parameters can be over- or underestimated depending on the situation. However, my results showed that these discrepancies do not go beyond a factor of 2. These results, presented in a paper to be submitted soon, demonstrate that the empirical mixing laws used in dust emission modeling of nearby galaxies still suffer shortcomings. Those results are the first of a series that will make more use of the RT-based calculations and dust model comparison. The advantage of this approach is that we know the reality of the data, that can be directly compared to the results of the fitting.

Those two studies show that the choices and assumptions made in dust modeling for dust emission fitting do have an impact on the inferred dust properties. The difference in dust composition from a model to another, or the chosen law to mix dust at different temperatures affect estimations of dust masses, grain sizes and relative abundances.
The framework developed in this thesis will be further used in the future. In particular, I will explore the impact of the number of photometric bands, the empirical law of ISRF-mixing, and the impact of clumpiness and star formation scenario on inferred dust properties.
This thesis has presented a direct application only in two nearby galaxies. More extensive work will be done in a large sample of galaxies at very low redshifts. I will collaborate with Drs. Karin Sandstrom and Adam Leroy on building a catalog of dust, gas and stars in galaxies at redshift $z = 0$. The vast number of observations will allow me to probe the extent of my results in various environments.

Bibliography

Allamandola, L. J., Tielens, A. G. G. M., & Barker, J. R. 1985, ApJ, 290, L25

Aniano, G., Draine, B. T., Gordon, K. D., & Sandstrom, K. 2011, PASP, 123, 1218

Asplund, M., Grevesse, N., Sauval, A. J., & Scott, P. 2009, ARA&A, 47, 481

Baes, M., Gordon, K. D., Lunttila, T., et al. 2016, A&A, 590, A55

Balog, Z., Müller, T., Nielbock, M., et al. 2013, Experimental Astronomy

Barnard, E. E. 1910, ApJ, 31

Beitia-Antero, L. & Gómez de Castro, A. I. 2017, MNRAS, 469, 2531

Bendo, G. J., Griffin, M. J., Bock, J. J., et al. 2013, MNRAS, 433, 3062

Bennett, C. L., Banday, A. J., Gorski, K. M., et al. 1996, ApJ, 464, L1

Bernard, J.-P., Reach, W. T., Paradis, D., et al. 2008, AJ, 136, 919

Bocchio, M., Jones, A. P., & Slavin, J. D. 2014, A&A, 570, A32

Bolatto, A. D., Simon, J. D., Stanimirović, S., et al. 2007, ApJ, 655, 212

Bot, C., Boulanger, F., Lagache, G., Cambrésy, L., & Egret, D. 2004, A&A, 423, 567

Bot, C., Ysard, N., Paradis, D., et al. 2010, A&A, 523, A20

Boulanger, F., Abergel, A., Bernard, J.-P., et al. 1996, A&A, 312, 256

Bradley, J., Dai, Z. R., Erni, R., et al. 2005, Science, 307, 244

Brüns, C., Kerp, J., Staveley-Smith, L., et al. 2005, A&A, 432, 45

Campbell, E. K., Holz, M., Gerlich, D., & Maier, J. P. 2015, Nature, 523, 322

Cardelli, J. A., Clayton, G. C., & Mathis, J. S. 1988, ApJ, 329, L33

Cardelli, J. A., Clayton, G. C., & Mathis, J. S. 1989, ApJ, 345, 245

Cartledge, S. I. B., Clayton, G. C., Gordon, K. D., et al. 2005, ApJ, 630, 355

Chastenet, J., Bot, C., Gordon, K. D., et al. 2017, A&A, 601, A55

Compiègne, M., Verstraete, L., Jones, A., et al. 2011, A&A, 525, A103

Dale, D. A., Helou, G., Contursi, A., Silbermann, N. A., & Kolhatkar, S. 2001, ApJ, 549, 215

Dell'Agli, F., García-Hernández, D. A., Ventura, P., et al. 2015, MNRAS, 454, 4235

Demyk, K., Meny, C., Lu, X.-H., et al. 2017, A&A, 600, A123

Desert, F.-X., Boulanger, F., & Puget, J. L. 1990, A&A, 237, 215

D'Onghia, E. & Fox, A. J. 2016, ARA&A, 54, 363

Donn, B. 1968, ApJ, 152, L129

Draine, B. T. 2003a, ARA&A, 41, 241

Draine, B. T. 2003b, ApJ, 598, 1026

Draine, B. T., Dale, D. A., Bendo, G., et al. 2007, ApJ, 663, 866

Draine, B. T. & Lee, H. M. 1984, ApJ, 285, 89

Draine, B. T. & Li, A. 2001, ApJ, 551, 807

Draine, B. T. & Li, A. 2007, ApJ, 657, 810

Engelbracht, C. W., Blaylock, M., Su, K. Y. L., et al. 2007, PASP, 119, 994

Engelbracht, C. W., Rieke, G. H., Gordon, K. D., et al. 2008a, ApJ, 685, 678

Engelbracht, C. W., Rieke, G. H., Gordon, K. D., et al. 2008b, ApJ, 678, 804

Fazio, G. G., Hora, J. L., Allen, L. E., et al. 2004, ApJS, 154, 10

Fioc, M. & Rocca-Volmerange, B. 1997, A&A, 326, 950

Fioc, M. & Rocca-Volmerange, B. 1999, ArXiv Astrophysics e-prints

Fitzpatrick, E. L. 1999, PASP, 111, 63

Fitzpatrick, E. L. & Massa, D. 2005, AJ, 130, 1127

Galametz, M., Madden, S. C., Galliano, F., et al. 2011, A&A, 532, A56

Galliano, F., Hony, S., Bernard, J.-P., et al. 2011, A&A, 536, A88

Galliano, F., Madden, S. C., Jones, A. P., Wilson, C. D., & Bernard, J.-P. 2005, A&A, 434, 867

Galliano, F., Madden, S. C., Jones, A. P., et al. 2003, A&A, 407, 159

Gaustad, J. E., McCullough, P. R., Rosing, W., & Van Buren, D. 2001, PASP, 113, 1326

Gordon, K. D., Cartledge, S., & Clayton, G. C. 2009, ApJ, 705, 1320

Gordon, K. D. & Clayton, G. C. 1998, ApJ, 500, 816

Gordon, K. D., Clayton, G. C., Misselt, K. A., Landolt, A. U., & Wolff, M. J. 2003, ApJ, 594, 279

Gordon, K. D., Engelbracht, C. W., Fadda, D., et al. 2007, PASP, 119, 1019

Gordon, K. D., Galliano, F., Hony, S., et al. 2010, A&A, 518, L89

Gordon, K. D., Meixner, M., Meade, M. R., et al. 2011, AJ, 142, 102

Gordon, K. D., Misselt, K. A., Witt, A. N., & Clayton, G. C. 2001, ApJ, 551, 269

Gordon, K. D., Roman-Duval, J., Bot, C., et al. 2014, ApJ, 797, 85

Graczyk, D., Pietrzyński, G., Thompson, I. B., et al. 2014, ApJ, 780, 59

Griffin, M. J., Abergel, A., Abreu, A., et al. 2010, A&A, 518, L3

Griffin, M. J., North, C. E., Schulz, B., et al. 2013, MNRAS, 434, 992

Harris, J. 2007, ApJ, 658, 345

Heck, P. R., Gyngard, F., Ott, U., et al. 2009, ApJ, 698, 1155

Heger, M. L. 1922, Lick Observatory Bulletin, 10, 146

Henning, T. & Mutschke, H. 1997, A&A, 327, 743

Hobbs, L. M., York, D. G., Thorburn, J. A., et al. 2009, ApJ, 705, 32

Houck, J. R., Roellig, T. L., van Cleve, J., et al. 2004, ApJS, 154, 18

Hughes, A., Wong, T., Ott, J., et al. 2010, MNRAS, 406, 2065

Israel, F. P., Wall, W. F., Raban, D., et al. 2010, A&A, 519, A67

Jarosik, N., Bennett, C. L., Dunkley, J., et al. 2011, ApJS, 192, 14

Jenkins, E. B. 2009, ApJ, 700, 1299

Jenniskens, P. & Desert, F.-X. 1994, A&AS, 106

Jones, A. P. 2012a, A&A, 545, C2

Jones, A. P. 2012b, A&A, 545, C3

Jones, A. P. 2012c, A&A, 540, A1

Jones, A. P. 2012d, A&A, 540, A2

Jones, A. P. 2012e, A&A, 542, A98

Jones, A. P., Fanciullo, L., Köhler, M., et al. 2013, A&A, 558, A62

Jones, A. P., Köhler, M., Ysard, N., Bocchio, M., & Verstraete, L. 2017, A&A, 602, A46

Keller, S. C. & Wood, P. R. 2006, ApJ, 642, 834

Kennicutt, Jr., R. C., Armus, L., Bendo, G., et al. 2003, PASP, 115, 928

Kim, S., Staveley-Smith, L., Dopita, M. A., et al. 2003, ApJS, 148, 473

Köhler, M., Jones, A., & Ysard, N. 2014, A&A, 565, L9

Köhler, M., Ysard, N., & Jones, A. P. 2015, A&A, 579, A15

Kroto, H. W. & Jura, M. 1992, A&A, 263, 275

Le Bourlot, J., Le Petit, F., Pinto, C., Roueff, E., & Roy, F. 2012, A&A, 541, A76

Leger, A. & Puget, J. L. 1984, A&A, 137, L5

Leroy, A., Bolatto, A., Stanimirovic, S., et al. 2007, ApJ, 658, 1027

Lewis, N. K., Cook, T. A., Wilton, K. P., et al. 2009, ApJ, 706, 306

Li, A. & Draine, B. T. 2001, ApJ, 554, 778

Marigo, P., Girardi, L., Bressan, A., et al. 2008, A&A, 482, 883

Mathis, J. S. 1990, ARA&A, 28, 37

Mathis, J. S., Mezger, P. G., & Panagia, N. 1983, A&A, 128, 212

Mathis, J. S., Rumpl, W., & Nordsieck, K. H. 1977, ApJ, 217, 425

Mathis, J. S., Whitney, B. A., & Wood, K. 2002, ApJ, 574, 812

Mattila, K. 1970, A&A, 9, 53

Mattila, K., Lemke, D., Haikala, L. K., et al. 1996, A&A, 315, L353

Meisner, A. M. & Finkbeiner, D. P. 2015, ApJ, 798, 88

Meixner, M., Gordon, K. D., Indebetouw, R., et al. 2006, AJ, 132, 2268

Meixner, M., Panuzzo, P., Roman-Duval, J., et al. 2013, AJ, 146, 62

Meixner, M., Panuzzo, P., Roman-Duval, J., et al. 2015, AJ, 149, 88

Merrill, P. W. 1934, PASP, 46, 206

Merrill, P. W. & Wilson, O. C. 1934, ApJ, 80, 19

Mezger, P. G., Mathis, J. S., & Panagia, N. 1982, A&A, 105, 372

Misselt, K. A., Gordon, K. D., Clayton, G. C., & Wolff, M. J. 2001, ApJ, 551, 277

Mizuno, N., Rubio, M., Mizuno, A., et al. 2001, PASJ, 53, L45

Molinari, S., Swinyard, B., Bally, J., et al. 2010, PASP, 122, 314

Müller, T., Nielbock, M., Balog, Z., Klaas, U., & Vilenius, E. 2011, PACS Photometer - Point-Source Flux Calibration, Tech. Rep. PICC-ME-TN-037, Herschel

Nanni, A., Bressan, A., Marigo, P., & Girardi, L. 2013, MNRAS, 434, 2390

Neugebauer, G., Habing, H. J., van Duinen, R., et al. 1984, ApJ, 278, L1

Ochsenbein, F., Bauer, P., & Marcout, J. 2000, A&AS, 143, 23

Oort, J. H. & van de Hulst, H. C. 1946, Bull. Astron. Inst. Netherlands, 10, 187

Paradis, D., Paladini, R., Noriega-Crespo, A., et al. 2012, A&A, 537, A113

Paradis, D., Reach, W. T., Bernard, J.-P., et al. 2009, AJ, 138, 196

Pilbratt, G. L., Riedinger, J. R., Passvogel, T., et al. 2010, A&A, 518, L1

Planck Collaboration, Abergel, A., Ade, P. A. R., et al. 2014, A&A, 566, A55

Platt, J. R. 1956, ApJ, 123, 486

Poglitsch, A., Waelkens, C., Geis, N., et al. 2010, A&A, 518, L2

Purcell, E. M. & Pennypacker, C. R. 1973, ApJ, 186, 705

Putman, M. E., Staveley-Smith, L., Freeman, K. C., Gibson, B. K., & Barnes, D. G. 2003, ApJ, 586, 170

Reach, W. T., Dwek, E., Fixsen, D. J., et al. 1995, ApJ, 451, 188

Reach, W. T., Megeath, S. T., Cohen, M., et al. 2005, PASP, 117, 978

Rémy-Ruyer, A., Madden, S. C., Galliano, F., et al. 2014, A&A, 563, A31

Rieke, G. H., Young, E. T., Engelbracht, C. W., et al. 2004, ApJS, 154, 25

Rolleston, W. R. J., Trundle, C., & Dufton, P. L. 2002, A&A, 396, 53

Roman-Duval, J., Gordon, K. D., Meixner, M., et al. 2014, ApJ, 797, 86

Roman-Duval, J., Jackson, J. M., Heyer, M., Rathborne, J., & Simon, R. 2010, ApJ, 723, 492

Russell, S. C. & Dopita, M. A. 1992, ApJ, 384, 508

Sandstrom, K. M., Bolatto, A. D., Bot, C., et al. 2012, ApJ, 744, 20

Sandstrom, K. M., Bolatto, A. D., Draine, B. T., Bot, C., & Stanimirović, S. 2010, ApJ, 715, 701

Stanimirović, S., Staveley-Smith, L., & Jones, P. A. 2004, ApJ, 604, 176

Stanimirovic, S., Staveley-Smith, L., van der Hulst, J. M., et al. 2000, MNRAS, 315, 791

Staveley-Smith, L., Kim, S., Calabretta, M. R., Haynes, R. F., & Kesteven, M. J. 2003, MNRAS, 339, 87

Steinacker, J., Baes, M., & Gordon, K. D. 2013, ARA&A, 51, 63

Stock, D. J. & Peeters, E. 2017, ApJ, 837, 129

Tchernyshyov, K., Meixner, M., Seale, J., et al. 2015, ApJ, 811, 78

Trumpler, R. J. 1930, PASP, 42, 214

van der Marel, R. P. & Kallivayalil, N. 2014, ApJ, 781, 121

Volten, H., Muñoz, O., Hovenier, J. W., et al. 2007, A&A, 470, 377

Walker, A. R. 2012, Ap&SS, 341, 43

Weingartner, J. C. & Draine, B. T. 2001, ApJ, 548, 296

Welty, D. E., Lauroesch, J. T., Blades, J. C., Hobbs, L. M., & York, D. G. 2001, ApJ, 554, L75

Werner, M. W., Roellig, T. L., Low, F. J., et al. 2004, ApJS, 154, 1

Whitney, B. A. 2011, Bulletin of the Astronomical Society of India, 39, 101

Witt, A. N. & Gordon, K. D. 2000, ApJ, 528, 799

Witt, A. N. & Stephens, T. C. 1974, AJ, 79, 948

Ysard, N., Köhler, M., Jones, A., et al. 2015, A&A, 577, A110

Zubko, V., Dwek, E., & Arendt, R. G. 2004, ApJS, 152, 211

Zubko, V. G., Mennella, V., Colangeli, L., & Bussoletti, E. 1996, MNRAS, 282, 1321

Part V

Annexes

A

Extinctions curves

Here I show the results for my estimation of extinction curves based on dust properties derived from dust emission fitting. There are 4 lines of sight in the SMC, and 19 in the LMC, all labelled with the star used to measure the extinction curve.

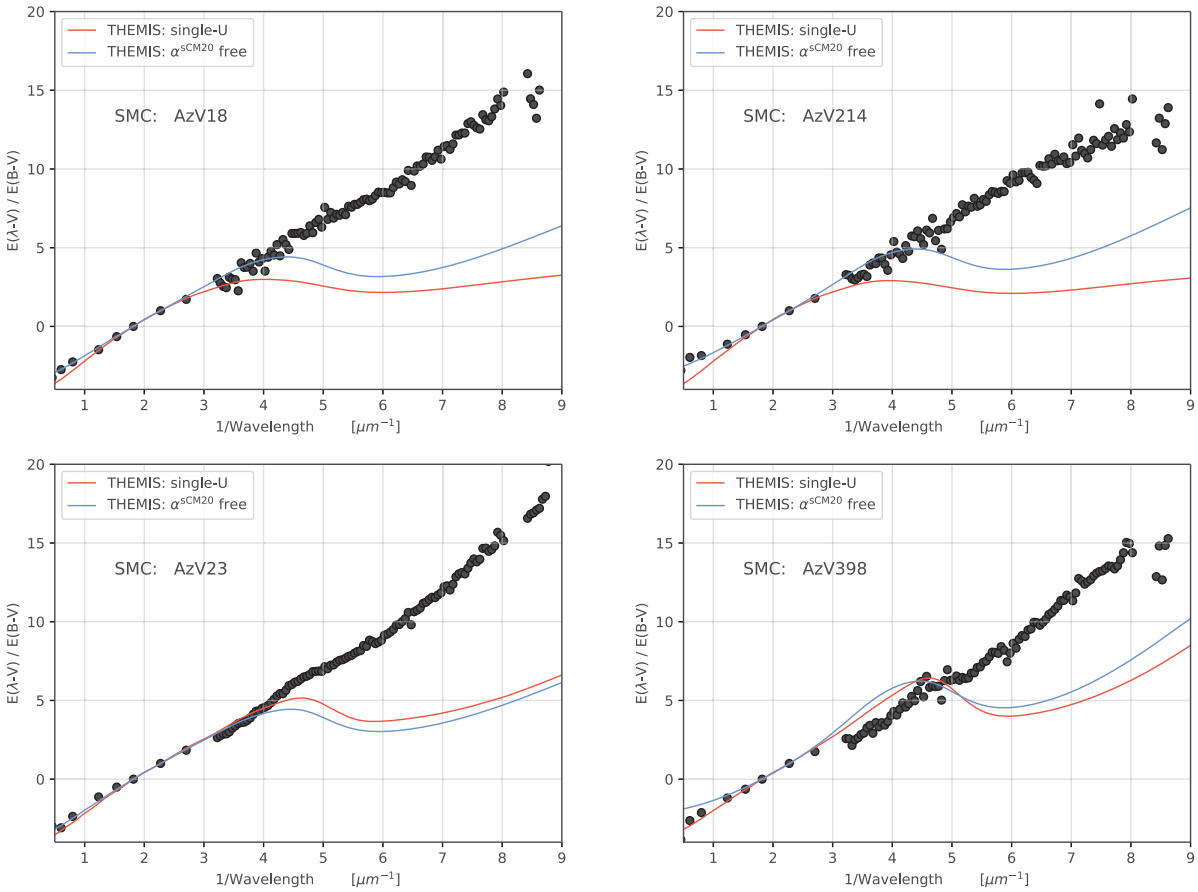

Figure A.1: Extinction curves in the SMC observed by Gordon et al. (2003) (grey circles), and the modeled curves created from emission-derived dust parameters (see Section 8.2).

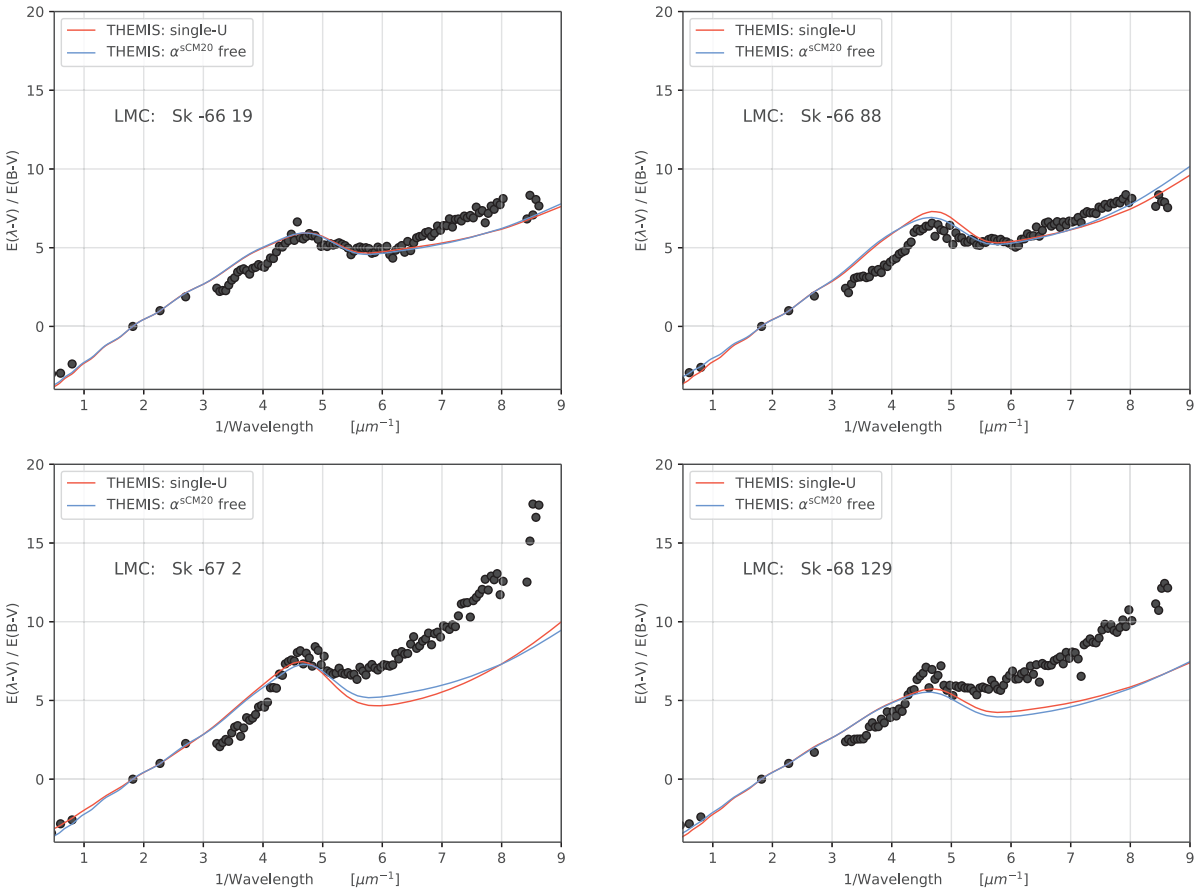

Figure A.2: Extinction curves in the LMC observed by Gordon et al. (2003) (grey circles), and the modeled curves created from emission-derived dust parameters (see Section 8.2).

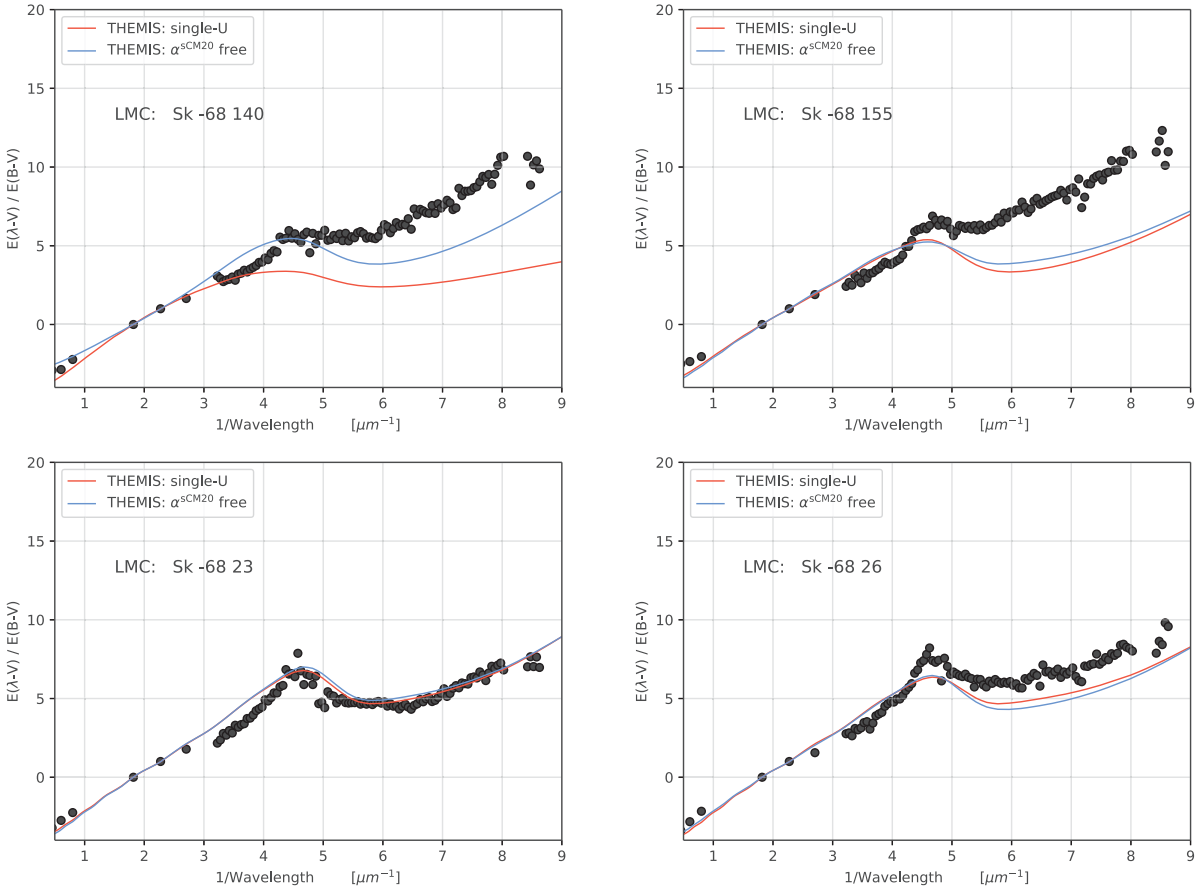

Figure A.3: Figure A.2 continued.

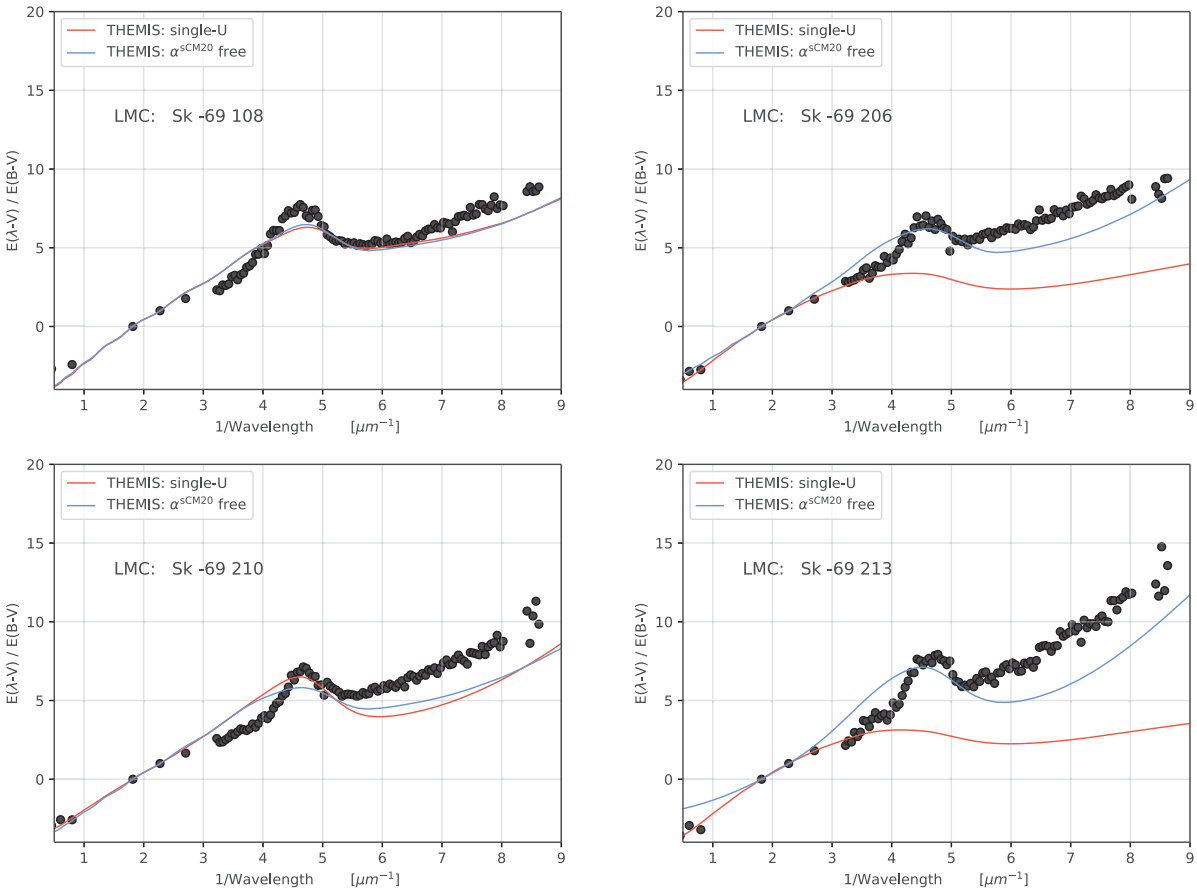

Figure A.4: Figure A.2 continued.

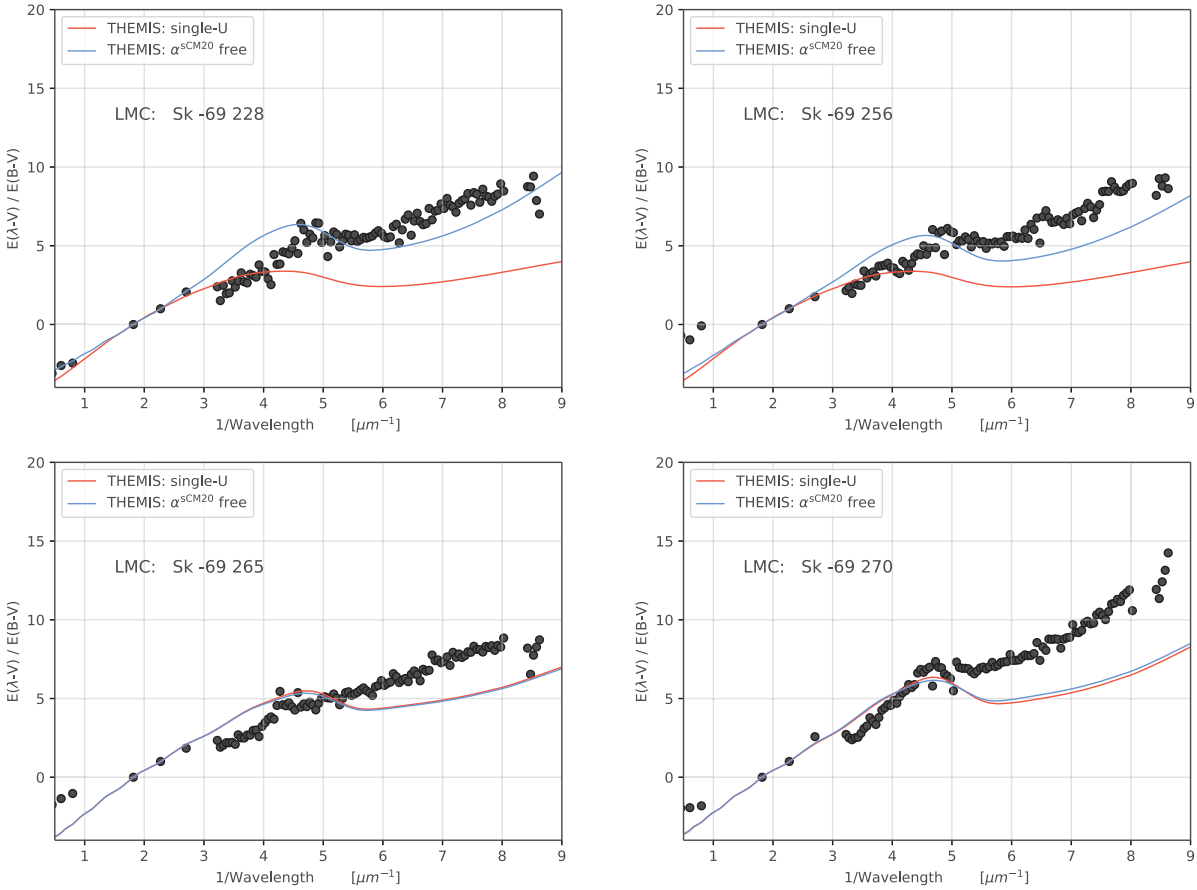

Figure A.5: Figure A.2 continued.

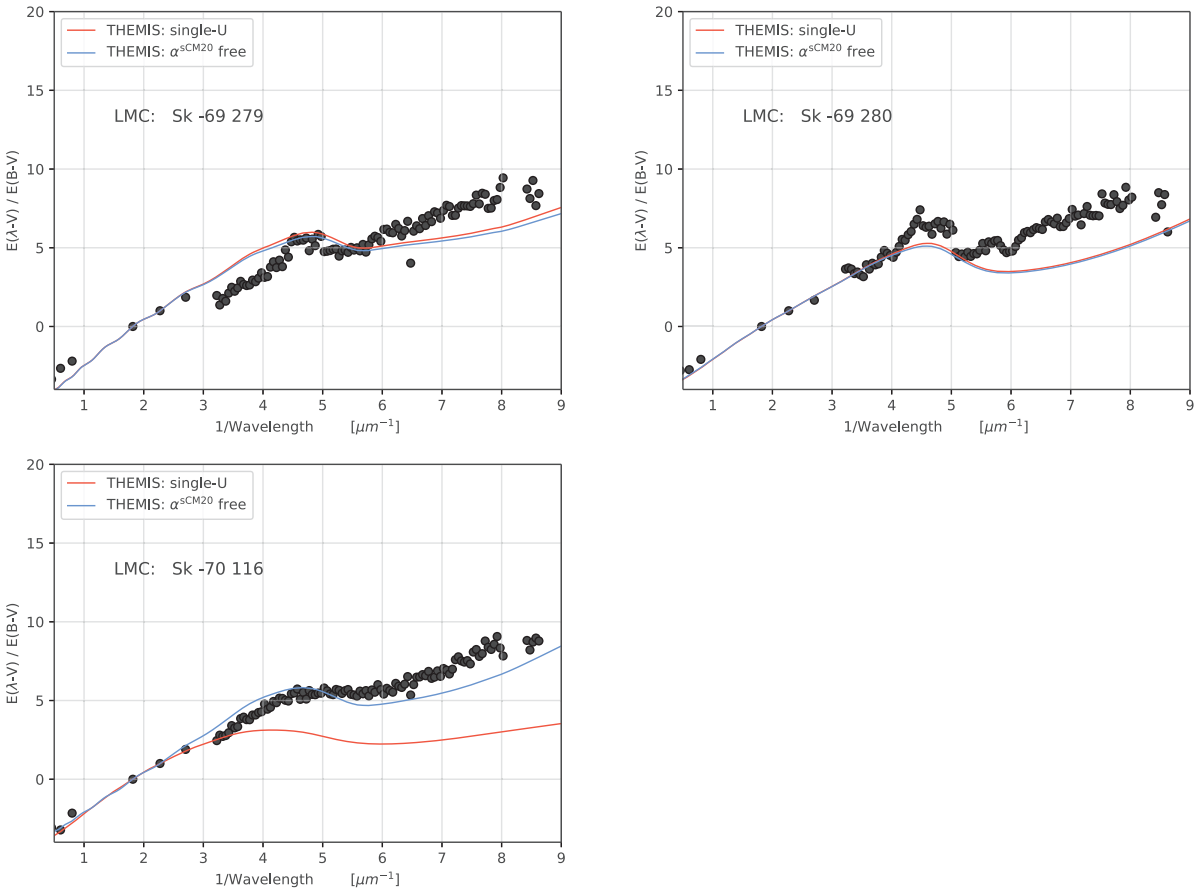

Figure A.6: Figure A.2 continued.

B

THEMIS parameters: triangular plots

I present here the triangular plots for two environments of Part II: a single ISRF and multi-ISRFs. This type of figure aims at showing possible degeneracies between parameters. We do not see strong variations between both approaches, and a slight difference between the galaxies, when it comes to the aSilM5 parameter.

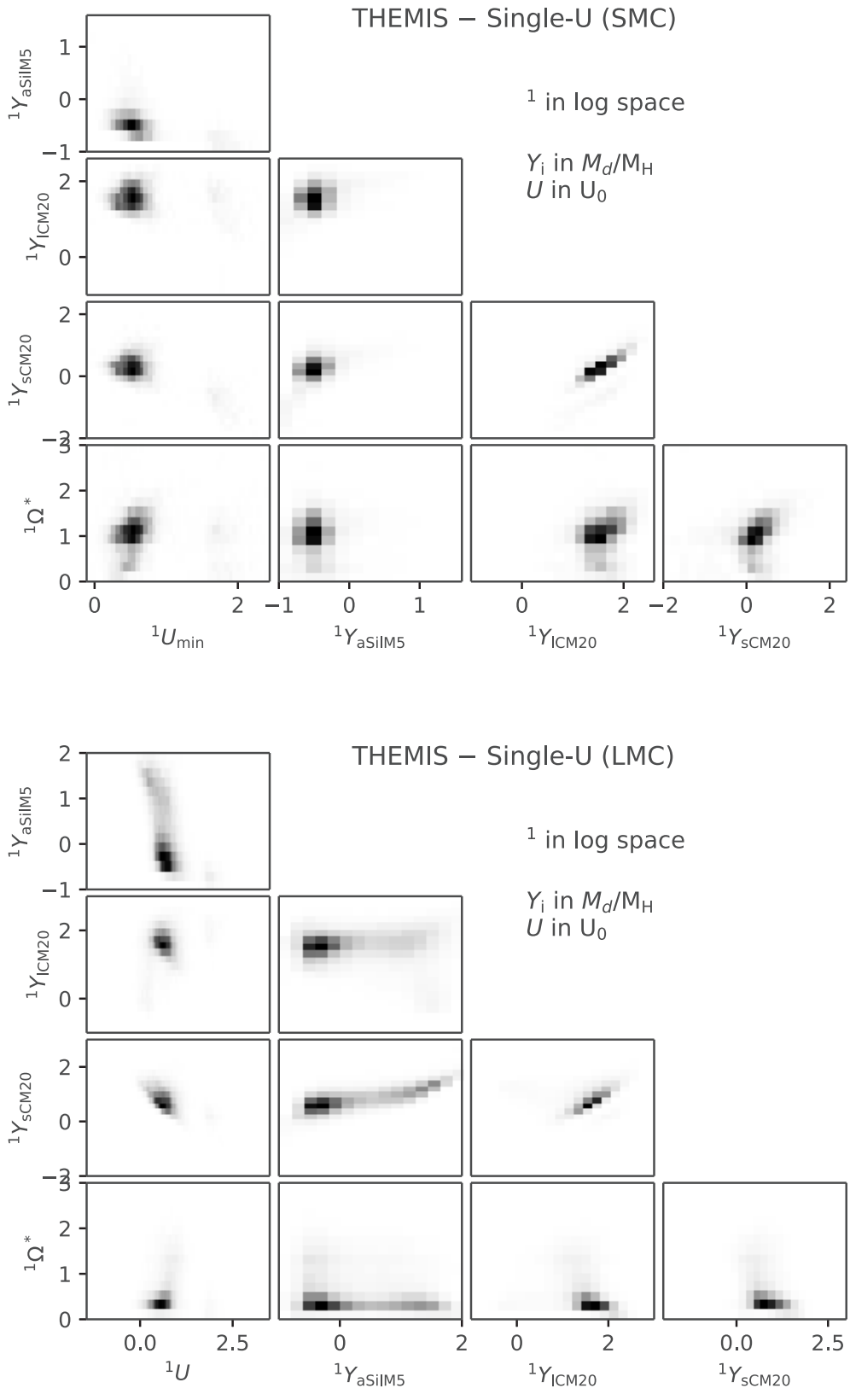

Figure B.1: Triangular plots showing parameter relationships for THEMIS in a Single-U environment in the MC (top) and LMC (bottom).

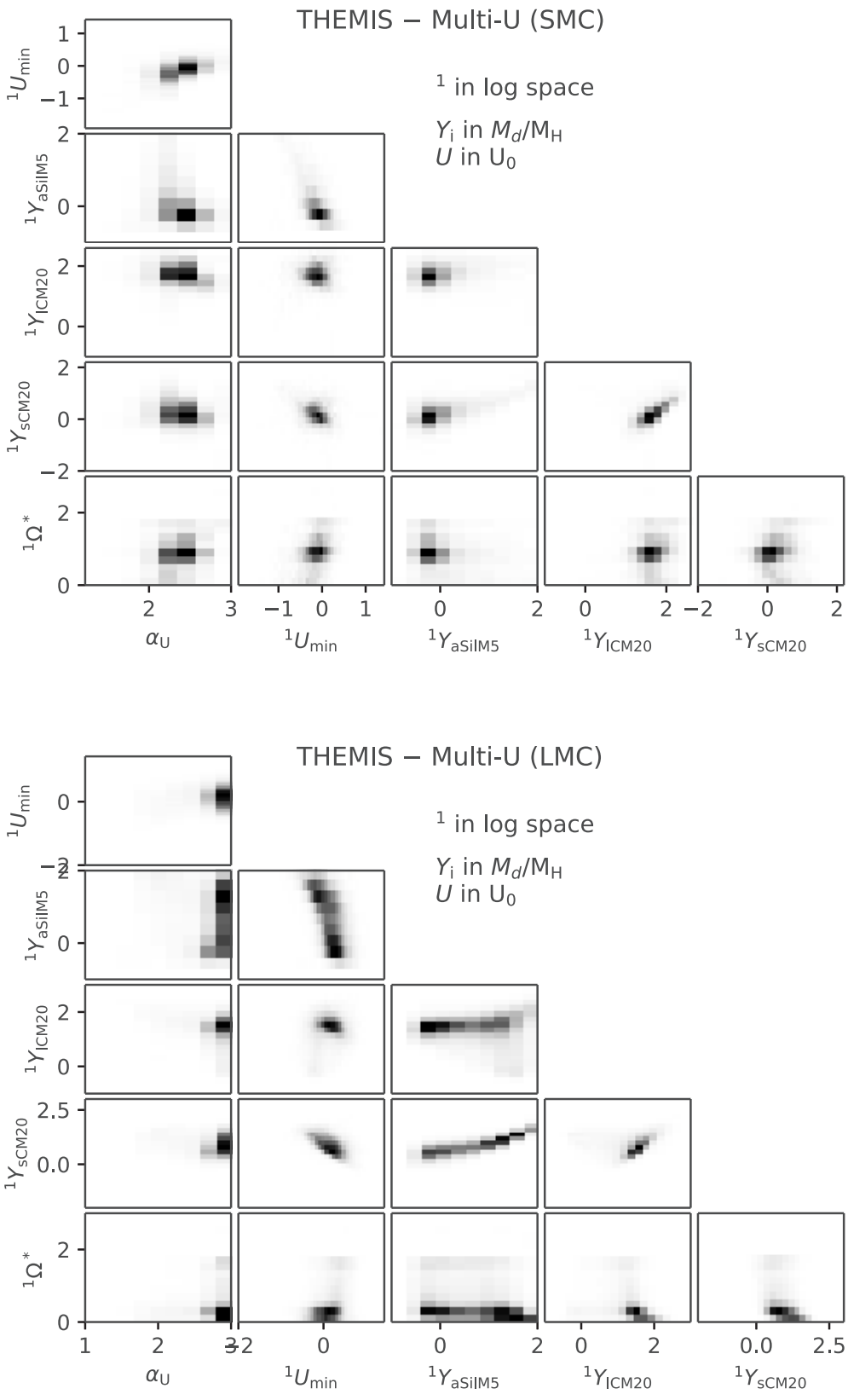

Figure B.2: Same as Figure B.1 in a Multi-U environment.

UNIVERSITÉ DE STRASBOURG

ÉCOLE DOCTORALE Physique, Chimie-Physique

UMR 7550

THÈSE présentée par :

Jérémy CHASTENET

soutenue le : **26 septembre 2017**

pour obtenir le grade de : **Docteur de l'université de Strasbourg**

Discipline/Spécialité : Astrophysique

Analyse de l'émission des poussières dans les galaxies proches

Impact des hypothèses et choix des modèles

THÈSE dirigée par :

Mme BOT Caroline	Astronome adjointe, Observatoire astronomique de Strasbourg
M. GORDON Karl	Astronome, Space Telescope Science Institute

RAPPORTEURS :

Mme MADDEN Suzanne	Ingénieur CEA, CEA
M. BAES Maarten	Professeur en Astrophysique, Sterrenkundig Observatorium

---

AUTRES MEMBRES DU JURY :

Mme DEMYK Karine	Directrice de Recherche, IRAP
Mme GENOVA Françoise	Directrice de Recherche, Observatoire astronomique de Strasbourg
M. CAMBRESY Laurent	Astronome, Observatoire astronomique de Strasbourg

Introduction générale

L'espace est rempli d'une quantité considérable d'objets d'une grande variété : des étoiles de différentes masses, des galaxies de différentes formes, des planètes lointaines et d'immenses nuages de gaz et de tout petits grains de poussières.
Pendant ma thèse, je me suis attaché à étudier ce que l'on appelle la poussière. Il s'agit de petits grains solides associés au gaz, dont la taille varie entre le nanomètre et le micromètre. On trouve ces grains de poussière dans les disques de formation planétaire ou dans un milieu dit interstellaire : l'espace entre les étoiles, au sein d'une galaxie. Nous nous intéresserons en particulier à cette poussière interstellaire, et plus précisément, celle que l'on peut trouver dans les galaxies proches de la notre.
Avant toute chose, revoyons brièvement les différentes parties du spectre électromagnétique, les informations qu'elles relaient, et le domaine d'étude de cette thèse.
Les rayons Gamma permettent d'observer les objets très énergétiques et/ou très chauds, tels que des étoiles à neutrons ou les alentours des trous noirs. Les rayons-X sont caractéristiques d'objets un peu moins chauds comme du gaz à haute température ou les restes d'une supernova. L'ultraviolet (UV) rend compte principalement de l'émission des étoiles jeunes, tandis que des étoiles plus vieilles sont visibles dans le domaine optique (observable à l'oeil nu). Dans le domaine infrarouge (IR), on observe majoritairement l'émission de la poussière, et ce sont ces longueurs d'onde qui vont nous intéresser, de quelques micromètres à un peu moins d'un millimètre. Enfin, les ondes radio nous permettent de voir la matière froide, comme du gaz à basse température ou des nuages moléculaires.

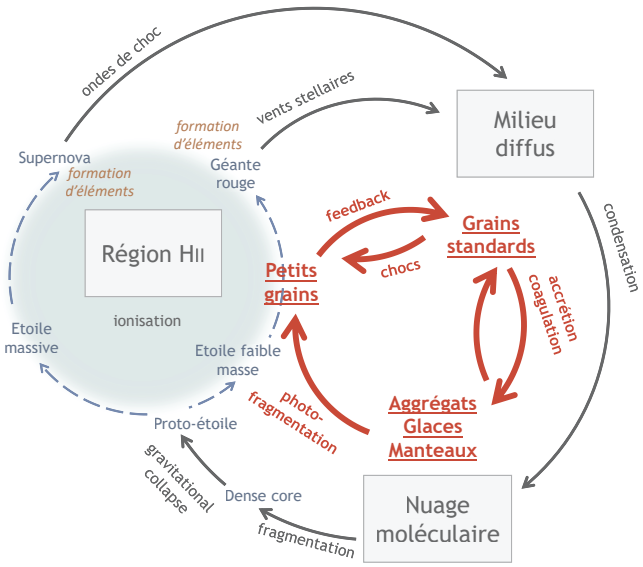

Figure B.3: Schéma simplifié du cycle du MIS.

Puisque nous nous intéressons à la poussière interstellaire, il convient d'introduire un peu le milieu qu'elle constitue avec le gaz : le milieu interstellaire (MIS). Les grains de poussière évoluent selon un cycle dans le MIS. Partons du nuage moléculaire, sur la Figure B.3 : c'est un dense nuage de gaz, principalement composé de H_2. On y trouve des agglomérats de grains, collés entre eux, avec d'épais manteaux, possiblement faits de glace (H_2O, CO_2). Ce nuage moléculaire peut donner vie à des étoiles s'il devient assez dense et s'effondre sur lui-même. La génération d'étoiles ainsi formées créent des éléments lourds par nucléosynthèse. Ces éléments se retrouvent dans les grains de poussière, qui font leur apparition dans les enveloppes d'étoiles relativement massives. Par la suite, ces nouvelles étoiles génèrent des photons UV capables d'ioniser les atomes d'hydrogène alentours. S'ils sont suffisamment énergétiques, ils peuvent également éroder, voire briser, les grains de poussière. Cette région ionisée est dénommée région H II. Ces grains sont "rendus" au milieu diffus. La formation d'un nouveau nuage dense dépend de la gravité ; la coagulation des grains est possible dans ces nuages. La composition et la taille des grains varient d'une région à l'autre. On définit la distribution de taille

standard de la poussière par celle du milieu diffus. Pour étudier la poussière dans ces régions, on définit aussi le champ de rayonnement. Il s'agit du spectre d'énergie des photons reçus par les grains. C'est une donnée importante qui impacte directement l'émission IR de la poussière, puisque c'est cette énergie qui sert à chauffer les grains. Mezger et al. (1982) et Mathis et al. (1983) ont produit plusieurs de ces spectres pour décrire le champs de rayonnement à différentes distances du centre galactique. La référence très souvent utilisée est celle à $D_{\mathrm{G}} = 10$ kpc, distance du Soleil au Centre galactique estimée à l'époque. En utilisant cette information, et les équations de la physique du solide, nous pouvons maintenant dresser quelques caractéristiques importantes de la poussière.

Description de la poussière interstellaire

La poussière peut s'observer par différents moyens : par son extinction, sa capacité à absorber et diffuser les rayons UV, son émission dans l'IR ou sa polarisation avec le champ magnétique. Il est important de décrire correctement la poussière, afin de créer des modèles adéquats qui reproduisent les observations, et pouvoir en déduire des propriétés dans les galaxies autres que la notre.

Extinction L'intensité de la lumière passant dans un nuage de poussière est atténuée, en fonction du nombre et de la composition des particules présentes et de la densité du nuage. Le terme d'extinction A_λ varie selon la section efficace d'extinction $C_{\mathrm{ext}}(a,\lambda) = Q_{\mathrm{ext}}(a,\lambda)\ \pi a^2$. L'efficacité d'extinction $Q_{\mathrm{ext}}(a,\lambda)$ traduit les propriétés des grains de poussière considérés.

L'extinction est l'effet cumulé de deux processus : l'absorption et la diffusion. Le premier décrit la capacité des grains à absorber un photon UV, qui provoque une augmentation de l'énergie interne du grain. Le second processus décrit la redirection des photons UV lorsqu'ils heurtent un grain de poussière : l'énergie du photon est la même, mais sa direction change. Lorsque la longueur d'onde de l'onde incidente est plus grande que la taille du grain, plus le grain est petit, plus l'absorption l'emporte sur la diffusion.

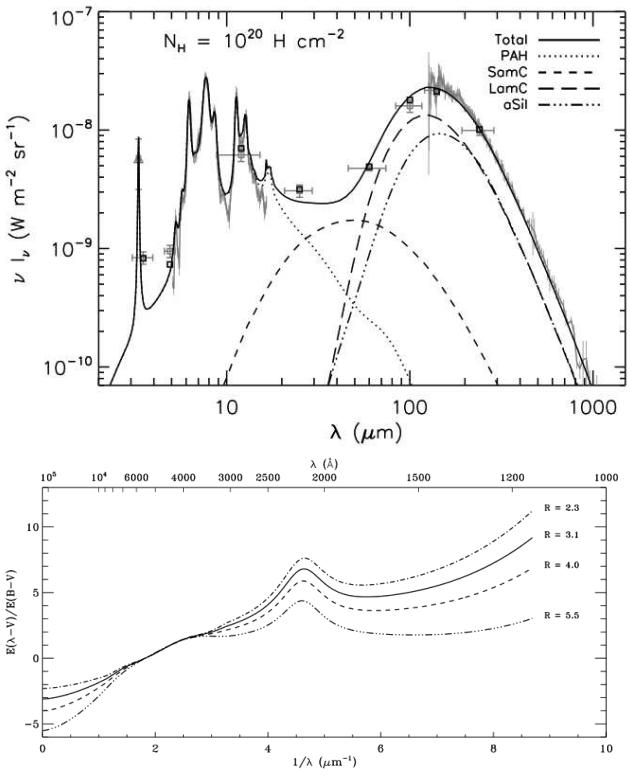

Figure B.4: *Haut :* Spectre d'émission (Compiègne et al. 2011). *Bas :* Courbe d'extinction (Fitzpatrick 1999).

Les variations de l'extinction avec la longueur d'onde sont en général montrées par une courbe d'extinction normalisée dans la bande V, comme sur la Figure B.4. Elle montre les particularités de l'extinction comme la bosse à 2175 Å, ou la pente à grand $1/\lambda$.

La distribution de taille des grains est estimée principalement par ces observations. Les modèles prédisent que les grains couvrent un intervalle de taille assez large, allant de 0.01 à 0.2 μm.

Émission L'émission de la poussière dépend de la quantité d'énergie qu'elle absorbe. On distingue en général deux types d'émission des grains. Les grains suffisamment gros sont soumis à un flux incident constant de photons, et ré-émettent cette énergie en continu. On décrit cette émission par un corps noir modifié, en utilisant la fonction de Planck $B(\lambda, T_{\rm d})$. La pente dans l'infrarouge lointain est modifiée par l'émissivité des grains, qui traduit leur capacité à absorber et émettre la lumière. Si le grain est trop petit pour absorber des photons continuellement, on parle de chauffage stochastique. A chaque absorption d'un photon, un grain de poussière voit son énergie interne et sa température augmenter de façon drastique, avant de se refroidir lentement, jusqu'au prochain impact. Ce type de chauffage est décrit dans les modèles de façon différente. La Figure B.4 montre un exemple de spectre d'émission avec ses différents parties. Dans l'infrarouge moyen ($3\ \mu\text{m} \leq \lambda \leq 30\ \mu\text{m}$), les pics d'émission sont caractéristiques des modes de vibrations de grosses molécules identifiées comme étant des hydrocarbonés aromatiques polycycliques (PAH).

Composition chimique La teneur en éléments des grains de poussière est cruciale pour être à même de reproduire les observations. En combinant les équations qui décrivent l'extinction et les observations, il est possible de déduire le volume occupé par les grains de poussière, relativement à celui des atomes d'hydrogène. Cela permet de mettre une limite sur la masse de la poussière, et d'en déduire que d'autres éléments que l'hydrogène ou l'hélium contribuent forcément à cette masse.
En mesurant les raies d'absorption du gaz interstellaire, on peut en déterminer la composition chimique : carbone, oxygène, magnésium, silicium, fer... Il est également possible de connaitre la composition chimique du voisinage solaire (cette valeur est souvent utilisée comme référence pour l'abondance totale en éléments du MIS). La composition de la poussière est déduite par ce qu'on appelle la déplétion : la différence entre l'abondance observée d'une étoile représentative du MIS étudié et celle du gaz.

Modèles de grains En utilisant les informations précédemment développées, il est possible de construire un modèle (dans cette thèse, il s'agit de modèles d'émission) décrivant les propriétés physico-chimiques des grains, afin de reproduire les observations de galaxies.
Les modèles les plus simples s'intéressent uniquement à l'émission des gros grains. Ils utilisent un corps noir modifié par différentes approches : une simple loi de puissance pour décrire l'émissivité des grains à grand λ, deux lois de puissance, ou encore deux populations de grains à deux températures différentes (voir Gordon et al. 2014).
Des modèles plus complets couvrent une plus large distribution de taille de grains, et prédisent un spectre d'émission du proche infrarouge au sub-millimétrique. On peut nommer par exemple :

- Draine & Li (2007, DL07) : qui émerge des travaux de Draine & Lee (1984), avec des mises à jour sur la taille et physique des grains (Draine & Li 2001; Li & Draine 2001; Weingartner & Draine 2001). Ce modèle utilise une population de carbone graphite et une population de grains silicatés. C'est le modèle le plus utilisé pour modéliser la poussière.
- Compiègne et al. (2011) : s'inspire du modèle de Desert et al. (1990), avec des modifications venant des travaux de Draine & Lee (1984), Zubko et al. (1996), Draine (2003b) et Draine & Li (2007).
- THEMIS[1] : développé par Jones et al. (2013), Köhler et al. (2014) et Ysard et al. (2015), ce modèle accorde une place importante à de nouvelles mesures en laboratoire (Jones 2012c,d,a,e,b). Ce modèle décrit la poussière par des grains carbonés aliphatiques et des grains silicatés, chacun recouvert d'un manteau aromatique.

[1] *The Heterogeneous Evolution dust Model at the IAS.*

La plupart des modèles sont calibrés (ajustement des densités, masses initiales et distribution de tailles) sur l'émission du milieu interstellaire diffus de la Voie Lactée (VL), mais la méthode varie.

Modéliser l'émission de la poussière dans les galaxies proches

Contexte et objets de l'étude Les galaxies dites proches représentent d'excellents sujets de recherche. Bien que les observations de la VL offrent une meilleure résolution, les limitations sont nombreuses ; par exemple, la présence de nombreux objets dans le disque galactique empêche de distinguer clairement les contributions respectives de ces objets au signal total reçu ; on peut aussi être gêné par un avant-plan de la VL. Observer les galaxies proches peut, dans certains cas, permettre de s'affranchir en partie de ces inconvénients. Cependant, une résolution trop peu fine peut conduire à un mélange de signaux dans un pixel, même dans ces galaxies. Malgré cela, observer les environnements divers (métallicité, taux de formation d'étoiles, âge...) de ces galaxies, et en plus grand nombre, est un argument puissant.
Plusieurs études ont identifié des propriétés de la poussière variant d'une galaxie à l'autre, et au sein même d'une galaxie (e.g. Cardelli et al. 1988; Fitzpatrick & Massa 2005; Cartledge et al. 2005; Gordon et al. 2009). Dans cette étude, deux modèles de poussière sont utilisés pour ajuster l'émission IR des Nuages de Magellan (*Small* et *Large Magellanic Clouds* : SMC et LMC, Figure B.5) ; l'ajustement est fait de façon homogène, afin d'identifier d'éventuelles différences dans les résultats, dues aux différences dans les modèles. Le SMC et le LMC sont deux galaxies irrégulières, proches de la VL (62 et 50 kpc, respectivement, Graczyk et al. 2014; Walker 2012), avec une plus faible métallicité (1/5 et 1/2 $Z_{\odot}$, respectivement, Rolleston et al. 2002). Plusieurs travaux se sont intéressés à ces galaxies, et ont notamment identifié des excès d'émission (e.g. Bot et al. 2004; Bernard et al. 2008; Gordon et al. 2014) par rapport aux modèles existants. Les observations que j'ai utilisées ici sont celles des projets *Spitzer* SAGE-SMC et SAGE-LMC (Gordon et al. 2011; Meixner et al. 2006) et *Herschel* HERITAGE (Meixner et al. 2013). Cela correspond à 11 bandes photométriques, allant de 3,6 à 500 μm. Des modifications communes aux deux lots d'images ont été mises en place afin d'homogénéiser les données : dégradation à résolution commune, soustraction de l'avant- et arrière-plan et repixelisation.

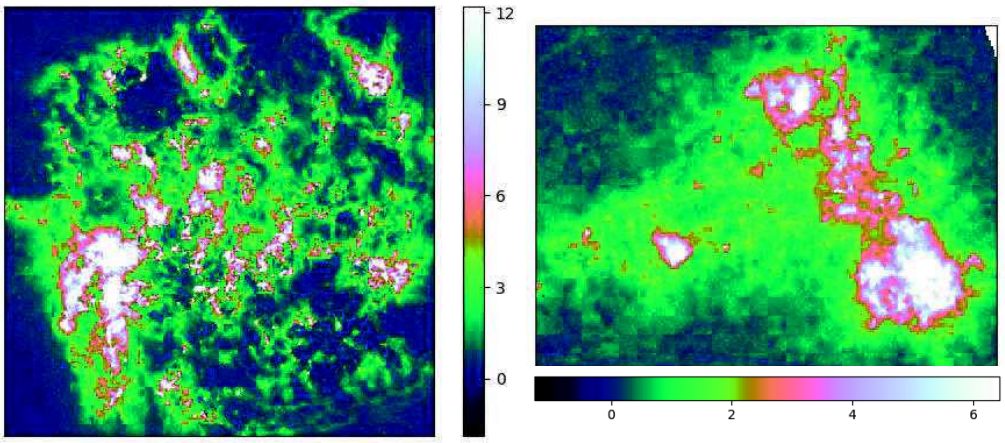

Figure B.5: Images de la bande SPIRE à 500 μm du Grand Nuage de Magellan (LMC, *gauche*) et du Petit Nuage de Magellan (SMC, *droite*). Les échelles sont en MJy/sr.

Outils utilisés Afin de créer les spectres d'émission à ajuster aux données, j'ai utilisé l'outil DustEM (Compiègne et al. 2011). Pour une composition donnée, avec les valeurs liées aux propriétés des grains choisis (Q, C, distribution de taille...), DustEM calcule l'extinction et l'émission de la poussière considérée, soumise à un champ de rayonnement (par défaut, celui de Mathis et al. 1983, à 10 kpc). Le modèle de Compiègne et al. (2011, MC11) et THEMIS sont utilisés dans cette étude. Ils divergent par la nature des grains pris en compte (MC11 utilise une population de PAH, tandis que THEMIS modélise ceci par des manteaux aromatiques), la pente dans l'IR lointain (grains silicatés et carbonés ont le même indice spectral dans MC11, différent dans THEMIS), et leurs propriétés optiques et thermiques. Dans chaque cas, les paramètres libres sont : les abondances de chaque population de grains (3 par modèle), l'intensité du champ de rayonnement incident, et une composante stellaire (modélisée par un corps noir), soit au moins 5 degrés de liberté. Chaque spectre est intégré dans les mêmes bandes photométriques que les observations, résultant en des distributions spectrales d'énergie (SEDs).
L'ajustement des modèles aux données est faite avec DustBFF (Gordon et al. 2014). Il s'agit d'une méthode de calcul qui propage les incertitudes à l'aide de matrices de covariance ; elles décrivent les erreurs instrumentales sur les mesures et l'arrière-plan dans les données. Cela permet de tenir compte des corrélations entre les bandes d'observations. La probabilité qu'un modèle ajuste les données est calculé par un χ^2 qui prend en compte la matrice en question. Par ailleurs, cette méthode est aussi intéressante car elle définit des priors pour les valeurs des paramètres considérés. Cela prend en compte des probabilités constantes dans les intervalles choisis.

Comparaison des modèles Pour cette étude, j'ai créé les spectres d'émission de la poussière dans différents environnements. J'ai étudié plusieurs cas :

- un champ de rayonnement unique ;
- deux champs à différentes intensités, créant deux spectres d'émission – un 'chaud' et un 'froid' – qui résultent en un spectre unique à l'aide d'un paramètre réglant la fraction chaude/froide (Meisner & Finkbeiner 2015) ;
- une combinaison de spectres d'émission à différentes intensités de champs de rayonnement, résultant en un spectre unique par une intégration en loi de puissance (Dale et al. 2001).

Dans le premier cas, un champ de rayonnement unique, THEMIS reproduit mieux les observations que le modèle MC11. En particulier, dans le SMC, les résidus $(\nu I_\nu^{\rm data} - \nu I_\nu^{model})/\nu I_\nu^{\rm data}$ à $\lambda \geq 100$ μm montrent un mauvais ajustement de la pente dans l'IR lointain par le modèle MC11. Cela est dû à un indice spectral unique, qui représente mal l'aspect plus plat de la SED à grandes longueurs d'onde. Au contraire, l'indice spectral des grains carbonés de THEMIS s'accorde mieux à cette forme, et permet un meilleur ajustement des données. A courtes longueurs d'onde, $\lambda \leq 8$ μm, les deux modèles montrent de larges résidus (c'est-à-dire beaucoup d'erreurs), mais ceux du modèle MC11 sont plus centrés en 0, ce qui équivaut à un meilleur ajustement global. Ceci est vraisemblablement dû à la population des PAH de ce modèle, qui permet un meilleur ajustement dans ces bandes que la population des petits grains carbonés de THEMIS. Néanmoins, l'ajustement des bandes à 70 et 100 μm par le modèle MC11 est moins bon que celui obtenu par THEMIS. Globalement, THEMIS montre donc de meilleurs résultats.
Dans les deuxième et troisième cas (plusieurs champs de rayonnements), seul THEMIS est étudié en détail. Les résultats montrent qu'utiliser plusieurs champs de rayonnement, qui permet de prendre en compte les mélanges le long de la ligne de visée, permet de mieux ajuster les données. En particulier, la pente entre 8 et 70 μm est mieux reproduite par un environnement avec des champs de rayonnements intégrés en loi de puissance. Cela conduit à une meilleure

reproduction des données dans les courtes longueurs d'ondes ($\lambda \leq 24$ μm). D'un point de vue général, utiliser plusieurs champ de rayonnement permet de mieux centrer les résidus, ce qui démontre un meilleur ajustement des données, tant dans le SMC que dans le LMC.
Une autre approche est testée, pour tenter de reproduire mieux les bandes à $\lambda \leq 70$ μm : la distribution de tailles des petits grains carbonés est laissée libre, en utilisant un champ de rayonnement unique. Cette méthode montre également de meilleurs résultats que la première approche : à courtes longueurs d'onde, les résidus sont plus centrés en 0.

Propriétés des poussières dans les Nuages de Magellan Les propriétés des poussières dans le SMC et le LMC ont été déduites uniquement avec les résultats THEMIS.
Les variations spatiales des abondances de chaque population de grains (petits et gros grains carbonés et grains silicatés) montrent d'importantes variations entre elles, et selon le type d'environnement choisi. La quantité de gros grains carbonés est celle qui varie la moins d'une situation à l'autre, et est estimée avec de faibles incertitudes.
En revanche, seule une limite supérieure peut être posée quant à la quantité de grains silicatés. Les fonctions de probabilités de ce paramètre, dans la plupart des pixels, sont très plates ; cela se traduit par un ajustement équivalent quelque soit la quantité proposée, si elle est en-dessous de la limite. Le nombre de pixels montrant ce genre de résultats est de plus de 50% dans le SMC et d'environ 10% dans le LMC. En moyenne, la limite supérieure est de $Y_{\rm aSilM5} \sim 2,5\, M_{\odot}^{\rm aSilM5}/M_{\rm H}$, identique dans les deux galaxies. Ce résultat impacte directement le rapport SiO_2/C. Estimé à ~ 10 dans la VL, il varie entre 0,2 et 0,7 dans le SMC, et entre 0,3 et 1 dans le LMC. Ceci implique que la composition de la poussière n'est pas la même entre la VL et les Nuages de Magellan.

Un point important, et utile à la comparaison des résultats d'une étude à l'autre, est la masse totale de poussière estimée dans chaque galaxie. Dans le SMC, j'obtiens $(2,9-8,9)\times10^4$ $M_\odot$ et $(3,7-4,2)\times10^5$ $M_\odot$ dans le LMC (Figure B.6). Ces valeurs sont légèrement plus faibles que celles de l'étude faite par Gordon et al. (2014), en utilisant uniquement les bandes *Herschel*. Les erreurs considérées viennent directement de la qualité des ajustements, donnée par le calcul, pour chaque pixel. J'ai également calculé les rapports gaz-sur-poussière (GDR) : il s'agit du rapport en masse de la quantité totale de gaz (dans ce cas : hydrogène uniquement) et de celle de poussière. La masse de gaz est calculée par des observations en H I et CO (e.g. Stanimirovic et al. 2000; Mizuno et al. 2001). En considérant les résultats montrant les meilleurs résidus, les GDRs s'échelonnent entre 1000 et 1200 dans le SMC et entre 500 et 520 dans le LMC. Dans le SMC, les variations du GDR en fonction du choix du champ de rayonnement sont assez larges. Des études n'utilisant pas l'émission IR de la poussière ont aussi estimé des GDRs dans les Nuages de Magellan (e.g. Gordon et al. 2003; Tchernyshyov et al. 2015). Bien que les écarts puissent être parfois larges, mes résultats s'accordent raisonnablement avec ces résultats.

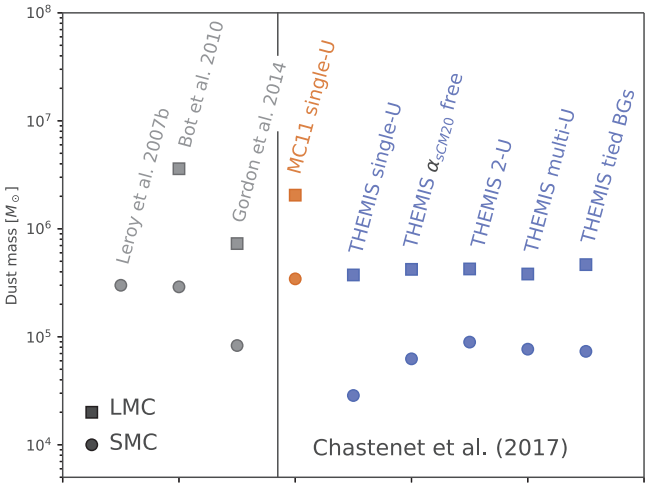

Figure B.6: Résumé des masses de poussière déduites dans mon étude, et quelques travaux précédents.

Impact pour d'autres études En utilisant ces résultats, je me suis intéressé à d'autres problèmes.
Par exemple, j'ai créé des courbes d'extinctions en utilisant les abondances dérivées des ajustement à l'émission. J'ai comparé ces courbes d'extinction à des mesures faites dans le SMC et LMC par Gordon et al. (2003). J'ai pu montrer qu'utiliser uniquement les propriétés liées à l'émission IR ne permet pas de reproduire l'extinction, et que les deux observables sont complémentaires.
J'ai aussi créé des spectres d'émission comme précédemment, mais en utilisant les champs de rayonnement construits par Mathis et al. (1983) à d'autres distances D_{G}. J'ai pu montrer que les résultats dans le SMC et le LMC quant à la force (ou distance) du champ de rayonnement qui ajuste le mieux les données sont différents.

Conclusions Cette étude a permis de démontrer que tous les modèles ne reproduisent pas aussi bien les données de galaxies proches comme les nuages de Magellan, bien qu'ils soient tous ajustés sur la VL. Cela a mis en évidence une composition de la poussière différente entre la VL, le SMC et le LMC. Les résultats ont aussi montré que les hypothèses de modélisation (i.e. d'environnement) peuvent affecter lourdement les propriétés déduites de la poussière.

Erreurs systématiques dans la modélisation de la poussière

L'étude précédente a démontré l'importance des choix faits dans la modélisation de l'émission IR de la poussière. Dans la seconde partie de ma thèse, je me suis intéressé à quantifier plus clairement les erreurs systématiques liées à ces choix. J'ai utilisé une méthode de transfert radiatif pour créer des spectres d'émission dont les propriétés sont connues ; j'ai ajusté ces spectres en les considérant comme des données observationnelles, avec les modèles couramment employés dans la littérature. Ces deux approches diffèrent dans la description du champ de rayonnement qui chauffe les grains. Dans le cas du transfert radiatif, ce champ est calculé en prenant en compte les interactions possibles ; dans le cas des modèles utilisés pour ajuster les données, il est décrit empiriquement. Comparer ces deux approches est donc intéressant pour en comprendre les différences.

Transfert radiatif Les méthodes de transfert radiatif (TR) consistent à modéliser le déplacement d'une onde/d'un paquet de photons dans un milieu ; dans le cas présent, ce milieu est un mélange d'étoiles et de poussière. Comme décrit précédemment, les grains de poussière absorbent la lumière UV et visible, et émettent un rayonnement IR. Ces interactions et contributions au spectre électromagnétique sont complexes, et les méthodes les plus simples de modélisation de l'émission IR n'en tiennent pas toujours compte. Le TR tend à palier ce problème, et cherche à résoudre l'intensité du champ de rayonnement en chaque position $\boldsymbol{x}$, direction $\boldsymbol{n}$ et longueur d'onde λ d'une certaine géométrie en 3 dimensions. Il s'agit néanmoins d'une méthode lourde à mettre en oeuvre : le problème est non-linéaire et non-local, et il n'existe pas de solution analytique. La prise en compte de l'absorption de la poussière, de l'émission et surtout de la diffusion par les grains fait de l'équation de TR une équation intégro-différentielle à 6 dimensions. Elle prend en compte les termes sources : émission "primaire" venant des étoiles et émission "secondaire" de la poussière ; la diffusion est également prise en compte. Ces termes contribuent positivement à l'intensité $I(\boldsymbol{x},\boldsymbol{n},\lambda)$. Les autres termes contribuent négativement à l'intensité et il s'agit de l'extinction par la poussière. Le calcul numérique permet, par itération, de déterminer l'intensité $I(\boldsymbol{x},\boldsymbol{n},\lambda)$ du champ de rayonnement, et l'émission et absorption des poussières en chaque point.

De nombreuses approches sont possibles pour résoudre l'équation de TR. Il convient d'en discrétiser une ou plusieurs dimension(s), de faire se déplacer les photons selon une méthode choisie, et de pouvoir en suivre le parcours. La méthode de résolution la plus employée est la méthode de Monte Carlo (MC) (voir par exemple Steinacker et al. 2013) ; ce type de méthode calcule la solution de façon probabiliste, en itérant le processus de nombreuses fois. C'est la méthode employée pour créer les données utilisées dans la suite.

DIRTYGrid et données simulées Le code de TR utilisé ici est DIRTY (Gordon et al. 2001; Misselt et al. 2001) ; en utilisant ces travaux, Law et al. *(in prep.)* ont créé la DIRTYGrid : il s'agit d'un ensemble de spectres et de SEDs, allant de l'UV à l'IR lointain, déterminée par calcul de TR combiné à un modèle de poussière. Le calcul prend en compte des paramètres stellaires (âge, taux de formation d'étoiles, type de formation, métallicité), les types de poussière de Weingartner & Draine (2001) et Draine & Li (2007) et la masse voulue, et une géométrie décrivant la distribution relative entre poussière et étoiles (*Shell*, *Dusty* ou *Cloudy* ; voir Witt & Gordon 2000). Tous ces paramètres couvrent une large gamme chacun, ce qui permet une bonne représentation de la diversité d'environnements rencontrés dans les galaxies proches.

Paramètre	# de valeurs
Type de grains	3
Géometrie	3
Homogénéité	2
Métallicité	5
Age stellaire	50
Masse de poussière	25
Type de formation d'étoiles	2
Taux de formation d'étoiles	29

Le calcul crée un grand nombre de spectres. Ces spectres sont intégrés dans les bandes photométriques de plusieurs instruments, en utilisant les courbes de transmissions, ce qui conduit à des SEDs. J'utilise la partie de ces SEDs qui se situe dans le domaine IR (les mêmes longueurs d'onde que l'étude précédente, de 3,6 à 500 μm).

Méthode Dans la suite de l'étude, ces points sont considérés comme des observations. Chaque SED calculée pour un ensemble de paramètres (stellaire, poussière, etc...) est ajustée par des modèles, et j'en déduis des propriétés de poussière. Néanmoins, la connaissance *a priori* des paramètres dans les SEDs synthétiques me permet de comparer les propriétés déduites de l'analyse des SEDs comme des "observations", avec ce qu'elles sont réellement dans les données. La suite du travail ne prend en compte que la poussière de type VL, et un seul scenario de formation stellaire. Les résultats sont regroupés par type de géométrie : pour chaque géométrie, je considère toutes les SEDs avec tous les autres paramètres libres.

Ajustement avec un modèle identique DIRTYGrid est construite avec le modèle de Draine & Li (2007). Dans un premier temps, je m'attache donc à utiliser le même modèle pour ajuster les SEDs synthétiques. Cela me permet de m'assurer que les possibles écarts entre les résultats déduits de l'ajustement et les propriétés *a priori* ne sont pas dus à des différences de modèle.
La qualité des ajustements est peu dépendante de la géométrie choisie. Les résidus $(\nu I_\nu^{\mathrm{DGrid}} - \nu I_\nu^{model})/\nu I_\nu^{\mathrm{DGrid}}$ suivent tous la même tendance. A $\lambda \geq 160$ μm, le modèle surestime le flux de la DIRTYGrid, dans chaque cas. Il est possible que la pente de l'émission des poussières dans l'IR lointain, affectée par les calculs de TR, ne soit pas correctement ajustée par le modèle de poussières utilisé dans l'analyse des observations.
Pour chaque ensemble de paramètres, la masse de poussière injectée dans les calculs des SEDs est connue ; il convient donc de vérifier si le modèle permet de déduire ces valeurs. La Figure B.7 montrent les résidus pour ces masses. Ici, les résultats sont dépendants de la géométrie choisie. Toutes les géométries montrent une distribution non gaussienne des résidus, avec un

certain nombre de résultats qui sur-estiment les masses. Néanmoins, l'une des géométries permet au modèle de mieux reproduire les masses de poussière : en s'intéressant aux maxima de ces résidus, on remarque que la géométrie *Dusty* offre les meilleurs résultats. Les autres géométries sur-estiment ou sous-estiment significativement les masses de poussière, par un facteur inférieur à 2. Il s'agit d'un effet intéressant lié aux calculs de TR. La quantité de PAH q_{PAH} retrouvée par le modèle d'analyse peut aussi être vérifiée. Les SEDs de la DIRTYGrid sont construites avec une valeur unique, et le modèle autorise plusieurs possibilités pour cette grandeur. Là encore, le modèle manque à reproduire la valeur *a priori*. Dans tous les cas de géométries, le modèle surestime q_{PAH}, et considère la valeur maximale possible (soit environ deux fois plus) comme étant celle qui reproduit le mieux les observations.
Les effets de TR induits par le calcul réaliste du champ de rayonnement ont donc de réels effets sur les propriétés de la poussière que l'on peut déduire en ajustant l'émission IR. Un ajustement raisonnable n'est pas forcément synonyme de caractéristiques exactes.

Avec un autre modèle Il est aussi intéressant d'essayer d'ajuster la DIRTYGrid avec un modèle de poussières ayant une composition différente de celle employée pour sa création. J'utilise pour cela le modèle THEMIS introduit précédemment.
Dans ce cas, la qualité des ajustements à grand λ est meilleure qu'avec le modèle DL07. Il apparait que la pente dans l'IR lointain décrite par THEMIS permet de mieux reproduire les données à ces longueurs d'onde. En revanche, les bandes à $\lambda \leq 70\ \mu$m sont très mal ajustées par THEMIS. En termes de masses, contrairement au modèle DL07, THEMIS ne montre qu'une sous-estimation des masses. Aucune géométrie ne permet de retrouver les valeurs correctes.

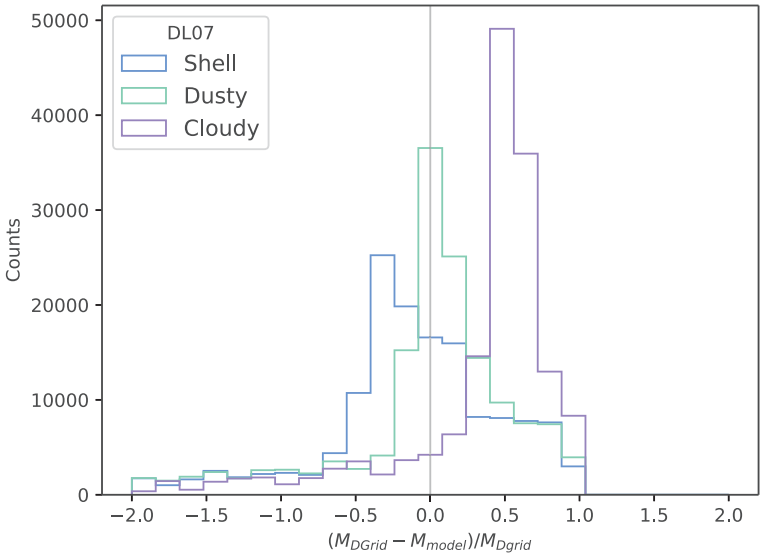

Figure B.7: Résidus en masses pour les trois géométries, en utilisant un modèle identique pour la création de DIRTYGrid et le modèle à ajuster.

Cela prouve cependant qu'une composition de la poussière différente que celle des observations peut conduire à un meilleur ajustement des données (dans certaines bandes photométriques) et que la composition déduite peut être impactée et refléter plus des effets de TR.

Conclusions Cette étude montre que les effets de géométrie et de TR sont importants dans les études en émission de la poussière. Les lois empiriques utilisées pour décrire le chauffage des grains dans les modèles "simples" ne s'accordent pas complètement avec les effets de TR. Cela conduit à une estimation biaisées de grandeurs comme la masse totale de poussière, bien que la qualité des ajustements soit en apparence corrects. Améliorer la description du champ de rayonnement dans les modèles apparait crucial.

Perspectives

Ma thèse s'est concentrée sur les conséquences des choix faits lors de la modélisation de l'émission IR de la poussière dans les galaxies proches, et leurs impacts sur les propriétés déduites des grains. Ces choix comprennent la nature du modèle (et par conséquent, la composition de la poussière, distribution de taille, propriétés optiques et thermiques) ou la description du champ de rayonnement et des lois de mélange (souvent empiriques).
Ces études ouvrent la voie à des questions et explorations supplémentaires ; par exemple :

- les résultats de cette thèse quant aux nuages de Magellan sont-ils observés dans d'autres galaxies proches ? Cette question sera abordée dans mon projet de post-doctorat. En collaboration avec le Dr Karin Sandstrom, je créerai et analyserai un catalogue des propriétés de la poussière dans environ 600 galaxies.
- Mes études ont porté sur des données *Spitzer* et *Herschel* , qui sont une combinaison courante. Mais on peut se demander : quel est l'impact du nombre de bandes photométriques considérées pour l'ajustement ? Quelles sont celles nécessaires pour contraindre le pic IR ? Les longueurs d'onde dans le domaine sub-millimétrique, où la poussière froide émet son rayonnement, peuvent-elles vraiment mieux contraindre la masse totale de poussière ? Ou leur apport est-il davantage lié aux caractéristiques des gros grains (pente dans l'IR lointain) ?
- La prédiction de l'extinction par les propriétés obtenues de l'émission ne donne pas de résultats satisfaisants. L'ajustement combiné des deux observables permet-il une meilleure estimation des propriétés de poussière ?
- La pente entre 8 et 70 μm permet-elle de mieux ajuster la quantité de petits grains dans les bandes à courtes longueurs d'onde ? Le projet de télescope SPICA[2] est particulièrement intéressant pour cet intervalle de longueur d'onde. Par ailleurs, les futures observations par le télescope JWST[3] promettent d'apporter de nouvelles informations concernant les petits grains.
- Puisque le calcul par TR permet de connaitre la distribution du champ de rayonnement dans chaque cellule de la grille, peut-on vérifier la validité des lois empirique qui décrivent ce champ dans les modèles de poussière ? Y a-t-il une meilleure description pour ajuster les données ? Les effets de géométrie observés par TR peuvent-ils être pris en compte dans un modèle de poussière "simplifié" ?

Répondre à ces questions permettra d'améliorer encore davantage les modèles de poussière actuels, et peut-être de les rendre plus généraux. Néanmoins, il semble évident qu'à mesure que les réponses apparaitront, de nouvelles interrogations feront surface, et promettent une recherche intense et riche.

[2] *Space Infrared telescope for Cosmology and Astrophysics*
[3] *James Webb Space Telescope*

Jérémy CHASTENET

Analyse de l'émission des poussières dans les galaxies proches

Résumé

Ma thèse s'est concentrée sur les conséquences qu'ont les choix de modélisation de l'émission de la poussière sur ses propriétés déduites dans les galaxies proches.

Une première étude a montré que tous les modèles ne reproduisent pas des observations de deux galaxies proches de façon satisfaisante, bien que tous reproduisent l'émission IR de la Voie Lactée. Cela a aussi mis en évidence que la composition de la poussière est différente d'une galaxie à l'autre, et différente de celle de la Voie Lactée. Le choix de l'environnement des grains, à travers la description du champ de rayonnement qui chauffe ces grains, impacte significativement les résultats tels que la masse totale de poussières.

Une deuxième étude s'est concentrée sur les biais systématiques dus à l'emploi de lois empiriques de mélange pour décrire le chauffage de la poussière. J'ai montré que les masses déduites peuvent être sous- ou surestimées, bien que les ajustements aux données apparaissent raisonnables.

Les résultats de cette thèse montrent alors qu'il est nécessaire de prendre en compte les choix de modélisation pour déterminer au mieux les propriétés des poussières dans les galaxies proches.

Mots-clefs

Astrophysique – Milieu interstellaire – Poussière – Galaxies – Modélisation

Résumé en anglais

My thesis focused on the implications of dust emission modelisation choices on its derived properties in nearby galaxies.

A first approach showed that all models do not fit observations of two nearby galaxies adequately and similarly, although they all managed to fit the Milky Way infrared emission. It also highlighted that the dust composition is not the same between those two galaxies, and also with that of the Milky Way. The choice of the dust grains environment, through the incident radiation field, can significantly impact results like the total dust masses.

A second project investigated the systematics errors due to the empirical laws used to describe the radiation field that heats the dust grains. I showed that some parameters can be over- or underestimated, while showing good fits to the observations.

These results show that it is important to take into consideration the choices made for modelisation in order to accurately determine dust properties in nearby galaxies.

Key-words

Astrophysics – Interstellar medium – Dust – Galaxies – Modelisation